

LORENZO CAMPANA
TURBULENT DRAG REDUCTION BY
SUPERHYDROPHOBIC SURFACES

TURBULENT DRAG REDUCTION BY
SUPERHYDROPHOBIC SURFACES

LORENZO CAMPANA



Turbulent drag reduction by superhydrophobic surfaces

Meccanica Teorica ed Applicata
Ingegneria Civile ed Industriale
University of Rome "La Sapienza"

Master Thesis

Lorenzo Campana: *Turbulent drag reduction by superhydrophobic surfaces*,
© Master Thesis

ADVISOR:
Carlo Massimo Casciola

CO-ADVISOR:
Francesco Battista

PHD. STUDENT:
Roberta Costantini

LOCATION:
Roma

TIME FRAME:
March 2017

*What we observe is not nature itself,
but nature exposed to our method of questioning.*

— Werner Heisenberg

Dedicated to the loving memory of my Grandfather.

ABSTRACT

The use of the combination of surface roughness and chemical treatment to obtain superhydrophobic surfaces (SHSs) for engineering large slip at the fluid-solid interface is analysed. The superhydrophobic surfaces (SHSs) were initially inspired by the unique water-repellent properties of the lotus leaf and can be employed to produce drag reduction in turbulent flows. The effects of a SHS consist on micro-grooves which can entrap gas pockets when submerged in the water, i.e. at the groove is present an interface liquid-gas with a no zero velocity. Direct numerical simulations (DNS) are used to investigate the drag-reducing performance of SHSs in a turbulent pipe flow. The SHS was modelled through a shear-free boundary condition on the air-water interface. Seven different configurations are analyzed: they differ from the micro-aligned with the flow direction, i.e. the pipe axis. The configuration of SHS influences the drag reduction within the pipe. The drag appears reduced in the superhydrophobic cases with respect to the smooth classical case. This drag reduction strongly depends on the geometrical features the surfaces. The increment of drag reduction is remarkable in the cases with a large width of the grooves. To understand the phenomena linked to the drag reduction mechanism, the turbulent vortical structures are studied. These structures are significantly modified compared to the smooth case. The quantitative relation between the statistical information of the flow and the drag reduction is investigated through the balance of momentum equation. Fukagata *et al.* [12] derive an equation which allow to separate the different dynamical effects producing frictional drag in turbulent pipe flows. The result underlines that the contribution of the Reynolds stress within the pipe rises with the width of groove providing a negative contribution to the drag reduction. This effect is exceeded by the contribution of the slip velocity at the wall. Finally the pressure average and fluctuations, which provide an overall drag reduction, have been analysed in order to examine the stability of the interface liquid-vapour (Cassie state). The pressure fluctuations have been studied through the analysis of their probability density functions (PDF). Increasing the width of grooves, the range of pressure fluctuations rises up. It is important to investigate about what is the stable state of the system between Cassie and Wenzel. As it is known if the system is in the Wenzel state the superhydrophobic surface does not take any advantage in terms of drag reduction, but it produces a negative effect. In conclusion all observation appear to be very innovative because these kind of studies are not still present in literature, particularly for the application of turbulent pipe flow.

ACKNOWLEDGMENTS

First, I would like to thank my thesis advisor Prof. C. M. Casciola, that with his lectures aroused my enthusiasm for this subject. Another great thank goes to Prof. P. Gualtieri and Prof. F. Battista for the passion and the commitment shown during my last year.

In particular, the door of Prof. Battista's office was always open, and I could run into whenever I had a trouble or a question about my thesis. He continuously stressed that this was my own work, but he very kindly steered me in the right direction.

I also gratefully acknowledge dr. R. Costantini for her support, as the second reader of this thesis, and I am indebted for her availability.

Finally, I must express my very profound gratitude to my parents, for providing an unfailing support and a continuous encouragement throughout my years of study and while writing the thesis. This accomplishment would not have been possible without them. *Thank you.*

CONTENTS

I SUPERHYDROPHOBIC SURFACE	1
1 INTRODUCTION	2
2 STATE OF ART	5
2.1 Wetting model	5
2.1.1 Superhydrophobicity	7
2.1.2 Cassie and Wenzel models	8
2.1.3 Metastability of superhydrophobic state	10
2.2 Properties of superhydrophobic surfaces	11
2.2.1 Catalysis of cavitation	11
2.2.2 Wall slip	11
2.3 Drag reduction	12
2.3.1 DNS Data	13
2.3.2 Experimental Data	18
2.4 Interface Liquid-gas	22
II TURBULENCE	25
3 TURBULENCE	26
3.1 Some characteristics	26
3.2 Averages	27
3.3 Mean-flow equations	28
3.4 The energy cascade	29
3.5 The Kolmogorov hypotheses	30
3.5.1 The Energy spectrum	31
4 WALL FLOWS	34
4.1 Channel flow	34
4.1.1 The mean equations	35
4.1.2 Characteristic quantities	36
4.1.3 Mean velocity profile	37
4.2 Pipe flow	39
III DIRECT NUMERICAL SIMULATION	43
5 NUMERICAL SIMULATIONS	44
5.1 Equations of Pipe	44
5.2 Chorin's projection method	45
5.2.1 Solution of Poisson Equation	47
5.2.2 Staggered mesh	47
5.3 Time interpolation	47
5.4 Boundaries conditions	48
5.5 Characteristic parameters	51
5.5.1 Calculus domain	51
5.6 Simulations	51
6 RESULTS	53
6.1 Mean velocities	53
6.1.1 Longitudinal velocity	54

6.1.2	Radial velocity	58
6.1.3	Phase velocity	62
6.2	Reynolds stress	63
6.3	Fukagata's balance	66
6.4	Pressure field	68
6.4.1	Probability density function	68
7	CONCLUSIONS	73
IV	APPENDIX	75
A	FUKAGATA'S BALANCE	76
B	DISCRETISATION OF POISSON'S EQUATION	78
	BIBLIOGRAPHY	80

LIST OF FIGURES

Figure 1.1	Lotus leaf and water strider	2
Figure 1.2	SEM	3
Figure 2.1	Section of the half drop.	6
Figure 2.2	Three phase contact at a solid surface.	6
Figure 2.3	Water drops on a superhydrophobic surface.	8
Figure 2.4	Wenzel and Cassie states.	9
Figure 2.5	Equilibrium contact angle θ^* on a rough surface.	10
Figure 2.6	Intrinsic slip at a smooth wall.	12
Figure 2.7	Drag reduction rate, R_D .	14
Figure 2.8	Drag and mean slip velocity variation with slip length.	15
Figure 2.9	Mean velocity profiles, u^+ .	16
Figure 2.10	Mean velocity profiles, $u^+ - u_s^+$.	17
Figure 2.11	Velocity fluctuations.	17
Figure 2.12	Schematic representation of drag decrease and increase mechanism.	18
Figure 2.13	Schematic representations of the SHSs.	18
Figure 2.14	Turbulent drag reduction performance of the SHS for both ridges and posts.	19
Figure 2.15	Schematic secondary flow mechanism over SHS.	19
Figure 2.16	Velocity profiles over a microridge surface.	20
Figure 2.17	Drag reduction as a function of Reynolds number for a channel.	20
Figure 2.18	The microridge spacing in wall units.	22
Figure 2.19	Macroscopic corner angle and microscopic contact angle.	23
Figure 2.20	Interface model.	23
Figure 3.1	<i>Reynolds' experiment:</i> in the first sequence the fluid is laminar, in the second one there is transition and in the last two the fluid is fully turbulent.	27
Figure 3.2	Stationary and non-stationary time series.	28
Figure 3.3	Scales of turbulence.	31
Figure 3.4	Homogeneous turbulence at very high Reynolds number, sketches of (a) the energy and dissipation spectra, (b) the contributions to the balance of equation (3.12), and (c) the spectral energy transfer rate.	32
Figure 3.5	Energy cascade.	33
Figure 4.1	Sketch of channel flow.	34
Figure 4.2	Profiles of the Viscous shear stress, and the Reynolds shear stress in turbulent channel flow: DNS data of Kim <i>et al.</i> [21]: dashed line, $Re = 5600$; solid line, $Re = 13750$.	36
Figure 4.3	A sketch of different wall regions in terms of $y^+ = y/\delta_v$.	37

Figure 4.4	Near-wall profiles of mean velocity from the DNS data of Kim <i>et al.</i> [21]: dashed line, $Re = 5600$; solid line, $Re = 13750$; dot-dashed line, $u^+ = y^+$. 38
Figure 4.5	Near-wall profiles of mean velocity: solid line, DNS data of Kim <i>et al.</i> [21]: $Re = 13750$; dot-dashed line, $u^+ = y^+$; dashed line, the log law. 39
Figure 4.6	Trend of the velocity profile in the different regions of the channel 40
Figure 4.7	Scheme of a cylindrical pipe. 40
Figure 4.8	Velocity profile along z direction in terms of wall units y^+ performed by a DNS of pipe flow with $u_\tau = 6.82 \cdot 10^{-2}$, $Re_\tau = 180.72$ and $Re = 2650$. 41
Figure 4.9	(a) Stresses and (b) Fluctuations velocity performed by a DNS of pipe flow with $u_\tau = 6.82 \cdot 10^{-2}$, $Re_\tau = 180.72$ and $Re = 2650$. 42
Figure 5.1	The staggered mesh in two dimensions. 48
Figure 5.2	Scheme of superhydrophobic surface with two different interfaces. 49
Figure 6.1	Scheme of SHS surface. 54
Figure 6.2	Means velocity profiles of $\langle u_z \rangle^+$. 55
Figure 6.3	Means velocity profiles $(\langle u_z \rangle - U_s)^+$. 56
Figure 6.4	The distance from the wall y^+ in semi-logarithmic scale as a function of means velocity profiles $(\langle u_z \rangle - U_s)^+$. 58
Figure 6.5	Two dimensional mean radial velocity $\langle u_r \rangle _\vartheta$. 59
Figure 6.6	Two dimensional mean vorticity along z direction $\langle \omega_z \rangle _\vartheta$ in correspondence of grooves and peaks. 60
Figure 6.7	Two dimensional mean vorticity along z direction in correspondence of grooves and peaks. 61
Figure 6.8	Schematic representation of vortical structures: principal (<i>big one</i>) and secondary (<i>small one</i>). 62
Figure 6.9	Trend of y^+ as a function of velocity $\langle u_z \rangle^+ _\vartheta$. 63
Figure 6.10	Mean fluctuations velocities for the seven cases. 64
Figure 6.11	Representation of stresses. 65
Figure 6.12	Fukagata's balance. 67
Figure 6.13	Two dimensional plot of mean pressure. 69
Figure 6.14	Probability density functions (PDF). 70
Figure 6.15	Probability density functions (PDF) normalized with the standard deviation σ . 71
Figure B.1	One dimensional mesh, where the scalar quantities ϕ is located in the middle of two consecutive nodes. 78

LIST OF TABLES

Table 1	Values of Low storage Runge-Kutta coefficients. 48
Table 2	Description of boundaries conditions for different cases. 50

Table 3	All simulations performed with <i>superhydrophobic surface</i> SHS with flat interface. The N° of cells indicate the presence of x cells slip and y no slip. This pattern are replaced along the entire circumference. The solid fraction ϕ_s is evaluated as $y/(x+y)$ and expresses the percentage of the slip zone along θ . The dimensions of pattern are expressed also in terms of wall unit and physic unit [μm], the latter evaluated supposing a radius pipe of $R = 1\text{mm}$. 52
Table 4	Values of Re_τ and the deviation from the mean value. 54
Table 5	Values of U_b , U_s and their difference also in terms of wall units +, having adimensionalized with u_τ where the characteristics parameters are $\text{Re}_N = 5000$ and $\text{Re}_\tau = 311.35$. 54
Table 6	Different values of the parameters k and B of the equation (6.4) for all simulations performed. 57
Table 7	Here are reported the values of standard deviation σ , skewness s , flatness f and the values of the pressure fluctuations p'_{\max} and p'_{\min} . 72
Table 8	Drag reduction increment $((U_b - U_{\text{ref}})/U_{\text{ref}})$ compared to the reference (Ref.) smooth case for different configurations (ϕ_s being the solid fraction). 74

Part I
SUPERHYDROPHOBIC SURFACE

INTRODUCTION

Several design ideas have been inspired by nature. Biological mechanisms can be studied to engineer systems for modern industrial applications [3]. When a water droplet rolls easily, retaining a nearly perfect spherical shape on a surface that remains essentially dry, such a surface is super-repellent or superhydrophobic [4]. Superhydrophobic surfaces were originally inspired by the unique water repellent properties of the lotus leaf [35] (see figure 1.1). Common superhydrophobic materials include many plant leaves, duck feathers, and glass surfaces coated by black soot dispersed from a lighted candle. More than 80 years ago Wenzel, Cassie and Baxter, pointed out the two physical ingredients necessary for a surface to be superhydrophobic: a bare hydrophobic coating, such as wax crystalloids on plant leaves, and roughness at the micro-scale. Strong water repellency occurs because the roughness effectively increases the liquid-solid free energy. This is the consequence of either a larger real contact area between the two components, the case of the liquid impregnating the surface (the so-called Wenzel state), or a replacement of the true liquid-solid contact by a highly energetic liquid-vapour interface, the case of the liquid interface suspended on an air cushion on top of the roughness peaks (the so-called Cassie state).



(a) *Lotus leaf*



(b) *Water strider*

Figure 1.1: (a) Water droplet beading on lotus leaf with static contact angle higher than 150 degrees. (b) Water strider possess a very rare trait that allows them to walk on water. This ability to the hydrophobic waxy microhairs covering their legs, microsetae, which are superimposed with nanogrooves.

Notwithstanding significant theoretical and experimental progress, challenges remain in the material design of superhydrophobic surfaces for wetting purposes. First and foremost, there are the issues of robustness and surface fragility, both thermodynamic and mechanical. In fact, the fragility of the Cassie state is the main technological challenge for the use of superhydrophobic materials (see figure 1.2) in underwater applications: at a depth of a few metres, the hydrostatic pressure is sufficient to balance the capillary pressure and to destabilize the more desirable Cassie state in favour of a Wenzel state. This Cassie-to-Wenzel transition involves the impregnation of the roughness fea-

tures of the surface with liquid, and it can occur for a number of reasons in addition to an increase in pressure, such as the presence of surface defects, evaporation, or the action of external forces. To avoid this problem, superhydrophobic materials can be designed with two length scales: a large scale governing the effective wetting properties of the surface, and a much smaller one that prevents the final stage of impregnation by increasing the critical transition pressure. Another method would involve a back-pressurization of the underlying gas layer, notwithstanding subtle geometric properties of the pressurized Cassie state with pressure-induced menisci curvature impacting both static and dynamic responses of the interface. More work in this area will be needed, perhaps by taking clues from biology. The robustness of the superhydrophobic state in plant leaves or animal feathers originates from the self-healing of the surface, and similar biomimetic processes remain to be achieved in the lab.

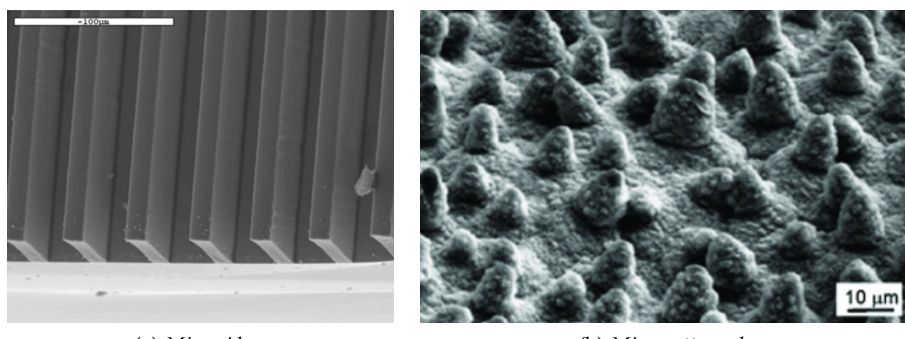


Figure 1.2: Scanning electron microscopy (SEM) image of superydrophobic surface. (a) microridges with the width of the cavities and ridges are 30 and 10 μm , respectively. The depth of the rib is 10 μm . (b) Image showing morphological micro-structures micropatterned (10 μm).

Another topic of interest is the drag-reducing ability of superhydrophobic surfaces. Indeed, the bubble cushion at the interface between the liquid and the solid in the Cassie state suggests a low viscous friction, as confirmed by a number of experiments.

Friction in fluids is manifest by the phenomenon of drag -the force required to move an object through a fluid or move a fluid through a device.

The potential reduction of skin friction drag in turbulent flows is of large economical and ecological interest and has continuously been investigated over the past few decades. The development of techniques which produce significant drag reduction in turbulent flows can have a profound effect on a variety of existing technologies. The benefits of drag reduction range from a reduction in the pressure drop in pipe flows to an increase in fuel efficiency and speed of marine vessels. A variety of different drag-reducing techniques are known today which are commonly classified in passive, active and reactive flow control mechanisms. Drag reduction in turbulent flows can be achieved through a number of different mechanisms including the addition of polymers to the fluid, the addition of bubbles or air layers, compliant walls, and

riblets. From an application point of view, passive flow control techniques are most appealing since they do neither require the installation of additional actuators and sensors nor the continuous energy input to run the control. *Superhydrophobic surfaces* can be used as a new passive technique for reducing drag over a wide range of Reynolds numbers from laminar to turbulent flows. New investigations will require new methods to quantify the effective properties of superhydrophobic surfaces. The traditional approach, which consists of characterizing superhydrophobic materials using solely their effective contact angles, will not necessarily lead to physical insight into transport phenomena. Instead, a physical parameter that follows the scaling and quantifies drag reduction is an effective slip length, which is the ratio of the effective surface velocity to the surface shear rate. Slip lengths up to 400 μm have been attained, suggesting their potential applicability in ducts with diameters up to 1 mm. Indeed, a pipe 1 mm in diameter coated with a material with the aforementioned slip length would experience more than a 75% reduction in friction. Such a large reduction is of potential importance for laminar-flow fuel cells and the dispersion of solutes in microfluidics, for example. Low friction requires a surface with a large no-shear (gaseous) region which, by definition, fractal surfaces do not possess.

2

STATE OF ART

In this chapter the current studies of superhydrophobic surfaces will be discussed, with particular emphasis on the model that characterises the two conditions of wettability said *Wenzel* and *Cassie-Baxter*; moreover the presence of metastability of the models will be discussed, as well as an analysis of theoretical, numerical and experimental works in literature concerning the studies of the drag reduction on superhydrophobic surfaces for a turbulent flow.

2.1 WETTING MODEL

The most important quantity in wetting and surface science is the *surface energy* γ . In a thermodynamic approach, surface energy is an excess quantity related to the energy cost of forming of a new interface in a two-phase system; by definition, therefore, is positive and intensive. An excess quantity is given by the difference between the actual quantity and that the system would have if the bulk properties were maintained up to a mathematical dividing surface. For instance, the grand potential of a liquid in equilibrium with its vapour reads

$$\Omega(\mu, V, T) = \Omega_l + \Omega_v + \Omega^{(s)} = -P_l V_l - P_v V_v + \gamma A \quad (2.1)$$

where the subscripts l and v denote the bulk quantities in the liquid and vapour phases, respectively, (s) is the excess part, μ the chemical potential of the system, V the total volume given by the sum of the volumes of the liquid and vapour domains $V \equiv V_l + V_v$, where $V_l = \text{vol}(D_l)$ and $V_v = \text{vol}(D_v)$, T the temperature, A the surface area of the liquid-vapour interface $A = \text{area}(\Sigma)$, P the pressure of each phase, and the surface energy. The open system described by the grand potential is in thermal and chemical equilibrium, as T and μ are constant everywhere in the system volume V .

In the case of a flat liquid-vapour interface, the condition for mechanical equilibrium is simply $P_l = P_v = P$. From a mechanical point of view, γ may be interpreted as the force per unit length that allows interfaces to withstand pressure differences across them; it is consequently often referred as *surface tension*. Imagine to cut ideally the sphere in a half, see figure 2.1; the pressure force acting on the hemisphere in the direction perpendicular to the cut is $\pi R^2 (P_l - P_v)$. This force is balanced by the surface tension acting on the circumference created by the cut, $2\pi R$; the surface tension is the force that keeps the two hemispheres together. The forces in the direction of the cut, instead, are already balanced because of the symmetry of the hemisphere. This simple force balance yields to the so-called *Laplace's equation*

$$P_l - P_v = 2\pi \frac{\gamma}{R} \quad (2.2)$$

that relates the pressure jump across an interface to the surface tension and the interface curvature. It is seen that the pressure is always higher inside the

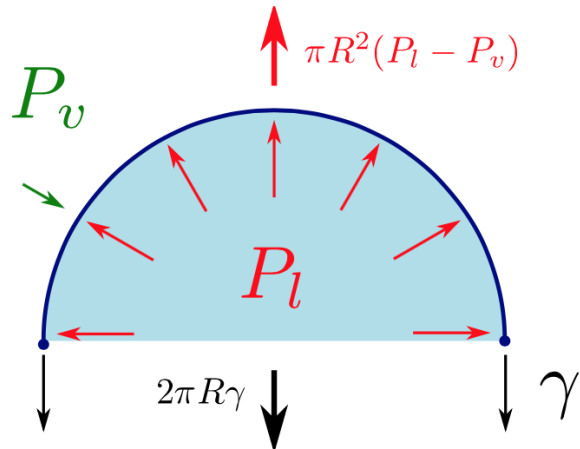


Figure 2.1: Section of the half drop discussed in the text, showing the pressures P_l (in red) and P_v (in green, only one arrow shown) acting in the opposite directions on the drop's surface. The surface tension (in black) acts on the bottom line in the direction perpendicular to the cut. The total forces in the direction of the cut are obtained by integrating the pressure on the surface and the surface tension on the line (thick arrows).

sphere, that is, $P_l > P_v$ for drops and the opposite for bubbles. This equation, together with the Young equation (2.3) explained below, is at the origin of most capillary phenomena and expresses the mechanical equilibrium condition for non-flat liquid-vapour interfaces.

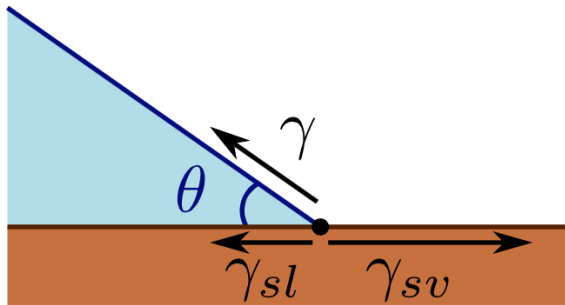


Figure 2.2: Three phase contact at a solid surface: the liquid-vapour interface intersects the solid surface with a tangent angle θ . The balance of the surface tensions γ , γ_{sl} , and γ_{sv} at the triple line (black point) yields Young equation 2.3.

In the typical case of wetting, where a liquid, a gaseous phase (that can be the vapour phase of the wetting liquid or air), and a solid are present, three surface energies need to be specified, γ_{sl} , γ_{sv} and γ_{lv} , related to the solid-liquid, solid-vapour, and liquid-vapour surfaces interfaces, respectively. Hereafter, the liquid-vapour surface energy will be referred to as γ for simplicity. The line where the three interfaces meet is called *triple line* (or contact line). A force balance at this line yields the second fundamental equation of capillarity, the so-called *Young's equation*. Imagine that the liquid-vapour interface

intersects a perfectly smooth solid surface with a tangent angle θ , as illustrated in figure 2.2. Mechanical equilibrium of the contact line requires that the sum of the surface tensions projected on the horizontal direction equals zero, $\gamma \cos \theta + \gamma_{sl} - \gamma_{sv} = 0$. This condition yields the equilibrium contact angle on a ideally smooth surface

$$\cos \theta = \frac{\gamma_{sl} - \gamma_{sv}}{\gamma} \quad (2.3)$$

The surface tension component in the vertical direction, $\sin \theta$, are equilibrated by the wall reaction. The angle in equation (2.3) is related only to surface energies that are chemical properties of the surface and of the wetting liquid and is the basic quantity used to characterise the wetting behaviour of a surface with a given liquid. Accordingly, this angle is usually referred to as chemical angle or Young contact angle, θ_Y . For ideally smooth substrates equations (2.2) and (2.3) completely describe the possible wetting scenarios. Focusing on the case of partial wetting where $0 < \theta_Y < \pi$; when the Young contact angle falls in this interval a lens of liquid is formed on the smooth substrate. An useful reference for capillary phenomena in a gravitational field is the capillary length $l_c = \sqrt{\gamma/m_l g}$ that compares gravitational and capillary forces; here m_l is the liquid mass density and g the gravitational acceleration. The capillary length gives an order of magnitude of when gravity start to deform liquid bodies: if the lens is smaller than l_c then the drop will be a spherical cap sitting on the smooth solid substrate, as dictated by Laplace and Young equations (2.2)-(2.3). For lenses larger than the capillary length, for instance any pool of water of sufficient extension, gravity deforms the interface giving rise to *puddles*, where the curvature of the interface is not constant; capillary effects are seen only at distances comparable to l_c from the edges of puddles. For clean water at ambient conditions l_c is around 2mm; it is interesting to note that below this threshold there is no intrinsic length scale for wetting phenomena, and all drops from few nanometers to millimeters look alike. Surfaces exhibiting Young contact angles $0 < \theta_Y < \pi/2$ are defined as *hydrophilic* since they tend to be wet by the given liquid; for instance, in trees the capillary action of hydrophilic lems can pump the sap for tens of meters. Instead when $\pi/2 < \theta_Y < \pi$, the surface is said *hydrophobic*, since liquid tend to retract from it; for instance, the capillary action of mercury on glass capillaries forces the meniscus to dry the surface. The perfectly drying regime occurs for $\theta_Y = \pi$, when the liquid tends to suppress any contact with the surface. This latter case has less practical importance as compared to complete wetting, since examples of perfectly drying surfaces are extremely rare.

2.1.1 Superhydrophobicity

As said above, for surfaces with contact angles less than $\theta < \pi/2$, the surface is considered hydrophilic, whereas for those with $\theta > \pi/2$, the surface is hydrophobic. However, reporting only the equilibrium contact angle for a surface is insufficient. Owing to the presence of surface roughness or chemical heterogeneity, a liquid droplet can actually exist over a range of contact angles between the receding contact angle, θ_r , and the advancing contact angle, θ_a . This nonuniqueness of the equilibrium contact angle is known as the contact angle hysteresis, $(\theta_r - \theta_a)$. Superhydrophobic surface is the combination

of a very large contact angle and a low contact angle hysteresis that defines a surface as superhydrophobic. The lack of significant contact angle hysteresis makes a water drop on a superhydrophobic surface unstable to even the smallest perturbation and allows it to move easily across these surfaces. There is some force that resists the action of gravity that would be impossible if the contact angles were the same for the advancing and receding sides of the drop. This hysteresis force (per unit length) is defined as

$$H = \gamma_{lv}(\cos \theta_r - \cos \theta_a) \quad (2.4)$$

For superhydrophobic surfaces, drops tend to roll rather than slide because the large contact angle moves the center of mass well above the surface. Rolling water drops tend to collect and remove dirt as they go, resulting in the remarkable self-cleaning ability of the lotus leaf and other superhydrophobic surfaces. In addition to plants, there are a large number of animals and insects that have evolved unique ways to utilize superhydrophobicity. Water striders, for example, have legs with thousands of tiny hydrophobic hairs or microsetae that allow them to stand and move quickly on water. Synthetic superhydrophobic surfaces have recently been developed that are capable of obtaining contact angles that approach $\theta \sim \pi$ with little to no measurable hysteresis [34]. Importantly, the difference between a hydrophobic surface and a superhydrophobic surface lies not in the surface chemistry, but in the micro or nanoscale surface roughness (see figure 2.3). Lotus leaves, for example, have micrometer-sized protrusions covered in hydrophobic wax crystalloids. For a rough surfaces like that of a lotus leaf, water will either fully or partially wet the surface depending on the hydrophobicity of the surface, the static pressure in the water, and the precise geometry of the surface features.

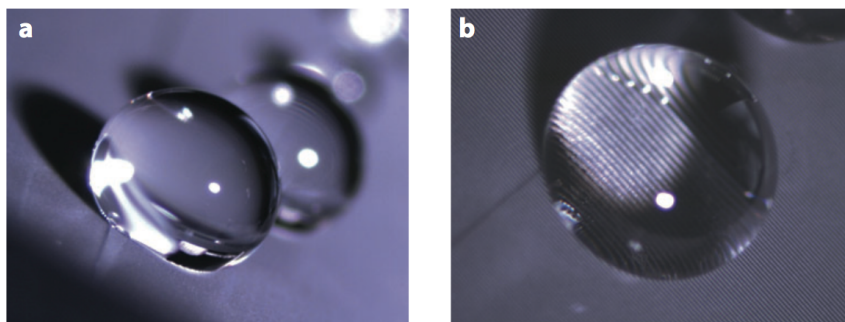


Figure 2.3: Water drops on a superhydrophobic surface consisting of $15\mu\text{m}$ wide ridges spaced $45\mu\text{m}$ apart seen from (a) the side and (b) the top. Note that the ridges and the air-water interface supported between them are visible through the drop in the top view (b).

2.1.2 Cassie and Wenzel models

There are two ideal models that are useful in understanding how *superhydrophobicity* stems from hydrophobicity and roughness and how it breaks down. The superhydrophobic properties of surfaces are connected with air trapped within surface roughness, for which the relevant model is the *Cassie*

[6] one. In studying how ducks feathers could resist wetting, Cassie and Baxter imagined that the feathers structure was not completely wet by water, but a flat liquid-air interface formed at roughness elements, thus entraining air. This situation is schematically shown in figure 2.4 (right); and using the usual notation for the solid fraction, ϕ_s , the well-known Cassie formula is recovered

$$\cos \theta^* = \phi_s \cos \theta_Y - (1 - \phi_s) \quad (2.5)$$

This simple model allows to predict the equilibrium contact angle θ^* for surfaces with a given geometry (encompassed in ϕ_s) and surface chemistry (θ_Y). For hydrophobic surfaces, $\theta_Y > \pi/2$, the effect of a Cassie state is to increase the equilibrium contact angle as compared with an equivalent smooth surface thus giving rise to superhydrophobicity. It is seen that for vanishing solid fractions the equilibrium contact angle tends to the perfect drying condition, $\theta^* \rightarrow \pi$. The equation (2.5) is valid for flat liquid-vapour interfaces and describes the contact angle as seen by an observer that considers as the reference plane a flat (virtual) surface, ignoring the fine scale details of the real surface.

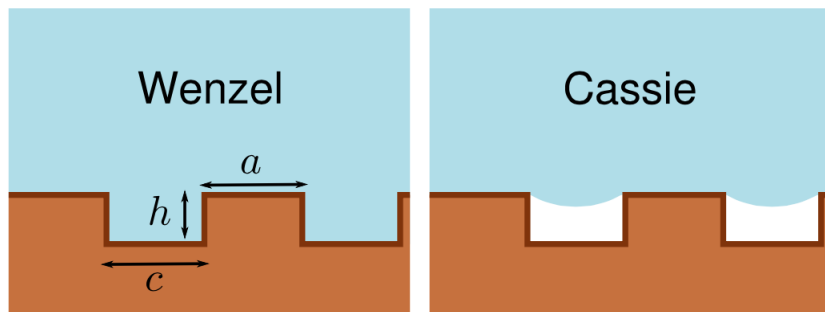


Figure 2.4: Wenzel (left) and Cassie (right) states on a submersed superhydrophobic surface with a pattern of rectangular grooves having height (h), hole width (c), and crest width (a).

If the same roughness profile considered for the Cassie state is completely wet, as in figure 2.4 (left), it is possible to define the equilibrium contact angle as

$$\cos \theta^* = r \cos \theta_Y \quad (2.6)$$

which is named after Wenzel [38], the first to derive equation (2.6). Since the roughness factor is given by the ratio between the actual surface area and the projected area, with $r > 1$, on hydrophobic surfaces, where $\cos \theta_Y < 0$, the Wenzel formula predicts that the equilibrium contact angle is larger than that on a flat surface. The two states are summarised in figure 2.5, showing in solid lines the configuration having minimal energy between the Cassie and Wenzel ones. For $\theta_Y \sim \pi/2$, the Wenzel state is always more stable, while for larger θ_Y (in the case of hydrophobic surfaces) the Cassie state is favoured. For very hydrophilic surfaces, $\cos \theta_Y > 0$, surface asperities are filled with liquid. For a droplet in the Cassie state, there is a maximum static pressure that can be supported before the air-water interface deflects enough to reach

the advancing contact angle and is driven into the space between the surface roughness. At this point the system reverts to the Wenzel state. Using Young's law and assuming an interface with a single radius of curvature such as that which exists between two parallel ridges as seen in figure 2.4 (right), one finds that

$$\Delta p_{\max} = p_{\text{liquid}} - p_{\text{gas}} = -\frac{2\gamma \cos \theta_a}{c} \quad (2.7)$$

Thus, the maximum static pressure that can be supported in the Cassie state decreases with increasing feature spacing.

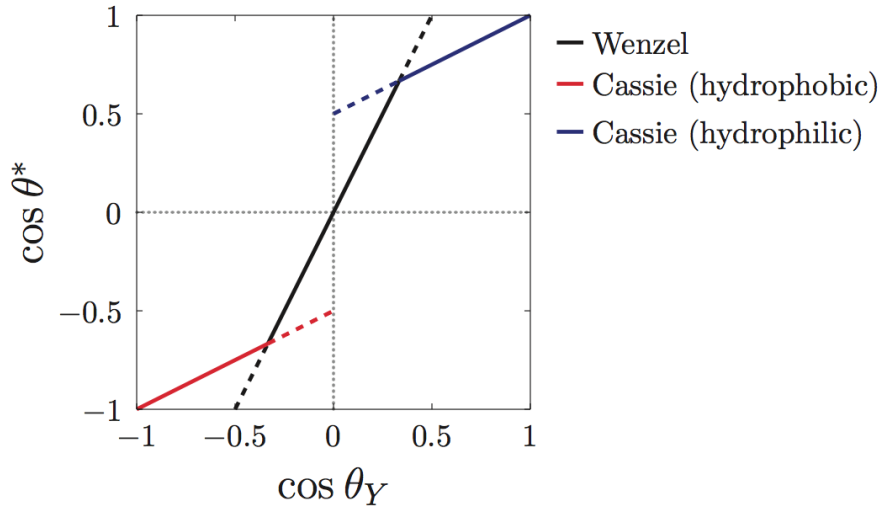


Figure 2.5: Equilibrium contact angle θ^* on a rough surface as predicted by Wenzel equation (2.6), in *black*, Cassie equation for a hydrophobic surface (2.5), in *red*, and Cassie equation for a hydrophilic surface (equation (2.5)) with the opposite sign in last term, in *blue*. The roughness has $\phi_s = 0.5$ and $r = 2$, corresponding, on the regular pattern with $a = c = h$.

2.1.3 Metastability of superhydrophobic state

Considering the system of the two equation models (2.5) and (2.6), one can obtain the critic value θ_c between the two states

$$\cos \theta_c = (\phi_s - 1)(r - \phi_s) \quad (2.8)$$

By the comparison between surface energy linked to Wenzel state and Cassie too, the development of air pocket is occurred only if $\theta_Y > \theta_c$. In figure 2.5 the dotted line represents the *metastability* of Cassie state, for contacts angles included $\pi/2 < \theta_Y < \theta_c$. Giacomello [15] investigates if the metastability Cassie-Baxter/Wenzel can exist, i.e. if it is possible to force a liquid to remain in the Cassie state when the stability thermodynamics conditions facilitate the Wenzel state (and vice versa). The free energy barrier separating these two states is found to largely exceed the thermal energy, confirming that liquids can be trapped in these metastable states. The Cassie-Baxter state and CB/W

metastabilities are supported even by the slightly hydrophilic surface considered ($\theta_Y < \pi/2$). This evidence suggests that surfaces may be realized to support the superhydrophobic CB state over a wide range of temperatures and densities (or, equivalently, pressures) and for a variety of liquids, provided that the Young contact angle is approximately equal to or larger than $\pi/2$. This study on the metastability is important also for technological practice, because it represents the way to extend the stability range of Cassie state.

2.2 PROPERTIES OF SUPERHYDROPHOBIC SURFACES

2.2.1 *Catalysis of cavitation*

At negative pressures, the gas nuclei stabilised by roughness and hydrophobicity on superhydrophobic surfaces may expedite the onset of cavitation. Cavitation is the abrupt nucleation of vapour bubbles inside a liquid in a (metastable) tensile state, corresponding to a negative ΔP . The formation of vapour bubbles is an activated event with large free energy barriers, related to the formation of a liquid-vapour interface. The presence of surfaces, contaminant particles, and hydrophobic patches may significantly speed up nucleation as compared to the bulk of a pure liquid. It can be demonstrated, in effect, that the rate of heterogeneous nucleation on superhydrophobic surfaces is increased by thousands orders of magnitude as compared to a flat surface [1]. Similarly to a catalyst, hydrophobic cavities act in lowering the free energy barriers and in breaking the nucleation process into multiple steps. In hydraulic and marine engineering, cavitation is known to rapidly deteriorate propeller blades and hydraulic structures. Cavitation damage is due to the collapse of the bubbles nucleated in the low pressure regions. The collapse produces extreme pressure and temperature conditions in addition to water jets in correspondence of solid walls. In other applications, the high energy concentration reached during bubble collapse may be favourably exploited in order to produce chemical synthesis of nanostructured materials, biomaterials, or in medicine to ablate selectively tissues.

2.2.2 *Wall slip*

An interesting question arising from the rapid development of superhydrophobic surface is which boundary condition must be expected for a liquid flowing on it. It has been observed that a finite velocity, the *slip velocity*, can be observed in the Cassie state arising from the composite gas-liquid and solid-liquid interface. This fact has remarkable consequences on both microscale and macroscale flows: for instance, wall drag can be reduced both in microfluidic devices and in turbulent flows [34]. In continuum fluid mechanics, the liquid slip is usually modelled with the Navier boundary condition, that replaces the usual no slip condition,

$$V_s = L_s \frac{\partial u}{\partial n} \Big|_w \quad (2.9)$$

Here U_s is the slip velocity, expressed in terms of the slip length, L_s , and the gradient of the liquid velocity parallel to the wall, u , in the direction normal

to the wall, n , computed at the wall. The slip length may be viewed as the distance from the wall where the extrapolated velocity vanishes, see figure 2.6; in this case, the nominal wall position must be considered (see e.g. the dotted line in 2.6). As already mentioned, L_s may be an intrinsic property of the wall, due to low affinity between the liquid and the solid, or an effective property arising from averaging over the roughness details, the *apparent slip*. Cassie states give rise to a composite boundary for the flow featuring liquid-solid interfaces, where the usual no slip (or intrinsic slip) condition holds, and liquid-vapour interfaces with a free-slip condition. By averaging out these microscopic details, the net effect on the flow is a large apparent slip length that can reach tens of microns. For this reason, superhydrophobic surfaces are very promising for applications of drag reduction.

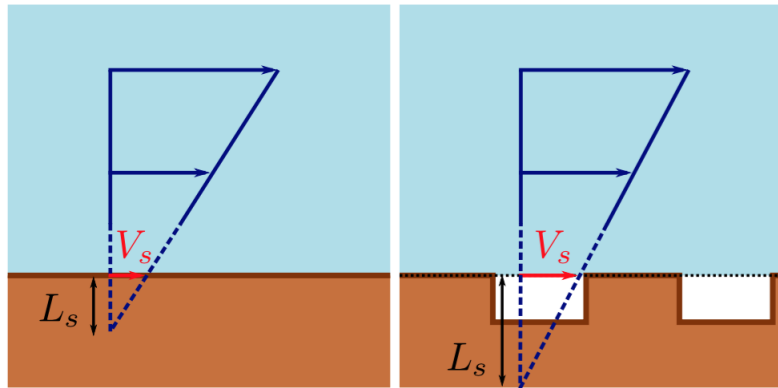


Figure 2.6: *Left*) Intrinsic slip at a smooth wall. The slip length L_s may be identified as the point where the extrapolated velocity profile vanishes. The slip velocity U_s is the velocity of the liquid at the wall in the direction parallel to it (in red). *Right*) Apparent slip at a structured wall (in this case the rectangular grooves). Cassie state with flat meniscus is represented.

For the case of grooves parallel and perpendicular to the flow with a flat meniscus, Lauga *et al.* [23] obtained an analytical expression for the apparent slip length L_s by solving the Stokes equation with mixed no-slip and no-shear boundary conditions

$$L_{s,\text{par}} = 2L_{s,\text{per}} = \frac{L}{\pi} \ln \left[\sec \left(\frac{\pi(1 - \phi_s)}{2} \right) \right] \quad (2.10)$$

where the subscript *par* and *per* denotes the parallel and perpendicular grooves, respectively, L the period of the groove pattern, and ϕ_s the solid fraction. It is worth noting that slip grows proportionally to L , and diverges logarithmically with vanishing solid fractions. The upper limit for realising large groove spacing L is the stability of the Cassie state, as previously mentioned. Low solid fractions, instead, pose a problem of mechanical resistance of the surface roughness.

2.3 DRAG REDUCTION

Drag reduction in turbulent flows can be achieved through a number of different mechanisms, including the addition of polymers to the fluid, of bubbles

or air layers, compliant walls, riblets and active turbulence control. A number of recent studies have investigated the use of superhydrophobic surfaces as a new passive technique for reducing drag in turbulent flows. Geometrically, riblets appear similar to the superhydrophobic surfaces; however, their scale and function are completely different. Riblets are ridges in the Wenzel state that are aligned in the flow direction. They reduce drag by disrupting the transverse motion of the fluid at the surface, thereby moving near-wall turbulent structures further from the wall. Riblets only perform well within a limited range of Reynolds numbers, and can have derogatory effects outside of their designed range. To be effective, a spacing between riblets, $w^+ = w/v(\tau_w/\rho)^{1/2}$, between $10 < w^+ < 30$ wall units must be maintained, where v is the viscosity, τ_w is the wall shear stress, and ρ is the density of the liquid. The superhydrophobic microfeatures used to produce turbulent drag reduction are typically too small to simultaneously produce a riblet effect.

Air-layer drag reduction is another technique similar to superhydrophobic surfaces. Here air is continuously injected into the boundary layer to produce an uninterrupted vapour zone between the solid surface and the water. Thus the air layers can produce nearly complete elimination of skin-friction drag. This mechanism creates three distinct regions: up to 20% bubble drag reduction at low air-injection rates, a transitional region at moderate injection rates, and a continuous air layer at large air-injection rates.

In active turbulence control technique, as studied by Choi *et al.* [7], the drag reduction is accompanied by significant lowering of the intensity of the wall-layer structures and in the magnitude of Reynolds shear stress throughout the flow. In this case there are essentially two mechanisms. Firstly, within a short time after the control is applied, drag is reduced mainly by deterring the sweep motion without modifying the primary streamwise vortices above the wall. Therefore the high-shear-rate regions on the wall are moved to the interior of the channel by the control schemes. Secondly, the active control changes the evolution of the wall vorticity layer by stabilizing and preventing lifting of the spanwise vorticity near the wall, which may suppress a source of new streamwise vortices above the wall.

2.3.1 DNS Data

The more relevant present in literature will be discussed, obtained through direct numerical simulation (DNS), on the study of drag reduction on superhydrophobic surfaces.

Fukagata *et al.* [14] present a theoretical prediction for the drag reduction rate achieved by superhydrophobic surfaces in a turbulent channel flow. The predicted amount is in good agreement with results obtained from direct numerical simulations for the streamwise, spanwise and combined case at $Re_\tau \approx 180$ and 400. The drag reduction rate, R_D , is defined as

$$R_D = \frac{C_{f0} - C_f}{C_{f0}} = 1 - \left(\frac{u_\tau}{u_{\tau0}} \right)^2 = 1 - \left(\frac{Re_\tau}{Re_{\tau0}} \right)^2 \quad (2.11)$$

where C_{f0} and C_f are the skin friction coefficients in no-slip and slip flows, respectively; Re_τ is the friction Reynolds number of the slip flow. They determined the analytical expressions to quantify the drag reduction rate to a

function of the slip length l^+ , $Re_{\tau 0}$ and $u_{\tau}^{+0} = \sqrt{1 - R_d}$ for the three cases accounted. Figure 2.7 shows the drag reduction rate predicted by using the theoretical formula. In all cases, the theoretical predictions are in good agreement with the results of DNS for the whole range of slip length. There is an excellent agreement at $Re_{\tau 0} = 400$, for which the low-Reynolds number effect should be much weaker than $Re_{\tau 0} = 180$. Moreover, the agreement in the combined slip case confirms the assumption additionally made for that case: the drag decrease and increase mechanisms by the streamwise and spanwise slips are independent of each other. As the Reynolds number increases, the effect of drag decrease due to the streamwise slip is gradually weakened, while the drag increase due to the spanwise slip deteriorates faster.

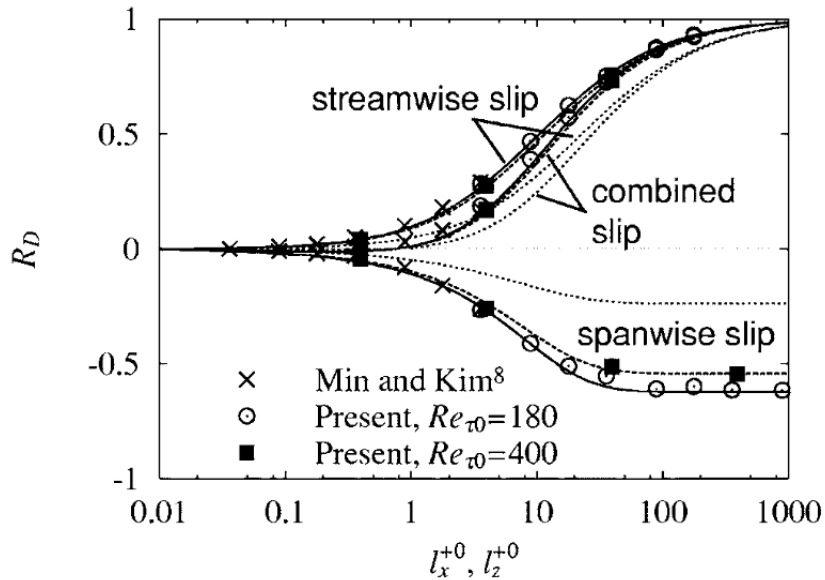


Figure 2.7: Drag reduction rate, R_D , as a function of slip length. Symbols, DNS; lines, present theory solid, $Re_{\tau 0} = 180$; dashed, $Re_{\tau 0} = 400$; dotted, $Re_{\tau 0} = 10^6$.

Min and Kim [27] performed turbulent channel flow simulations at a friction Reynolds number of $Re_{\tau} = H/\nu\sqrt{\tau_w/\rho} = 180$ with an arbitrary, but not unreasonable, slip length boundary, imposed both parallel and perpendicular to the flow direction. In order to delineate the effect of the streamwise and spanwise slip-boundary conditions separately, three different cases are performed: (1) Case 1, streamwise slip only ($u_s \neq 0, w_s = 0$), (2) Case 2, spanwise slip only ($u_s = 0, w_s \neq 0$); and (3) Case 3, slip in both directions ($u_s \neq 0, w_s \neq 0$). A constant mass flow rate is maintained for all cases, and the resulting mean pressure gradient is monitored to infer the skin-friction drag. The fractional change in the drag, DR, is defined as

$$DR = \frac{(-\frac{dp}{dx}) - (-\frac{dp}{dx}|_0)}{-\frac{dp}{dx}|_0} \times 100 \quad (2.12)$$

where $dp/dx|_0$ represents the mean pressure gradient with the no-slip boundary condition.

L_s	L_s^+	u_s^+	Case 1		Case 2		Case 3	
			DR	DR	DR	DR	DR	DR
0.0002	0.036	0.035	0	0	0.035	0	0.035	0
0.0005	0.089	0.088	-1	+1	0.089	-1	0.089	-1
0.001	0.178	0.176	-2	+2	0.177	-2	0.177	-2
0.002	0.357	0.349	-5	+3	0.355	-1	0.355	-1
0.005	0.891	0.845	-10	+8	0.877	-3	0.877	-3
0.01	1.783	1.618	-18	+16	1.707	-8	1.707	-8
0.02	3.566	3.006	-29	+26	3.238	-17	3.238	-17

Figure 2.8: Drag and mean slip velocity variation with slip length. Here, L_s^+ denotes the slip length normalized by the wall shear velocity of no-slip walls u_{τ_0} , and u_s^+ denotes the mean slip velocity normalized by the actual wall shear velocity u_τ .

Figure 2.8 shows the mean skin-friction drag and the mean slip velocity as the slip length varies. It is worth mentioning that the drag in laminar flow decreases with any slip length in the streamwise direction. In turbulent flows, however, the present results show that the slip length, L_s^+ must be larger than 0.2 in order to have noticeable drag reduction. Both the mean slip velocity u_s^+ and the drag reduction are increased as the slip length increases. Note that the mean drag increases when the slip-boundary condition is used in the spanwise direction (Case 2). When the slip boundary condition is used in both directions (Case 3), the reduction is smaller than the one of Case 1, indicating that the drag-reducing effect of the streamwise slip is counter-balanced by the drag increasing effect of the spanwise slip.

Results obtained by permormed DNS are presented here. The profiles of mean velocity u^+ , $(u^+ - u_s^+)$ and fluctuations velocity can be observed in the figures 2.9, 2.10 and 2.11. Min and Kim conclude that, as shown in figure 2.12a, wall-shear stress is smaller with a streamwise slip, and drag reduction is a direct consequence. The strength of near-wall streamwise vortices are enhanced with a spanwise slip as shown in figure 2.12b, which in turn results in a drag increase.

Martell *et al.* [26] investigate the drag-reducing performance of superhydrophobic surfaces (SHS) in turbulent channel flow. Slip velocities, wall shear stresses and Reynolds stresses are considered for a variety of SHS microfeature geometry configurations at a friction Reynolds number of $Re_\tau \sim 180$. As shown in figure 2.13, the top surface of each microfeature is taken to be a no-slip boundary on the liquid, and the suspended liquid-gas interface between the microfeatures is simulated as a flat and shear-free boundary on the liquid. The streamwise and spanwise directions have periodic boundary conditions which approximate infinite parallel plates. While the drag is locally zero on the free surface between the posts or ridges, it is non-zero over the posts and ridges because of the no-slip boundary condition. The net drag is the sum of these two effects and depends on which one dominates. While it is often stated that the drag reduction is a result of smaller wall contact with the fluid, this is an incomplete explanation of the phenomenon, as the spacing between the microfeatures is also critically important. Several ridge and post configurations were examined, where the feature width d and feature spacing w were varied (see figure 2.13).

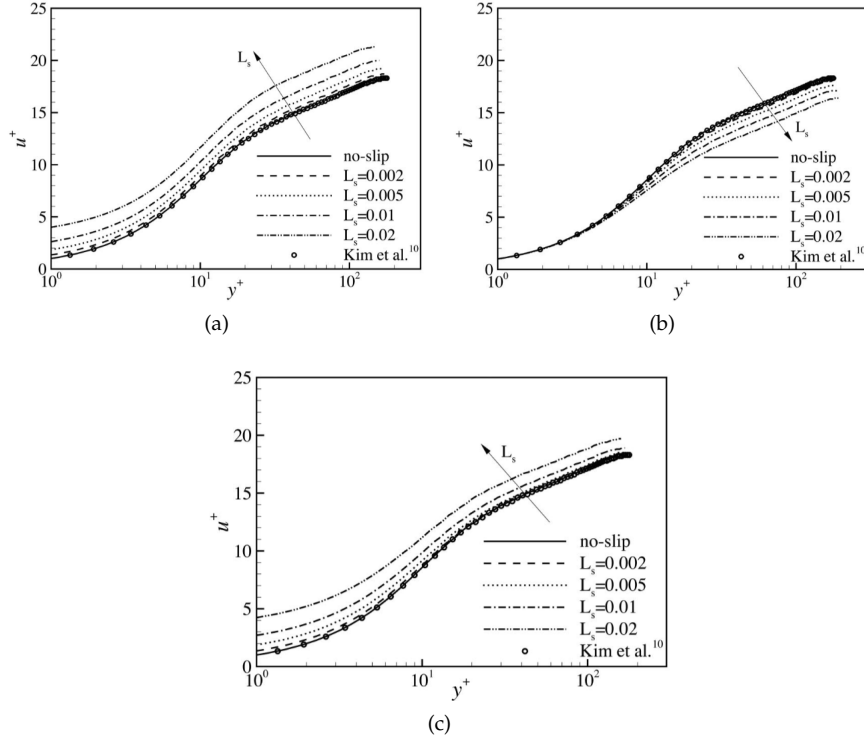


Figure 2.9: Mean velocity profiles, u^+ : (a) Case 1, streamwise slip; (b) Case 2, spanwise slip; (c) Case 3, combined slip.

The slip and drag reduction properties of the SHS, obtained by Martell *et al.*, are summarized in figure 2.14. A higher drag reduction performance is obtained with increased feature spacing. This trend is consistent for both ridges and posts, as the slip velocity attains a maximum nearly 65% of the bulk velocity for ridges and over 75% of the bulk velocity for posts, with a width to spacing ratio d/w just above 0.3. Ridge width to spacing ratios of about $d/w = 1$, achieved higher slip, with larger microfeature widths and gaps. This is clearly seen in figure 2.14 (a), where the slip velocity for $15\mu\text{m} - 15\mu\text{m}$ ridges is nearly 40% lower than the slip velocity for the $30\mu\text{m} - 30\mu\text{m}$ ridges. A similar trend is found in figure 2.14 (b), where the bottom wall shear stress lowering for the $15\mu\text{m} - 15\mu\text{m}$ ridges is nearly 30% smaller than that for $30\mu\text{m} - 30\mu\text{m}$ ridges. This result shows that the actual size of the features, and not simply the ratio of width to spacing (or the percentage of shear-free surface on the SHS), plays an important role in the surface's drag reduction. Smaller features lead to diminished drag-reduction performance.

Türk *et al.* [37] conduct a series of DNS of turbulent flow over a superhydrophobic surface SHS carrying streamwise straight grooves at $\text{Re}_\tau = 180$. The SHS is modelled as alternating free-slip and no-slip boundary conditions, and the spanwise periodicity L is systematically changed in order to investigate its influence on the turbulence dynamics and the resultant gain. In contrast to previous studies, they perform DNS of turbulent channel flow including superhydrophobic boundary conditions on both channel walls under CPG

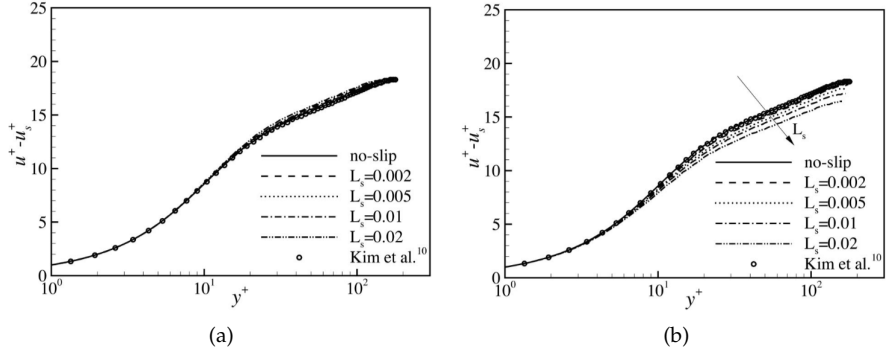


Figure 2.10: Mean velocity profiles, $u^+ - u_s^+$: (a) Case 1, streamwise slip; (b) Case 3, combined slip.

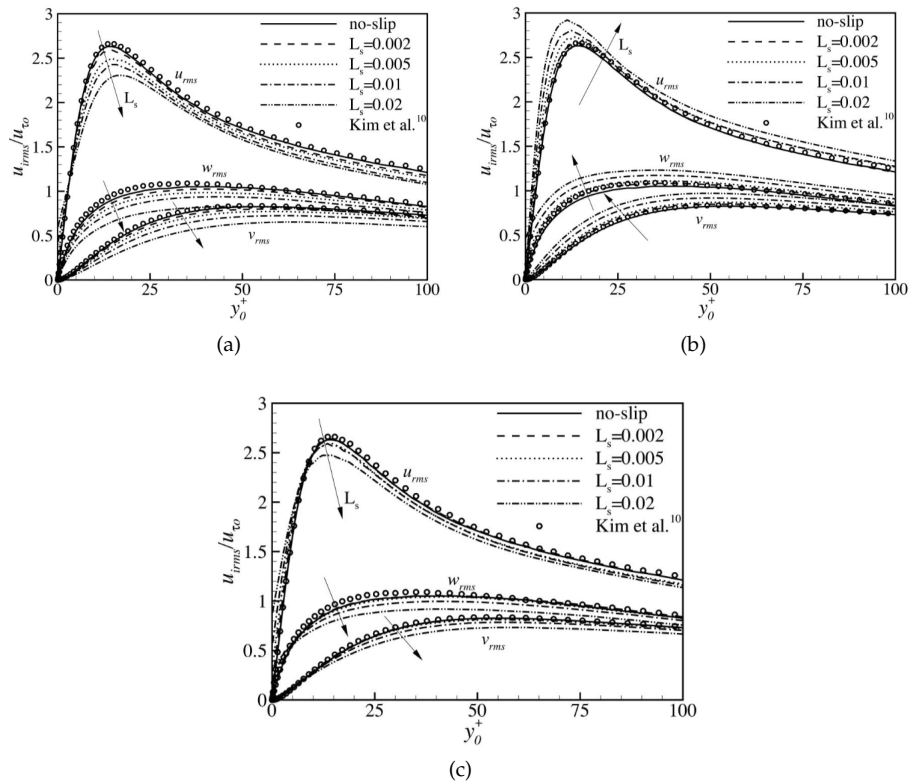


Figure 2.11: The velocity fluctuations normalized by u_{τ_0} : (a) Case 1, streamwise slip; (b) Case 2, spanwise slip; (c) Case 3, combined slip.

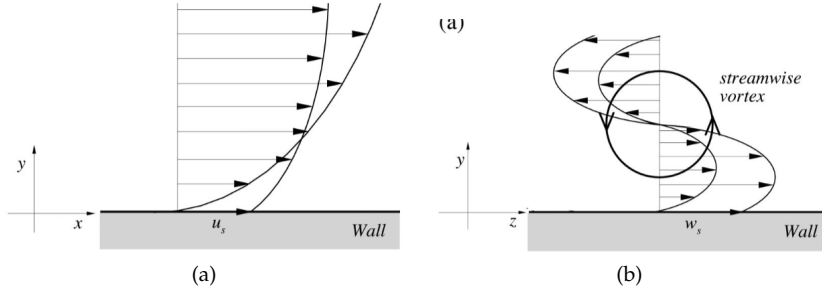


Figure 2.12: A schematic representation of drag decrease and increase mechanism: (a) drag decreases with a streamwise slip velocity (x - y plane); (b) drag increases with a spanwise slip velocity (y - z plane).

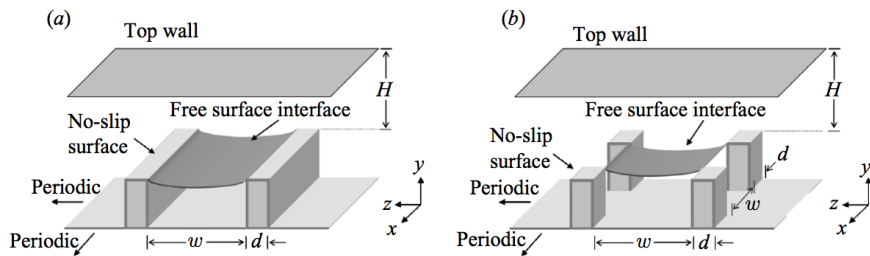


Figure 2.13: Schematic representations of the SHSs containing (a) ridges and (b) posts, arranged on a plane with periodic boundary conditions. The posts are square and spaced evenly in the streamwise (x) and spanwise (z) directions.

conditions. This set-up, for which the wall shear stress and thus Re_τ is kept constant on both channel walls, ensures the absence of relaminarization effects and the gain of SHS is given by an increase in flow rate. In addition to the results obtained from the DNS, their study is also focused on the presence of turbulent structure at the wall. The alternating free-slip and no-slip boundary condition causes a spanwise inhomogeneity which induces a secondary flow of Prandtl's second kind, characterized by steady streamwise roll cells (see 2.15 (a)). For large free-slip areas, the occurrence of tertiary vortices with opposed rotational direction is observed. The influence of the induced secondary motions on slip length l_s is found to be significant only when tertiary vortices occur (see 2.15 (b)).

2.3.2 Experimental Data

Daniello *et al.* [8] perform an experiment to investigate the drag reduction. They used a rectangular flow cell with smooth and superhydrophobic PDMS walls with $30\mu\text{m}$ and $60\mu\text{m}$ wide microridges spaced $30\mu\text{m}$ and $60\mu\text{m}$ apart, respectively. They performed pressure-drop measurements, as well as PIV measurements, to investigate the drag reducing ability of superhydrophobic surfaces in turbulent flows at Reynolds numbers between $2000 < \text{Re} < 10000$. A typical set of velocity profiles, resulting from PIV near the superhydrophobic wall for the $60 - 60$ ridge surface is shown in figure 2.16a for a range of

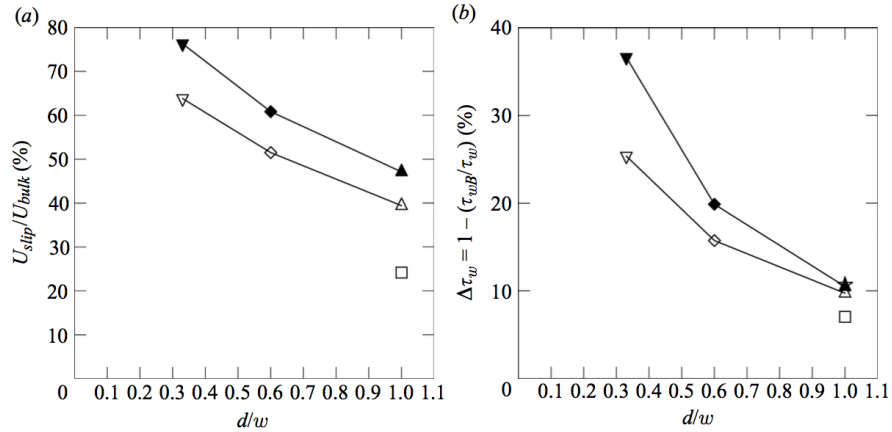


Figure 2.14: Turbulent drag reduction performance of the SHS for both ridges and posts as a function of the width to spacing ratio. **(a)** Slip velocity at the SHS normalized by the bulk velocity for varying feature width and spacing. **(b)** Wall shear stress reduction at the SHS, normalized by the average wall shear stress, for varying feature width and spacing. The data include 15μm – 15μm (□), 30μm – 30μm (△), 30μm – 50μm (◊) and 30μm – 90μm (▽) ridges, as well as 30μm – 30μm (▲), 30μm – 50μm (◆) and 30μm – 90μm (▼) posts. For example a ridge which is 30μm wide and spaced at 50μm is a '30μm – 50μm ridge'.

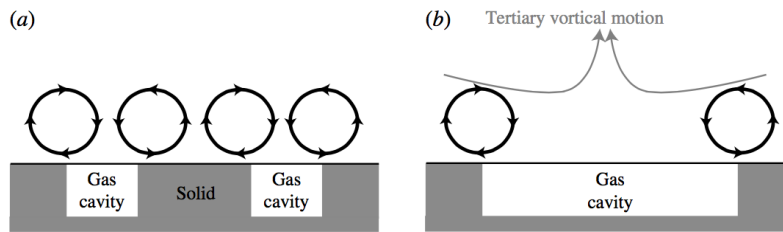


Figure 2.15: Schematic secondary flow mechanism over SHS with **(a)** small and **(b)** large groove width.

Reynolds number between $2700 < Re < 8200$; and for the 30 – 30 ridge case as seen in figure 2.16b. The effect of the superhydrophobic wall is not observed for the low Reynolds number experiments.

The turbulent drag reduction, $DR = (\tau_{no-slip} - \tau_{SH})/\tau_{no-slip}$, was computed as the percent difference in shear stress at the superhydrophobic and no-slip wall and it is shown in figure 2.17, as a function of Reynolds number. The slip length calculated from PIV data is insignificant in the laminar region and reaches a maximum value greater than $b = 70\mu\text{m}$ for 30 – 30 and greater than $b = 120\mu\text{m}$ for 60 – 60 ridges. In the present experiments, a maximum drag reduction of approximately 50% was observed for both micro-ridge geometries, once a suitably high Reynolds number was achieved. Reduction is initiated at a critical Reynolds number in the turbulent regime. For the micro-ridges under consideration, the critical Reynolds number was determined to be $Re_{crit} \approx 2500$.

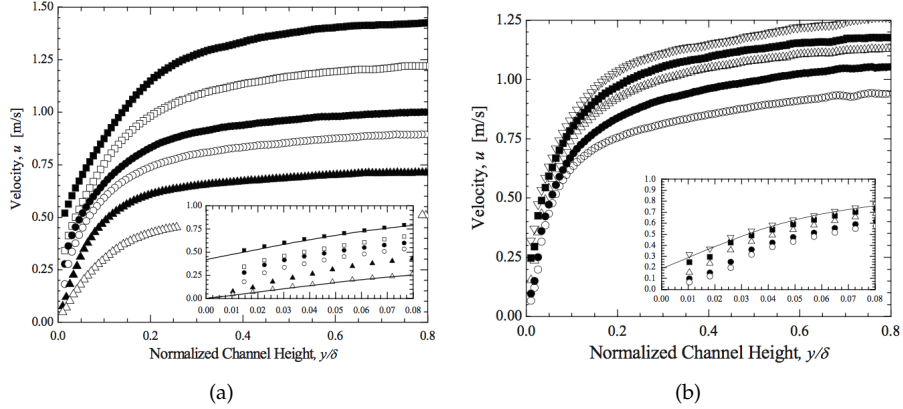


Figure 2.16: **(a)** Velocity profiles over a microridge surface $w = 60\mu\text{m}$ $d = 60\mu\text{m}$ showing the development of significant slip velocities with increasing Reynolds number from 2700(\triangle) to 8200(\blacksquare). (Inset) Velocity profiles near the wall demonstrating prominent slip velocities. Reynolds numbers are 2700(\triangle), 3900(\blacktriangle), 4840(\lozenge), 5150(\blacklozenge), 6960(\square), and 8200(\blacksquare). **(b)** Velocity profiles over the $w = 30\mu\text{m}$ $d = 30\mu\text{m}$ microridge surface demonstrate slip velocity behaviour consistent with that observed on the $60 - 60$ surface, but reduced in magnitude. Reynolds numbers range from 4970(\circ) to 7930(\triangledown). Larger feature spacing performs better for a given Reynolds number. Reynolds numbers are 4970(\circ), 5400(\blacklozenge), 6800(\triangle), 7160(\blacksquare), and 7930(\triangledown).

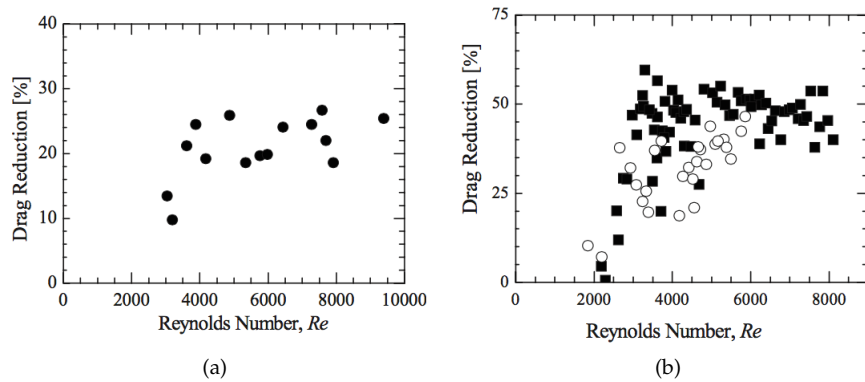


Figure 2.17: Drag reduction as a function of Reynolds number for a channel with **(a)** a single superhydrophobic wall $w = 30\mu\text{m}$ $d = 30\mu\text{m}$ (\bullet) and **(b)** two superhydrophobic walls containing $w = 30\mu\text{m}$ $d = 30\mu\text{m}$ microridges (\circ) and $w = 60\mu\text{m}$ $d = 60\mu\text{m}$ microridges (\blacksquare).

This Reynolds number is near or just past the transition boundary to turbulent flow. This observation, along with the noted lack of drag reduction in the laminar regime, suggests that the underlying physical cause of the observed effect must relate to the unique structure of wall-bounded turbulent flow. The physical origins of the critical Reynolds number for the onset of drag reduction can be understood by analyzing the relevant length scales in the flow. If the drag reduction and the slip length were dependent on the micro-ridge geometry and channel dimensions alone, as is the case in laminar flows, then one would expect to find the reduction and slip length to be independent of Reynolds number. In turbulent flows, however, there is a third length scale of importance, i.e. the thickness of the viscous sublayer which extends out to $y^+ = 5$. Although the viscous sublayer thickness remains fixed in wall units, in dimensional form the thickness of the viscous sublayer decreases with increasing Reynolds number as $y_{vsl} = 5\sqrt{\rho/\tau_w}$. Close to the wall, where viscous stresses dominate, the analytical solutions of Philip *et al.* [29] show that the influence of the shear-free air-water interface extends to a distance roughly equal to the micro-ridge spacing, w , into the flow. Thus, a superhydrophobic surface can impact on the turbulent flow, if the micro-ridge spacing approaches the thickness of the viscous sublayer, $w \approx y_{vsl}$, or in other words, $w^+ = y^+ = 5$. Figure 2.18 shows that the behaviour of micro-feature spacing for the 30–30 and the 60–60 surfaces under study. The w^+ values are calculated from shear stress measured at the superhydrophobic surface. This means that the micro-feature spacing is minimally 15%–50% of viscous sublayer thickness almost immediately after the turbulent transition. Hence for 30–30 and 60–60 ridges, drag reduction is noticed almost as soon as a turbulent flow develops. As the Reynolds number increases and the thickness of the viscous sublayer is further reduced, the presence of the superhydrophobic surface will more strongly influence the velocity profile within the viscous sublayer and reduce the momentum transferred from the fluid to the wall and the vorticity of the fluid at the edge of the viscous sublayer. Turbulence intensity is thereby reduced, increasing the drag reduction. Therefore one expects that saturation of the turbulent drag reduction is likely in the limit of very large Reynolds numbers, where the micro-ridges are much larger than the viscous sublayer. In this limit, the drag reduction should approach a limit of $D_R = w/(w + d)$, as momentum is only transferred from the solid fraction of the superhydrophobic surface and the viscous sublayer is thin enough, so that the no-slip and shear-free portions of the surface can be considered independently. For the present shear-free area ratios, this limit would be 50%. Drag reduction results, shown in figure 2.17, appear consistent with this hypothesis, the 60–60 ridges already appearing to plateau. As the critical Reynolds number will decrease with increasing feature spacing, coarser superhydrophobic surfaces will begin to perform better at lower Reynolds numbers. It is therefore expected that equivalent drag reduction performance will be accessible to much finer micro-feature spacings at higher Reynolds numbers. With fine superhydrophobic surfaces, little drag reduction may be evident until the viscous sublayer shrinks significantly, well beyond the transition.

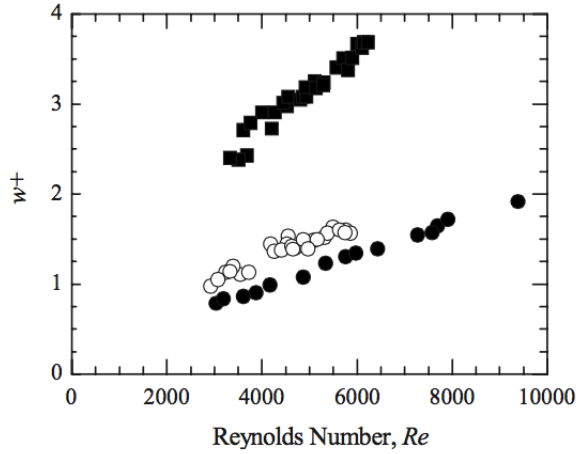


Figure 2.18: The microridge spacing in wall units, w^+ , as a function of Reynolds number. The data are taken from PIV measurements from a channel with a single superhydrophobic surface of $w = 30\mu\text{m}$ and $d = 30\mu\text{m}$ microridges (●) and from pressure measurements for flow through a channel with two superhydrophobic walls containing $w = 30\mu\text{m}$ and $d = 30\mu\text{m}$ microridges (○) and $w = 60\mu\text{m}$ and $d = 60\mu\text{m}$ microridges (■). A spacing of $w^+ = 5$ corresponds to the thickness of the viscous sublayer. Only points in the turbulent regime are shown.

2.4 INTERFACE LIQUID-GAS

In general, the deformation (shown in figure 2.19), of the interface responding to the pressure difference, as an equivalent way of representing the pressure distribution on the wall. The deformation of the interface obeys the Young-Laplace equation is

$$\nabla^2 \eta \approx \frac{P_{\text{liquid}} - P_{\text{gas}}}{\sigma} \quad (2.13)$$

where σ is the surface tension and η is the interface height measured from the channel wall plane at $y^+ = 0$. Starting from this general view, it is interesting to analyse the behaviour of the interface. So one raise the following questions: does a superhydrophobic surface induce a different pressure field compared to a flat surface? If so, how does this difference scale with system parameters, and when does it become significant that it can deform the air-water interface and potentially rupture the entrapped gas pockets?

Seo *et al.* [36] have performed DNS of turbulent channel flows subject to superhydrophobic surfaces over a wide range of texture sizes spanning values. The results show that the larger texture size intensifies the contribution of stagnation pressure, while the contribution from turbulence is essentially insensitive to L^+ . The scaling of the induced pressure and the consequent deformations of the air-water interface are analysed. Based on their results, an upper bound on the texture wavelength is quantified, that limits the range of robust operation of superhydrophobic surfaces when exposed to high-speed flows. They also investigated pressure fluctuations in terms of two modes: an

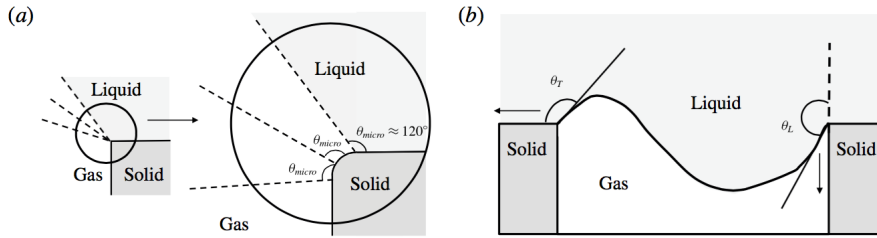


Figure 2.19: (a) Macroscopic corner angle and microscopic contact angle under the pinned interface assumption. (b) Corner angles at the trailing edge and leading edge.

unsteady turbulent mode and a steady coherent mode solely controlled by the texture geometry. While the pressure magnitude of the turbulent mode is of the same order as that in a smooth-wall turbulent boundary layer, the pressure field associated with the texture geometry was shown to increase significantly with the texture size. Particularly for a three-dimensional post geometry, this pressure increase was more significant (in comparison to two-dimensional stream-wise ridges) due to the stagnation of slip velocity with the edge of the posts. They showed that the coherent pressure field has a self-similar behaviour for a wide range of L^+ , and that it scales linearly with the slip velocity. Lastly, they analysed the interface deformation due to the resulting pressure fields and predicted threshold conditions for interface failure and transition to the Wenzel state. Combining the knowledge of pressure fluctuations and interface deformation, it becomes clear that the implementation of large textures can deteriorate the stability of the gas pockets.

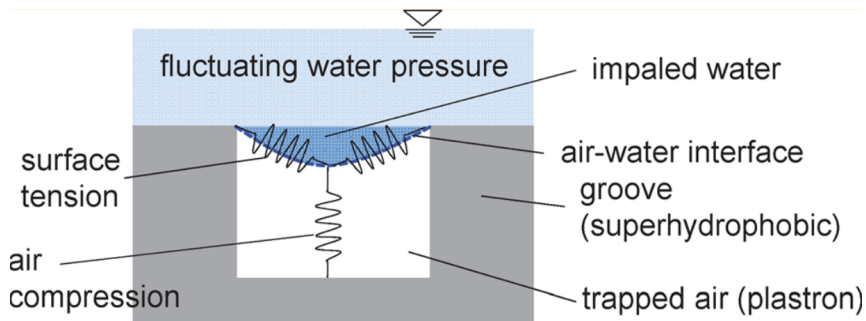


Figure 2.20: Interface model.

Piao *et al.* [30] conduct a study on the interface liquid-gas of superhydrophobic surface (see figure 2.20). They performed a theoretical analysis to investigate the collapse transition and estimate the plastron longevity on SHS having micro-scaled grooves under the fluctuating water pressure and the diffusion of the trapped air, while considering various variables such as immersion depth, surface parameters, and fluctuating water pressure conditions. The dependence of the plastron longevity on surface geometry is found. The plastron on a narrow groove width ($\leq 5\mu\text{m}$) lasts days, while that with a wider one ($\geq 35 - 45\mu\text{m}$), is more susceptible to the pressure fluctuation, and lasts a

shorter time. While the increase of amplitude of fluctuation has a negative effect on the plastron longevity, the increase of fluctuating frequency (below the mechanical resonance frequency of the plastron) tends to slightly mitigate the reduction of lifetime, by contributing to the viscous damping. Finally, as a countermeasure to the fluctuating water pressure, it is suggested that the enhanced advancing contact angle of the groove sidewall mitigates the negative effects.

Part II
TURBULENCE

3

TURBULENCE

Most flows encountered in engineering practice and in nature are turbulent. The boundary layer on an aircraft wing is likely to be turbulent, the atmospheric boundary layer over the earth surface is turbulent, as well as the major oceanic currents. In spite of our everyday experience with it, turbulence is not easy to define precisely. An important characteristic is its ability to transport and mix fluid much more effectively than a comparable laminar flow. This is well demonstrated by an experiment first reported by Osborne Reynolds [32] (1883). Dye is steadily injected on the centreline of a long pipe in which water is flowing. As Reynolds later established, this flow is characterised by a single non-dimensional parameter, now known as the Reynolds number Re . In general, it is defined by $Re = UL/\nu$, where U and L are characteristic velocity and length scales of the flow, and ν is the kinematic viscosity of the fluid. In the Reynolds' pipe-flow experiment (as shown in figure 3.1) if Re is less than about 2300 the flow is laminar, the fluid velocity does not change with time, and all streamlines are parallel to the axis of the pipe. However if Re exceeds about 4000, then the flow is turbulent. Close to the injector, the dye streak is jiggled about by the turbulent motion; it becomes progressively less distinct with downstream distance; and eventually mixing with the surrounding water reduces the peak dye concentration to the extent that is no longer visible.

3.1 SOME CHARACTERISTICS

As previously mentioned, it is difficult to arrive at one general definition of the turbulence. Thus it is necessary to extract some general characteristics of this phenomenon:

- *Randomness*: Turbulent flows seem irregular, chaotic, and unpredictable.
- *Nonlinearity*: Turbulent flows are highly nonlinear. In unstable flows small perturbations grow spontaneously and frequently equilibrate as finite amplitude disturbances. The nonlinearity of turbulent flow results in vortex stretching, a key process in which three-dimensional turbulent flows maintain their vorticity.
- *Diffusivity*: Due to macroscopic mixing of fluid particles, turbulent flows are characterised by a rapid rate of diffusion of momentum and heat.
- *Vorticity*: Turbulence is characterised by high levels of fluctuating vorticity. The identifiable structures in a turbulent flow are vaguely called *eddies*. A characteristic feature of turbulence is the existence of an enormous range of eddy sizes. The large eddies have a size of order of the width of the region of turbulent flow. The large eddies contain most of the energy. The energy is handed down from large to small eddies by nonlinear interactions, until it is dissipated by viscous diffusion in the smallest eddies whose size is of the order of millimeters.

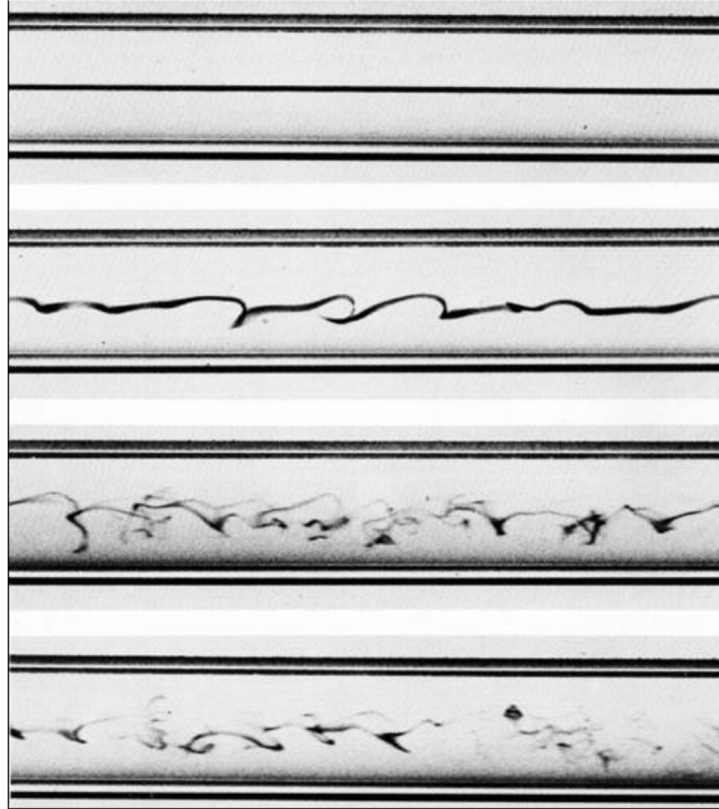


Figure 3.1: *Reynolds' experiment*: in the first sequence the fluid is laminar, in the second one there is transition and in the last two the fluid is fully turbulent.

- *Dissipation*: The vortex stretching mechanism transfers the energy and vorticity to increasingly smaller scales, until the gradients become so large that they are dissipated by viscosity. Turbulent flows therefore require continuous supply of energy to make up for the viscous losses.

3.2 AVERAGES

The variables in a turbulent flow are not deterministic in details and have to be treated as stochastic or random variables. Let $u(t)$ be any measured variable in a turbulent flow. Consider first the case when the "average characteristics" of $u(t)$ do not vary with time (figure 3.2a). In such a case we can define the average variable as the time mean

$$\langle u \rangle \equiv \lim_{t_0 \rightarrow \infty} \frac{1}{t_0} \int_0^{t_0} u(t) dt \quad (3.1)$$

Now consider a situation in which the average characteristics do vary with time. An example is the decaying series shown in figure 3.2b, which could represent the velocity of a jet as the pressure in the supply tank falls. In this case the average is a function of time and cannot be formally defined by using equation (3.1), because it cannot be specified how large the averaging interval t_0 should be made in evaluating the integral (3.1). If t_0 is very large then

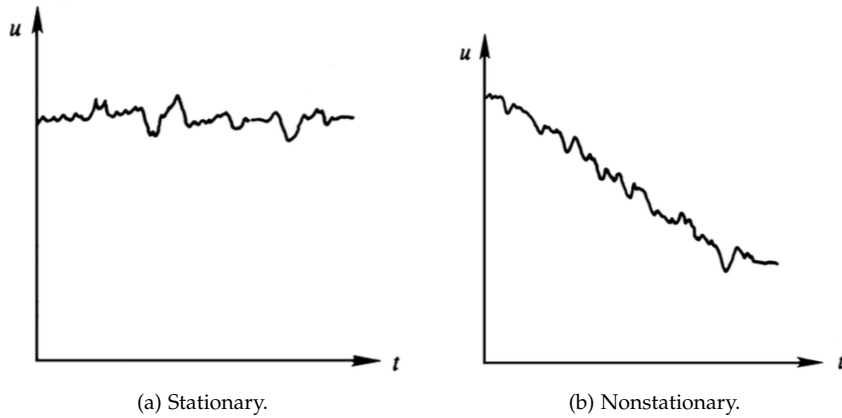


Figure 3.2: Stationary and non-stationary time series.

it may not get a "local" average, and if t_0 is very small then it may not get a reliable average. In such a case, however, one can still define an average by performing a large number of experiments, conducted under identical conditions. A collection of experiments, performed under an identical set of experimental conditions, is called an ensemble, and an average over the collection is called an ensemble average, or expected value. If the i -th record is denoted by $u^i(t)$, therefore defined the ensemble average of u at time t to be

$$\langle u \rangle \equiv \frac{1}{N} \sum_{i=0}^N u^i(t) \quad (3.2)$$

As there is no way of controlling natural phenomena in the atmosphere and the ocean, it is very difficult to obtain observations under identical conditions. Consequently, in a non-stationary process such as the one shown in figure 3.2b, the average value of u at a certain time is sometimes determined by using equation (3.1) and choosing an appropriate averaging time t_0 , small compared to the time during which the average properties change appreciably. The various averages of a random variable, such as its *mean* and *rms* values, are collectively called the statistics of the variable. When the statistics of a random variable are independent of time, we say that the underlying process is stationary. For a stationary process the time average (i.e., the average over a single record, defined by equation (3.1)) can be shown to equal the ensemble average, resulting in considerable simplification. Similarly, we define a homogeneous process as one whose statistics are independent of space, for which the ensemble average equals the spatial average.

3.3 MEAN-FLOW EQUATIONS

The most basic equation which governs the mean velocity field $\langle u(\vec{x}, t) \rangle$, can be derived starting from the *Reynolds' decomposition* of velocity field which can be written as a two different contributes: mean and fluctuation velocity

$u(\vec{x}, t) = \langle u(\vec{x}, t) \rangle + \bar{u}'(\vec{x}, t)$. Considering the *Navier-Stokes equations* in non-dimensional form, the instantaneous velocity field $u(\vec{x}, t)$ is expressed as

$$\nabla \cdot \vec{u} = 0 \quad (3.3a)$$

$$\frac{\partial \vec{u}}{\partial t} + \nabla(\vec{u} \otimes \vec{u}) = -\nabla p + \frac{1}{Re} \nabla^2 \vec{u} + \frac{f_g}{Fr^2} \quad (3.3b)$$

where $Fr = u_0 / \sqrt{f_0 L_0}$ is the *Froude number* defined as the ratio of the flow inertia to the external field. Averaging the Equation (3.3), one gets

$$\nabla \cdot \langle \vec{u} \rangle = 0 \quad (3.4a)$$

$$\frac{\partial \langle \vec{u} \rangle}{\partial t} + \langle \vec{u} \rangle \cdot \nabla \langle \vec{u} \rangle = -\nabla \langle p \rangle + \frac{1}{Re} \nabla^2 \langle \vec{u} \rangle + \frac{\langle f_g \rangle}{Fr^2} + \nabla \cdot T_r \quad (3.4b)$$

T_r is called *Stress Reynolds Tensor* and it is defined as $T_r = -\langle \vec{u}' \otimes \vec{u}' \rangle$. It is important to notice that new equation (3.4) seems to be very similar to old one (3.3); but the presence of *Stress Reynolds Tensor* makes the things complex, as the difficulties about the turbulence study lie on it. The *Stress Reynolds Tensor* is an additional unknown variable like the mean velocity and the pressure. Therefore four scalar equations for ten scalar unknown variables (the tensor is symmetric) are given. In this case the system is not close and an additional equation for the *Stress Reynolds Tensor* is required. This problem is called *The closure problem*, and it is a typical behaviour of the non linear equations. If the non linearity is weak, then $\vec{u}' \ll \langle \vec{u} \rangle$, so the problem can be overcome; if the turbulence terms \vec{u}' and $\langle \vec{u} \rangle$ are of the same order, the treatise is more difficult.

3.4 THE ENERGY CASCADE

The idea of the *energy cascade* (introduced by Richardson in 1922) is that kinetic energy enters the turbulence, through the production mechanism, at the largest scales of motion. This energy is then transferred, by an inviscid process, to smaller and smaller scale, until at the end, it is dissipated by viscous actions. Richardson's view of the energy cascade is that the turbulence can be considered to be composed by *eddies* of different sizes. Eddies of size ℓ have a characteristic velocity $u(\ell)$ and timescale $\tau(\ell) \equiv \ell/u(\ell)$. An eddy has not a precise definition, but it is conceived to be a turbulent motion, localised within a region of size ℓ , at least moderately coherent over this region. The region occupied by a large eddy can also contain smaller eddies. Richardson's notion is that the large eddies are unstable and break up, transferring their energy to somewhat smaller eddies. Those with the largest size range are characterised by the lengthscale ℓ_0 which is comparable to the flow scale L , and their characteristic velocity $u_0 \equiv u(\ell)$ is of the order of the r.m.s turbulence intensity (k), $u_{r.m.s} \equiv \sqrt{2/3k}$, which is comparable to U . These smaller eddies undergo a similar break-up process, and transfer their energy to yet smaller eddies. This cascade, in which energy is transferred to successively smaller and smaller eddies, continues until the Reynolds number $Re(\ell) \equiv u(\ell)\ell/\nu$ is sufficiently small that the eddy motion is stable, and molecular viscosity is effective in dissipating the kinetic energy. Richardson studied the energy cascade in a very qualitative way because adequate mathematical tools were not yet available to describe the phenomena.

3.5 THE KOLMOGOROV HYPOTHESES

Questions about the energy cascade and turbulence scales (see figure 3.3) are answered by Kolmogorov (1941) in the form of three hypotheses. The first one concerns the isotropy of the small-scale motions. In general, the large eddies are anisotropic and are affected by the boundary conditions of the flow. Kolmogorov argued that the directional biases of the large scales are lost in the chaotic scale reduction process, by which energy is transferred to successively smaller and smaller eddies.

Kolmogorov's hypothesis of local isotropy. At sufficiently high Reynolds number, the small-scale turbulent motions ($\ell \ll \ell_0$) are statistically isotropic.

It is useful to introduce a lengthscale ℓ_{EI} as the demarcation between the anisotropic large eddies ($\ell > \ell_{EI}$) and the isotropic small eddies ($\ell < \ell_{EI}$). In the energy cascade (for $\ell < \ell_{EI}$) the two dominant processes are the transfer of energy to successively smaller scales, and viscous dissipation. The important parameters are the rate at which the small scale scales receives the energy from the large scales T_{EI} and the kinematic viscosity ν . The dissipation rate ε is determined by the energy transfer rate T_{EI} , so that these two rates are nearly equal $\varepsilon \approx T_{EI}$. Consequently, the hypothesis that the statistically universal state of the small scales is determined by ν and the rate of energy transfer from the large scales T_{EI} can be stated as:

Kolmogorov's first similarity hypothesis. In every turbulent flow at sufficiently high Reynolds number, the statistics of the small-scale motions ($\ell < \ell_{EI}$) have a universal form that is uniquely determined by ν and ε .

The size range is referred to as the *universal equilibrium range*. Given the two parameters ν and ε , there are unique length, velocity, and time scales that can be formed

$$\eta \equiv \left(\frac{\nu^3}{\varepsilon} \right)^{\frac{1}{4}} \quad (3.5)$$

$$u_\eta \equiv (\nu \varepsilon)^{\frac{1}{4}} \quad (3.6)$$

$$\tau_\eta \equiv \left(\frac{\nu}{\varepsilon} \right)^{\frac{1}{2}} \quad (3.7)$$

The Reynolds number based on Kolmogorov scales equals unity ($\eta u_\eta / \nu = 1$), which is consistent with the notation that the cascade proceeds to smaller and smaller scales as long as the Reynolds number $u_\ell \ell / \nu$ is small enough for dissipation to be effective. The dissipation rate is given by

$$\varepsilon = \nu \left(\frac{u_\eta}{\eta} \right)^2 = \frac{\nu}{\tau_\eta^2} \quad (3.8)$$

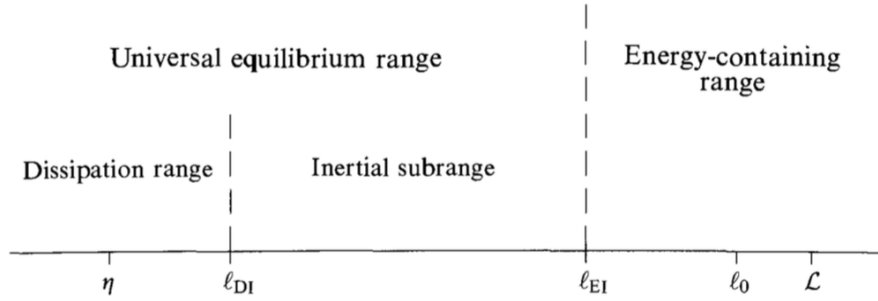


Figure 3.3: Scales of turbulence.

The ratios of the smallest to largest scales are determined from the definitions of Kolmogorov scales and from the scaling $\varepsilon \sim u_0^3/\ell_0$. The results are

$$\frac{\eta}{\ell_0} \sim Re^{-\frac{3}{4}} \quad (3.9)$$

$$\frac{u_\eta}{u_0} \sim Re^{-\frac{1}{4}} \quad (3.10)$$

$$\frac{\tau_\eta}{\tau_0} \sim Re^{-\frac{1}{2}} \quad (3.11)$$

The ratio η/ℓ_0 decreases with increasing Re . As a consequence, at sufficiently high Reynolds number, there is a range of scales ℓ that are very small compared with ℓ_0 , and yet very large compared with η , $\ell_0 \gg \ell \gg \eta$. Since eddies in this range are much bigger than the dissipative eddies, it may be supposed that their Reynolds numbers $\ell u(\ell)/\nu$ are large, and consequently that their motions are partially affected by viscosity. Hence the first similarity hypothesis,

Kolmogorov's second similarity hypothesis. In every turbulent flow at sufficiently high Reynolds number, the statistics of the motion of the scale ℓ in the range $\ell_0 \gg \ell \gg \eta$ have a universal form that is uniquely determined by ε independent of ν .

It is convenient to introduce a lengthscale ℓ_{DI} , so that the range in the above hypothesis can be written $\ell_{EI} > \ell > \ell_{DI}$. This lengthscale ℓ_{DI} splits the *universal equilibrium range* ($\ell < \ell_{EI}$) into two subranges: the *inertial subrange* ($\ell_{EI} > \ell > \ell_{DI}$) and the *dissipation range* ($\ell < \ell_{DI}$). According to the second similarity hypothesis, motions in the inertial subrange are determined by inertial effects (viscous effects being negligible) whereas only motions in the dissipation range experience significant viscous effects, and so are responsible for the dissipation.

3.5.1 The Energy spectrum

To formulate the energy spectrum, which is based on the hypotheses previously introduced, the starting point is the *De Karman-Howarth equation* [9]. By applying the *Fourier's transform* to De Karman-Howarth equation, making use of the *Wiener-Khinchin theorem* [19], one can write an equation of the energy

spectral density which depends on the vector of numbers waves $\vec{\kappa}$. A scalar equation is obtained, independent from vector $\vec{\kappa}$, a 1D-equation function only of $|\vec{\kappa}|$

$$\frac{\partial \hat{E}_{1D}}{\partial t} + \frac{d\hat{T}_{1D}}{d\kappa} = -2\nu\kappa^2\hat{E}_{1D} + \hat{\Pi}_{1D} \quad (3.12)$$

where the second term of left side of Equation (3.12) is the dissipation, $\hat{\Pi}_{1D}$ is the input of power i.e. where the force acts, and \hat{T}_{1D} is the power spectral transfer as shown in Figure 3.5. It is important to analyse the shape of \hat{E}_{1D} .

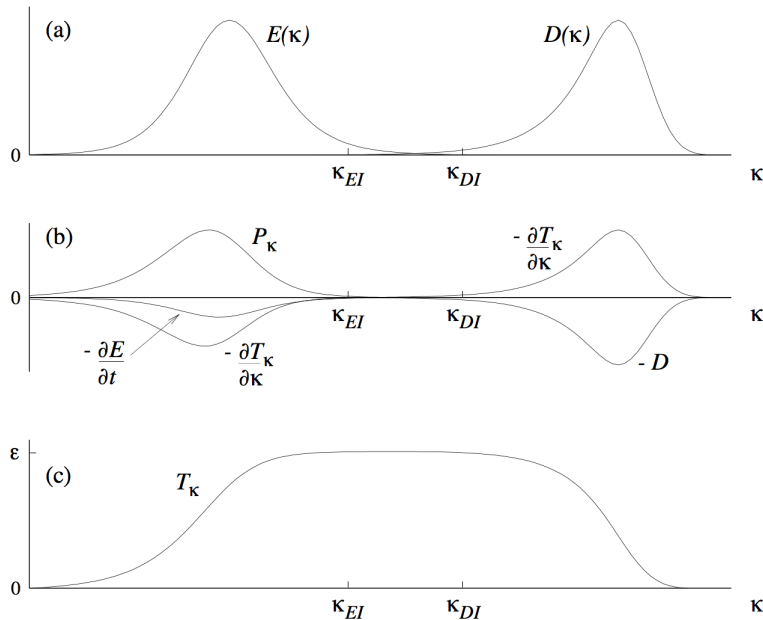


Figure 3.4: Homogeneous turbulence at very high Reynolds number, sketches of (a) the energy and dissipation spectra, (b) the contributions to the balance of equation (3.12), and (c) the spectral energy transfer rate.

Through a dimensional analysis $\hat{E}_{1D} = \hat{E}_{1D}(\kappa, \rho_0, \mu, \varepsilon, \kappa_0)$, if $\eta = (\nu^3/\varepsilon)^{1/4}$, and \hat{E}_{1D} can be expressed as

$$\hat{E}_{1D} = \hat{E}_{1D}(\kappa, \rho_0, \nu, \eta, \kappa_0) \implies \hat{E}_{1D}(\kappa\eta, \rho_0, \nu, \eta, \kappa_0\eta) \quad (3.13)$$

in non-dimensional form. Taking into account the dimension of $[\hat{E}_{1D}] = [U^2 L]$ and $[U] = ([\varepsilon][L])^{1/3}$, the *Buckingham theorem* leads to

$$\hat{E}_{1D} = \varepsilon^{\frac{2}{3}} \kappa^{-\frac{5}{3}} \hat{E}_{1D}^*(\kappa\nu, \kappa_0\nu) \quad (3.14)$$

Focusing the attention on the inertial subrange, \hat{E}_{1D}^* is equal to C_κ called *Kolmogorov's constant*. It is constant because in this range acts neither power input nor dissipation, thus the *energy spectrum law*, as shown in figure 3.5, is

$$\hat{E}_{1D} = C_\kappa \varepsilon^{\frac{2}{3}} \kappa^{-\frac{5}{3}} \quad (3.15)$$

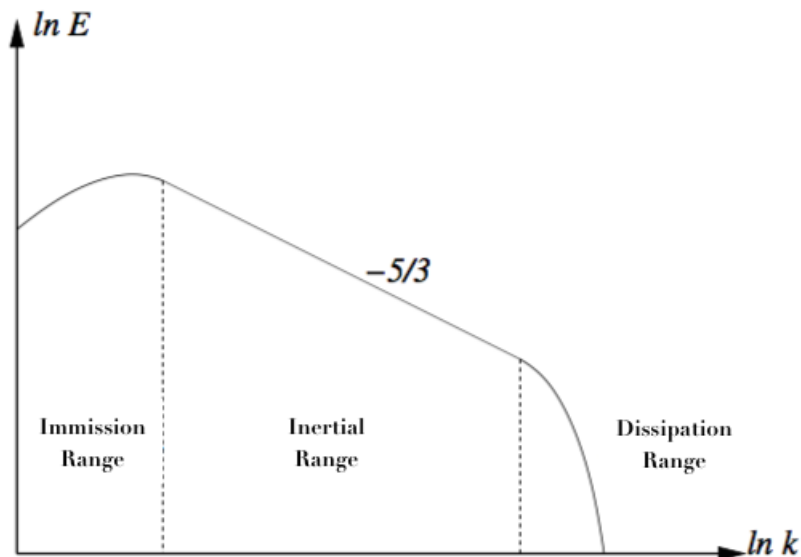


Figure 3.5: Energy cascade.

It must be emphasized that the *inertial range* is independent from the characteristics of the flux (macroscopic scale) and fluid (chemical-physical properties). The study of turbulence has to focus on this range for its universal behaviour. The validation of *Kolmogorov's hypothesis* implies that the macroscopic and microscopic scales have to be distinguished. Therefore the Re number has to be large, as suggested by the relation $L/\eta \propto Re^{3/4}$. So, the macroscopic zone contains all anisotropy part of flux i.e. the production of energy, while the microscopic zone is controlled by the viscous force which dissipates the energy derived from *inertial range*.

In conclusion, it is important to underline that there exists a *Landau's objection* to the *Kolmogorov's theory*. Landau discovered that the constant C_K , in the equation (3.15), is not universal for the structure functions of high order but it depends on turbulent production [5]. The error made by Kolmogorov was to consider that the *eddy structures* would fill the entire space in the fluid, making it uniform. Therefore the hypothesis of homogeneity fails: actually, the energy dissipates itself only in some regions of the fluid and not in the entire space. This phenomenon within the fluid, showing turbulent zones alternated to laminar zones, is called *intermittency*.

WALL FLOWS

In general and particularly for the engineering applications, it is important to study turbulent flows in the presence of walls. Two simplest cases are considered here: fully developed channel flow and fully developed pipe flow. These flows are of practical importance and played a prominent role in the historical development of the study of turbulent flows. Central issues are the shape of mean velocity profiles, and the *friction laws*, which describe the shear stress exerted by the fluid on the wall. These flows are extremely important to understand the physics of the engineering problem into the applications.

4.1 CHANNEL FLOW

The case of a flow through a rectangular duct of high $h = 2d$ is presented. The duct is long ($L/d \ll 1$) and has a large aspect ratio ($b/d \ll 1$). The extent of the channel in the spanwise z direction is large compared with d so that the flow is statistically independent of z . Near the entry of the duct ($x = 0$) there is a flow-development region. However, the attention has to focus on the *fully developed* region in which velocity statistics no longer varies with x . Hence the fully developed channel flow can be considered statistically stationary and one-dimensional, with a velocity distribution that depends only on y . The flow is driven by a constant pressure gradient dp/dx along the x direction. The presence of the wall, thanks to viscosity, creates a no-slip boundary condition. It means that there is a zero velocity at the wall. This constraint brings to a zone where the flow is dominated by viscous effects, which is called *boundary*

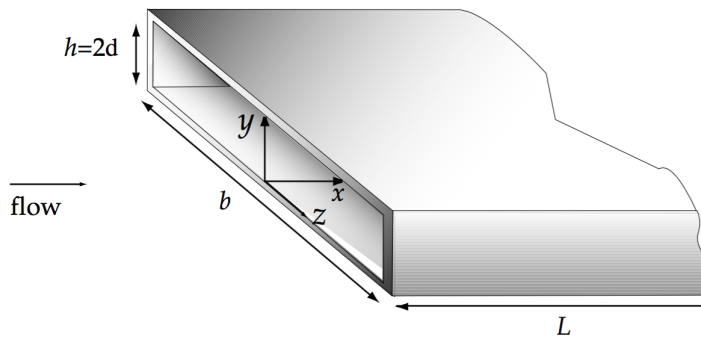


Figure 4.1: Sketch of channel flow.

layer and highly depends on Reynolds' number. The Reynolds numbers used to characterised the flow are

$$\text{Re} = \frac{(2d)\bar{u}}{\nu} \quad (4.1)$$

$$\text{Re}_0 = \frac{du_0}{\nu} \quad (4.2)$$

where $u_0 = \langle u \rangle_{y=d}$ is the *centerline velocity* and the *bulk velocity* u_b is

$$u_b = \frac{1}{d} \int_0^d \langle u \rangle dy \quad (4.3)$$

4.1.1 The mean equations

With the hypotheses makes previously, the set of equations from the channel flow can be written as

- The mean continuity equation becomes

$$\frac{d \langle v \rangle}{dy} = 0 \quad (4.4)$$

since $\langle w \rangle$ is zero, and $\langle u \rangle$ is independent by x . Taking into account the boundary condition for $\langle v \rangle_{y=0} = 0$, so $\langle v \rangle$ for all y .

- The mean-momentum equation along y reduces to

$$0 = -\frac{d \langle v'^2 \rangle}{dy} - \frac{1}{\rho} \frac{\partial \langle p \rangle}{\partial y} \quad (4.5)$$

integrating the equation (4.5) with boundary conditions for $\langle v'^2 \rangle_{y=0} = 0$ and the mean pressure on the bottom wall $p_w = \langle p(x, 0, 0) \rangle$, one obtains

$$\langle v'^2 \rangle + \frac{\langle p \rangle}{\rho} = \frac{\langle p_w(x) \rangle}{\rho} \quad (4.6)$$

The equation (4.6) underlines the fact that the mean axial pressure gradient is uniform across the flow

$$\frac{\partial \langle p \rangle}{\partial x} = \frac{d \langle p_w \rangle}{dx} \quad (4.7)$$

- The mean-momentum equation along x is

$$0 = \nu \frac{d^2 \langle u \rangle}{dy^2} - \frac{\langle u'v' \rangle}{dy} - \frac{1}{\rho} \frac{\partial \langle p \rangle}{\partial x} \quad (4.8)$$

$$\frac{d}{dy} \left(\nu \frac{d \langle u \rangle}{dy} - \tau_R \right) = \frac{1}{\rho} \frac{d \langle p_w \rangle}{dx} \quad (4.9)$$

where $\tau_R = \langle u'v' \rangle$ is the *Reynolds stress* due to fluctuations. Integrating the Equation (4.9) along y , and considering that $\tau_R(0) = \tau_R(2d) = 0$ and defining $\tau_W = [\mu \frac{d \langle u \rangle}{dy}]_0 = -[\mu \frac{d \langle u \rangle}{dy}]_{2d} > 0$ and $\tau(y) = \mu \frac{d \langle u \rangle}{dy}$ the final results is

$$\tau(y) = \tau_W + \tau_R(y) + \frac{1}{\rho} \frac{d \langle p_w \rangle}{dx} y \quad (4.10)$$

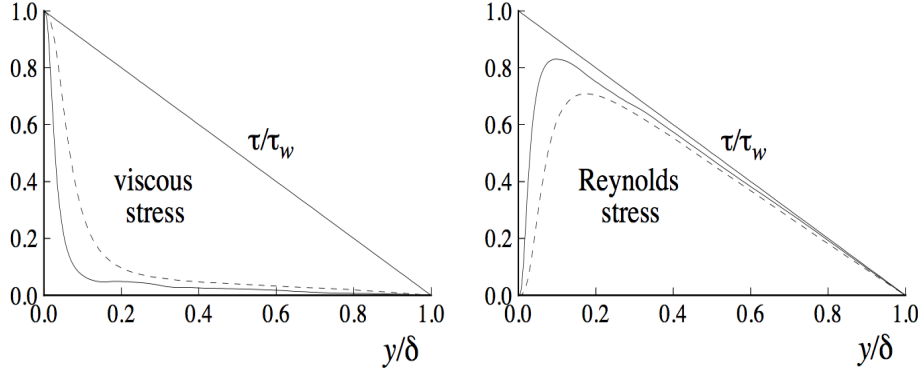


Figure 4.2: Profiles of the Viscous shear stress, and the Reynolds shear stress in turbulent channel flow: DNS data of Kim *et al.* [21]: dashed line, $Re = 5600$; solid line, $Re = 13750$.

It is clear that the total stress τ is given by two contributes: the *Reynolds stress* τ_R and the *Viscous stress* τ_W as shown in figure 4.2. In the middle of the channel $y = h$, for symmetries reasons $\tau(h) = 0$, so that in the top of channel at $y = 2h$

$$\tau_W = -\frac{h}{\rho} \frac{d \langle p_w \rangle}{dx} \quad (4.11)$$

The equation (4.9) is meaningful: the difference of pressure between inlet and outlet is balanced (reaching the equilibrium of the flow) by the wall shear-stress. Substituting the equation (4.11) into (4.10) one obtains

$$\tau(y) - \tau_R(y) = \tau_W \left(1 - \frac{y}{h} \right) \quad (4.12)$$

Therefore the problem can be reduced to determine the mean velocity profile along y direction which allows the evaluation of the characteristics of the channel flow.

4.1.2 Characteristic quantities

Close to the wall the viscosity ν and the wall shear stress τ_W are important parameters. From these quantities, *viscous scales* can be defined, that are appropriate velocity scales and lengthscales in the near-wall region. These are, respectively, the *friction velocity*, the *viscous lengthscale* and the *friction Reynolds number*

$$u_\tau \equiv \sqrt{\frac{\tau_W}{\rho}}, \quad \delta_\nu \equiv \nu \sqrt{\frac{\rho}{\tau_W}} = \frac{\nu}{u_\tau}, \quad Re_\tau \equiv \frac{u_\tau \delta}{\nu} = \frac{\delta}{\delta_\nu} \quad (4.13)$$

The distance from the wall is expressed in terms of *wall units*

$$y^+ \equiv \frac{y}{\delta_\nu} = \frac{u_\tau y}{\nu} \quad (4.14)$$

Notice that y^+ is similar to a local Reynolds number, so its magnitude can be expected to determine the relative importance of viscous and turbulent

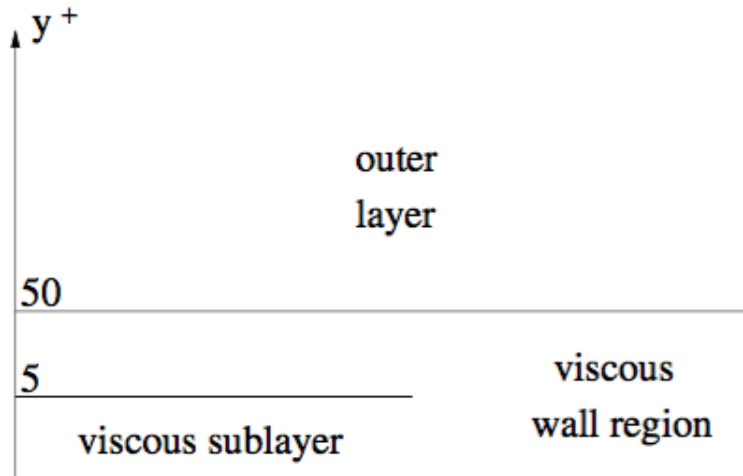


Figure 4.3: A sketch of different wall regions in terms of $y^+ = y/\delta_v$.

processes. Different regions or layers in the near wall flow are defined on the basis of y^+ as showed in figure 4.3. In the *viscous wall region* ($y^+ < 50$), there is a direct effect of the molecular viscosity on the shear stress; whereas, conversely, in the *outer layer* ($y^+ > 50$) the direct effect of viscosity is negligible. Within the viscous wall region, in the *viscous sublayer* ($y^+ < 5$), the Reynolds shear stress is negligible compared with the viscous stress. As the Reynolds number of the flow increases, the fraction of the channel occupied by the viscous wall region decreases, since δ_v/δ varies as Re_τ^{-1} .

4.1.3 Mean velocity profile

The mean velocity profile can be written in a non-dimensional form as $\langle u \rangle = u_\tau f(y/\delta, Re_\tau)$, and its derivative is

$$\frac{d\langle u \rangle}{dy} = \frac{u_\tau}{y} F\left(\frac{y}{\delta_v}, \frac{y}{\delta}\right) \quad (4.15)$$

where F is a non-dimensional function which depends on two non-dimensional parameters. The choice of the two parameters is that δ_v is the appropriate lengthscale in the viscous wall region ($y^+ < 50$) while δ is the appropriate scale in the outer layer ($y^+ > 50$). The relation $(y/\delta_\tau)/(y/\delta) = Re_\tau$ shows that these two parameters are not independent. The expression of the function F , depending on the region that one considers, has to be determined.

Prandtl (1925) postulated that, at high Reynolds number, close to the wall ($y/\delta \ll 1$) there is a *inner layer* in which the mean velocity profile is determined by the viscous scales, independent of δ and u_0 . This implies that one can write

$$\lim_{\frac{y}{\delta} \rightarrow 0} F\left(\frac{y}{\delta_v}, \frac{y}{\delta}\right) = F_1\left(\frac{y}{\delta_v}\right) \quad (4.16)$$

Taking into account this relation, the equation (4.15) can be rewritten in terms of $y^+ = y/\delta_v$ and $u^+ = \langle u \rangle / u_\tau$, so that

$$\frac{du^+}{dy^+} = \frac{1}{y^+} F_1(y^+) \quad (4.17)$$

The integral of (4.17) determines the *law of the wall*

$$u^+ = \int_0^{y^+} \frac{1}{y'} F_1(y') dy' = f_W(y^+) \quad (4.18)$$

There are a lot of experimental verifications which show that the f_W is universal for the Reynolds numbers not too close to transition. This trend is not only valid for channel flow, but also for pipe flow and boundary layers.

The viscous sublayer

It is said that the *law of the wall* is related to the *wall units* y^+ . The zone closer to the wall is the *viscous sublayer*.

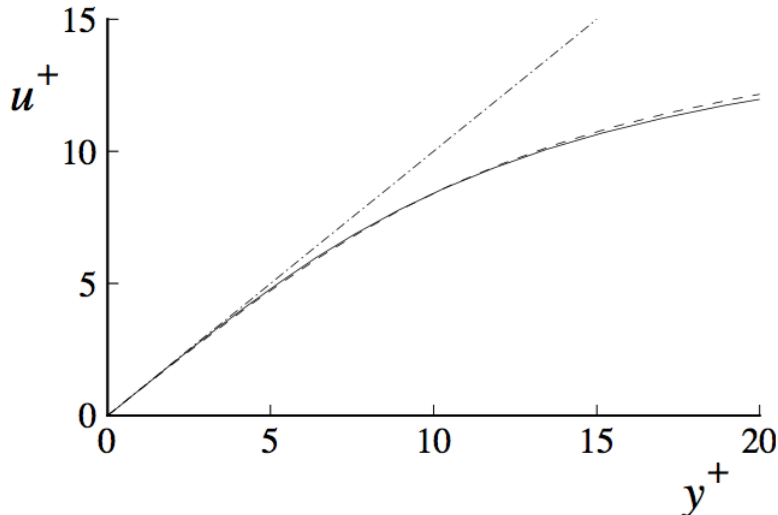


Figure 4.4: Near-wall profiles of mean velocity from the DNS data of Kim *et al.*[21]: dashed line, $Re = 5600$; solid line, $Re = 13750$; dot-dashed line, $u^+ = y^+$.

The law of this zone can be found from the equation (4.18) considering that the no-slip condition $\langle u \rangle_{y=0} = 0$ corresponds to $f_W(0) = 0$, while the viscous stress law at the wall yields for the derivative $f'_W(0) = 1$. Thus the Taylor-series expansion for $f_W(y^+)$ for small y^+ is

$$f_W(y^+) = y^+ + O(y^{+2}) \quad (4.19)$$

which express the linearity of the velocity profile in this zone. Figure 4.4 shows the profiles u^+ in the near wall region obtained from DNS. The gap from linear relation $u^+ = y^+$ is negligible in the viscous sublayer ($y^+ < 5$), but significant for $y^+ > 10$, showing that the profile changes with the region.

The logarithmic layer

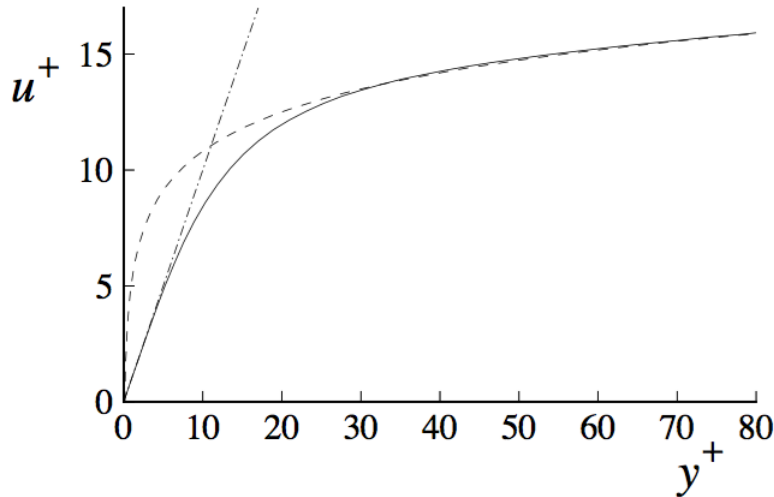


Figure 4.5: Near-wall profiles of mean velocity: solid line, DNS data of Kim *et al.* [21]; $Re = 13750$; dot-dashed line, u^+ ; dashed line, the log law.

The *inner layer* is usually defined as $y/\delta < 0.1$. For large y^+ it can be supposed that viscosity has little effect. Hence, in the equation (4.16), the dependence of $F_1(y^+)$ on ν vanishes, so that F_1 adopts a constant value denoted by k^{-1} , which is the *Von Karman constant*

$$F_1(y^+) = \frac{1}{k} \quad \text{for} \quad \frac{y}{\delta} \ll 1 \quad \text{and} \quad y^+ \gg 1 \quad (4.20)$$

Thus, in this region, the mean velocity gradient is

$$\frac{du^+}{dy^+} = \frac{1}{ky^+} \quad (4.21)$$

which integrated, leads to

$$u^+ = \frac{1}{k} \ln y^+ + B \quad (4.22)$$

where B is a constant. In literature, there is some variation in the values ascribed to the log-law constants, but generally they are within 5% of $k = 0.41$ and $B = 5.2$. Figure 4.5 shows a comparison between the log-law and DNS data in the inner part of the channel ($y/\delta < 0.25$). There is an excellent agreement for $y^+ > 30$. The region between the viscous sublayer ($y^+ < 5$) and the *log-law region* ($y^+ > 30$) is called the *buffer layer*. It represents the transition region between the viscosity-dominated and turbulence-dominated parts of the flow. The various regions and layers which are used to describe near-wall flows are summarized in figure 4.6.

4.2 PIPE FLOW

In a cylindrical pipe the constraint can be expressed as $0 < (y - R)^2 + z^2 < 1$, being involved two finite dimensions instead of one as in the channel. How-

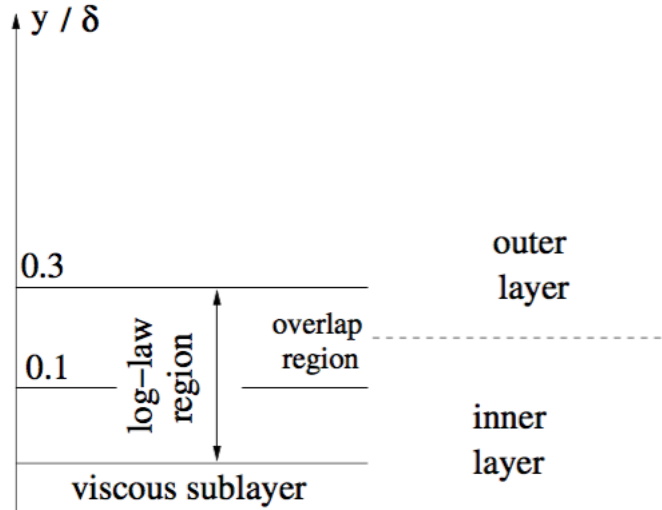


Figure 4.6: Trend of the velocity profile in the different regions of the channel

ever, moving to a cylindrical coordinates system (ϑ, r, z), the only non-periodic variable is r , whereas ϑ, z are periodic.

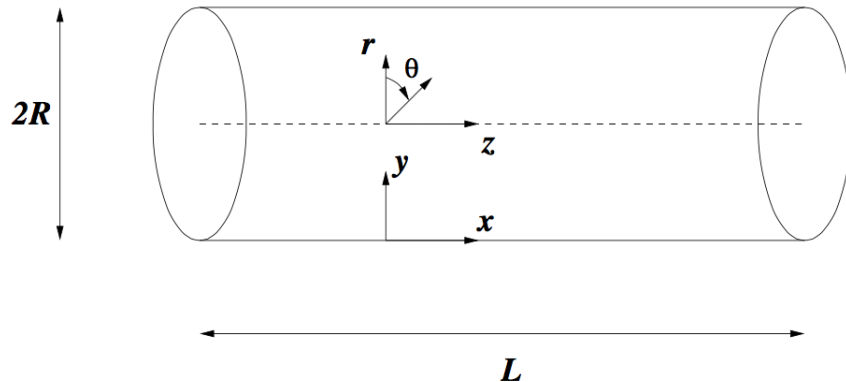


Figure 4.7: Scheme of a cylindrical pipe.

In figure 4.7 a fully developed turbulent flow in a long straight pipe of circular cross section with internal diameter $2R$ is shown. In polar cylindrical coordinates (ϑ, r, z) , velocity statistics depends solely on the radial coordinate, r . The mean centerline velocity is denoted by U_0 ,

$$U_0 \equiv \langle U(\vartheta, r, z) \rangle \quad (4.23)$$

and the bulk velocity is

$$U_b \equiv \frac{1}{\pi R^2} \int_0^R \langle U \rangle 2\pi r dr \quad (4.24)$$

Choosing $\delta \equiv R$ as characteristics flow width, the conventionally Reynolds number can be expressed as $Re = U_b 2R / \nu = U_b 2\delta / \nu$. The velocity profile is

different from the channel case, because the function $F(\frac{y}{\delta_v}; \frac{y}{\delta})$ depends on the constraint. However, $F_1(y^+)$ e $f_w(y^+)$ are similar to it because the *inner layer* is independent from the macroscopic characteristics; whereas in the *outer layer* the characteristics of the pipe influences the velocity profile, so one can focus the attention only in the near wall regions. For high Re numbers the log-law profile is similar to the channel one; for low Re numbers the *Von Karmann's* constant $1/k$ is higher and the value of A changes.

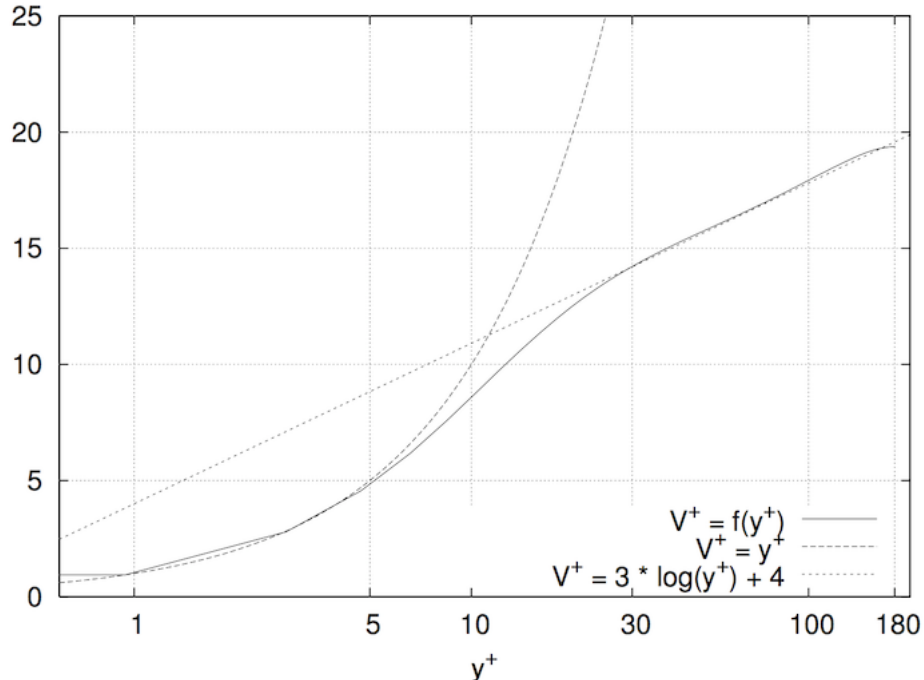


Figure 4.8: Velocity profile along z direction in terms of wall units y^+ performed by a DNS of pipe flow with $u_\tau = 6.82 \cdot 10^{-2}$, $Re_\tau = 180.72$ and $Re = 2650$.

As shown in figure 4.8, the velocity profile in the *inner layer* ($0 < y^+ < 5$) is the same of the channel and it follows the theory trend. In the *log layer* ($y^+ > 30$) the trend changes with a slope and constant equal to 3 and 4, respectively, rather than 1/0.41 and 5.2 as in the case of the channel.

In figure 4.9a the trend of Reynolds stresses τ_R and the wall stresses τ_w are shown, as a function of wall unit y^+ . As formulated by the theory, the Reynolds stresses at the wall are zero, whereas the wall stresses are maximum. When y^+ grows, τ_R has a relative maximum in the log layer, whereas the wall stresses tend to zero.

In the pipe flow (as seen in figure 4.8), the only mean velocity different from zero is along z . Its value along r is null because there is a constraint imposed at the wall, while along θ there is the hypothesis of zero tangential velocity. The reasoning changes for the second order velocity means which correspond to the fluctuations of the velocity field in the three directions as shown in figure 4.9b. Here the major contribute is given by $\langle u_z'^2 \rangle$; in addition the relative maxima of three curves are located in the *viscous wall region* and tend rapidly to zero at the wall.

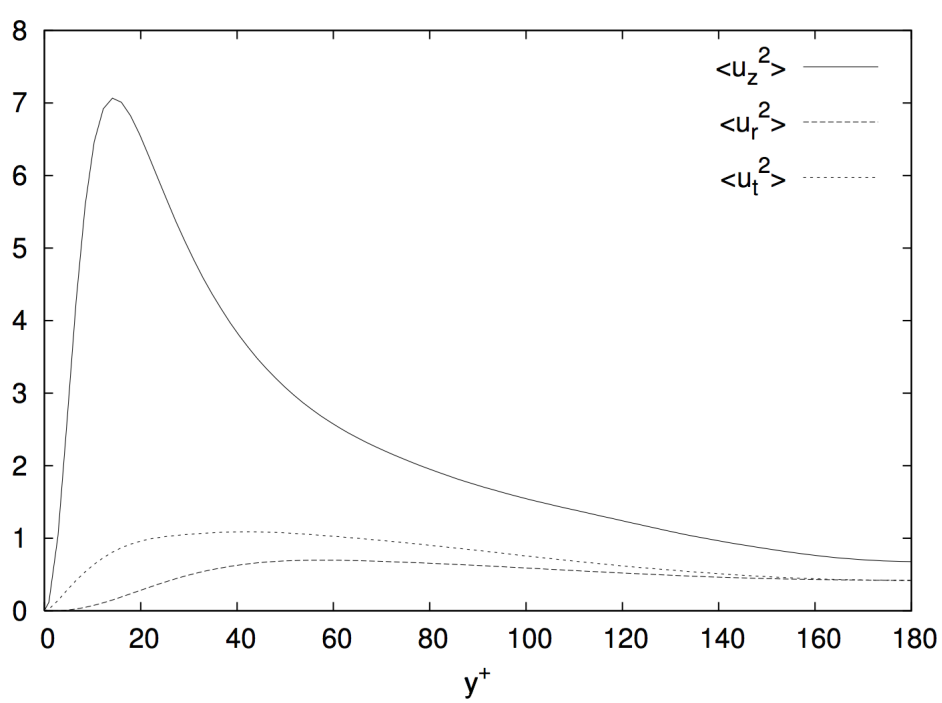
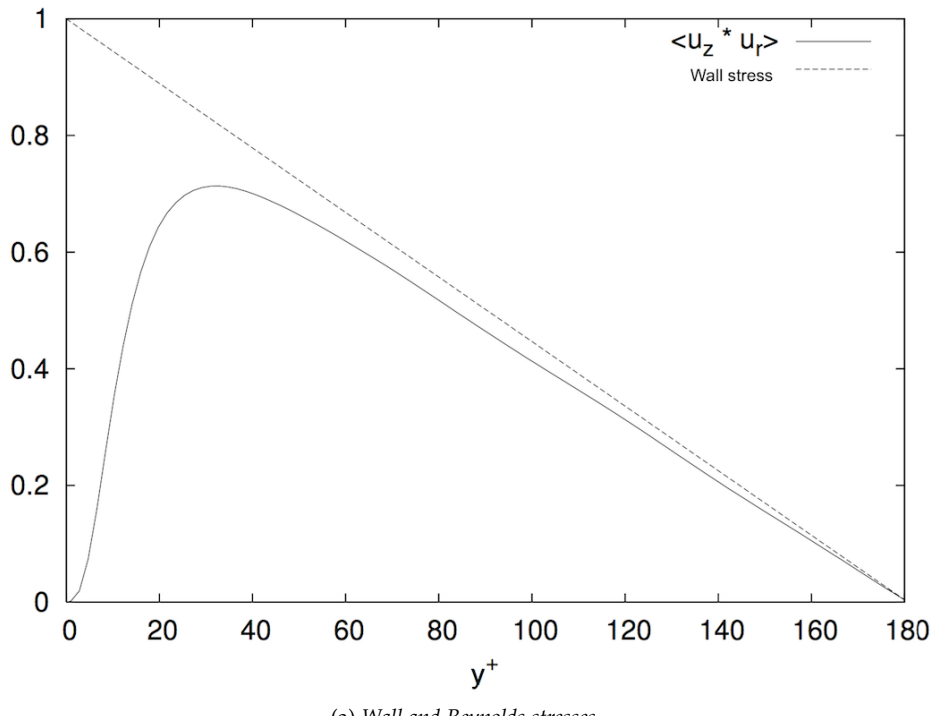


Figure 4.9: (a) Stresses and (b) Fluctuations velocity performed by a DNS of pipe flow with $u_\tau = 6.82 \cdot 10^{-2}$, $Re_\tau = 180.72$ and $Re = 2650$.

Part III
DIRECT NUMERICAL SIMULATION

5

NUMERICAL SIMULATIONS

This chapter contains the technique for numerical solution of the *Navier-Stokes equations* and the simulations carried out for the analysis of drag reduction in the turbulent pipe flow with a superhydrophobic surface.

5.1 EQUATIONS OF PIPE

The governing equations of the motion of an incompressible fluid flow are the *Navier-Stokes equations*, that expressed in cylindrical coordinates are respectively:

- *Continuity equation*

$$\frac{1}{r} \frac{\partial(ru_r)}{\partial r} + \frac{1}{r} \frac{\partial u_\theta}{\partial \theta} + \frac{\partial u_z}{\partial z} = 0 \quad (5.1)$$

- *Momentum equation*

$$\frac{\partial u_r}{\partial t} = h_r + b_r - \frac{1}{r} \frac{\partial p}{\partial r} + \frac{1}{Re} V_r^{\text{viscous}} \quad (5.2a)$$

$$\frac{\partial u_\theta}{\partial t} = h_\theta + b_\theta - \frac{1}{r} \frac{\partial p}{\partial \theta} + \frac{1}{Re} V_\theta^{\text{viscous}} \quad (5.2b)$$

$$\frac{\partial V_z}{\partial t} = h_z - \frac{1}{r} \frac{\partial p}{\partial z} + \frac{1}{Re} V_z^{\text{viscous}} \quad (5.2c)$$

Here the equations are non-dimensionalized by using the pipe radius R , the characteristic velocity U and the kinematic viscosity of the fluid ν . The *Reynolds number* is defined by

$$Re = \frac{UR}{\nu}$$

The characteristic velocity, U , can be defined using either the friction velocity, $u_\tau = \sqrt{\tau_w/\rho}$ and the bulk velocity, U_b . The choice depends on the flow condition, whether the mean pressure gradient, $-dP/dz$ or the mass flow rate is kept constant over the time of integration. The first terms, h_r , h_θ and h_z , on the right-hand side denote the non linear convective terms

$$h_r = -\frac{1}{r} \frac{\partial}{\partial r}(ru_r u_r) - \frac{1}{r} \frac{\partial}{\partial \theta}(u_\theta u_r) - \frac{\partial}{\partial z}(u_z u_r) \quad (5.3a)$$

$$h_\theta = -\frac{1}{r} \frac{\partial}{\partial r}(ru_r u_\theta) - \frac{1}{r} \frac{\partial}{\partial \theta}(u_\theta u_\theta) - \frac{\partial}{\partial z}(u_z u_\theta) \quad (5.3b)$$

$$h_z = -\frac{1}{r} \frac{\partial}{\partial r}(ru_r u_z) - \frac{1}{r} \frac{\partial}{\partial \theta}(u_\theta u_z) - \frac{\partial}{\partial z}(u_z u_z) \quad (5.3c)$$

The terms b_r and b_ϑ , in the equations of u_r , u_ϑ directions are the metrical terms arising from the curvature of coordinate system, respectively

$$b_r = \frac{u_\vartheta^2}{r} \quad (5.4a)$$

$$b_\vartheta = -\frac{u_r u_\vartheta}{r} \quad (5.4b)$$

whereas the viscous terms $V^{viscous}$ can be expressed as

$$V_r^{viscous} = \frac{1}{r} \frac{\partial r \tau_{rr}}{\partial r} + \frac{1}{r} \frac{\partial \tau_{r\vartheta}}{\partial \vartheta} - \frac{\tau_{\vartheta\vartheta}}{r} + \frac{\partial \tau_{zr}}{\partial z} \quad (5.5a)$$

$$V_\vartheta^{viscous} = \frac{1}{r} \frac{\partial r \tau_{\vartheta r}}{\partial r} + \frac{1}{r} \frac{\partial \tau_{\vartheta\vartheta}}{\partial \vartheta} + \frac{\tau_{r\vartheta}}{r} + \frac{\partial \tau_{z\vartheta}}{\partial z} \quad (5.5b)$$

$$V_z^{viscous} = \frac{1}{r} \frac{\partial r \tau_{zr}}{\partial r} + \frac{1}{r} \frac{\partial \tau_{z\vartheta}}{\partial \vartheta} + \frac{\partial \tau_{zz}}{\partial z} \quad (5.5c)$$

where τ_{ij} are the viscous stresses components, that in cylindrical coordinates can be written as

$$\tau_{rr} = 2\mu \left(\frac{\partial u_r}{\partial r} \right) \quad (5.6a)$$

$$\tau_{\vartheta\vartheta} = 2\mu \left(\frac{1}{r} \frac{\partial u_\vartheta}{\partial \vartheta} + \frac{u_r}{r} \right) \quad (5.6b)$$

$$\tau_{zz} = 2\mu \left(\frac{\partial u_z}{\partial z} \right) \quad (5.6c)$$

$$\tau_{r\vartheta} = \mu \left(\frac{\partial u_\vartheta}{\partial r} + \frac{1}{r} \frac{\partial u_r}{\partial \vartheta} - \frac{u_\vartheta}{r} \right) \quad (5.6d)$$

$$\tau_{zr} = \mu \left(\frac{\partial u_r}{\partial z} + \frac{\partial u_z}{\partial r} \right) \quad (5.6e)$$

$$\tau_{z\vartheta} = \mu \left(\frac{\partial u_\vartheta}{\partial z} + \frac{1}{r} \frac{\partial u_z}{\partial \vartheta} \right) \quad (5.6f)$$

Here the field is statistically homogeneous in z and ϑ directions so that several terms have zero mean value. The same thing can not be said for the single realization, thus these values have to be evaluated because they influence the evolution of solution.

5.2 CHORIN'S PROJECTION METHOD

A fractional step method formulated by Chorin [20] in 1968 has been used to solve numerically the incompressible *Navier-Stokes equations*. Chorin's method, approximates the evolution equations using a decomposition of the operators they contain. This method applied to the Navier-Stokes system, allows to overcome the problem of pressure, which is a Lagrangian constraint necessary to

force the solenoidality of velocity field, i.e. the conservation of mass. Considering the incompressible *Navier-Stokes equations*,

$$\frac{\partial \vec{u}}{\partial t} + \nabla \cdot (\vec{u} \otimes \vec{u}) = -\nabla p + \frac{1}{Re} \nabla^2 \vec{u} \quad (5.7)$$

$$\nabla \cdot \vec{u} = 0 \quad (5.8)$$

an intermediate velocity field \tilde{u} , which does not satisfy the mass conservation, is first computed. This explicitly implies the use of the momentum equation by ignoring the pressure gradient term

$$\frac{\partial \tilde{u}}{\partial t} = -\nabla \cdot (u \otimes u) + \frac{1}{Re} \nabla^2 \tilde{u} \quad (5.9)$$

This new intermediate velocity field \tilde{u} has to be projected for each time step as

$$u = \tilde{u} + \nabla \phi \quad (5.10)$$

where ϕ is a scalar variable which has to be determined. The first half of the algorithm focuses the attention on \tilde{u} , solving it through the equation (5.9); then in the second half, ϕ is evaluated. This brings to solve the *Poisson's problem* which is obtained replacing equation (5.10) into (5.8)

$$\nabla^2 \phi + \nabla \cdot \tilde{u} = 0 \quad (5.11)$$

After ϕ has been determined, one can return to the original problem, computing the general solution which is given by equation (5.10). There is a rigorous connection between the scalar term ϕ and the pressure term p , that can be found replacing the equation (5.10) into (5.7), obtaining

$$\frac{\partial}{\partial t}(\tilde{u} + \nabla \phi) + \nabla \cdot (u \otimes u) = -\nabla p + \frac{1}{Re} \nabla^2(\tilde{u} + \nabla \phi) \quad (5.12)$$

The equation (5.12) can be reduced simply considering (5.9), and getting to (5.13).

$$\frac{\partial}{\partial t}(\nabla \phi) + \nabla p - \frac{1}{Re} \nabla^2(\nabla \phi) = 0 \quad (5.13)$$

Taking out to common factor nabla in the equation (5.13) the result is

$$\nabla \left(\frac{\partial \phi}{\partial t} + p - \frac{1}{Re} \nabla^2 \phi \right) = 0 \quad (5.14)$$

Now integrating, the result in equation (5.16) is obtained.

$$\left(\frac{\partial \phi}{\partial t} + p - \frac{1}{Re} \nabla^2 \phi \right) = C(t) \quad (5.15)$$

$$\phi = \phi_0 - \int_0^t \left(p + \frac{1}{Re} \nabla \cdot \tilde{u} \right) dt \quad (5.16)$$

The equation (5.16) underlines the consistency of the algorithm and the relationship between the scalar variable ϕ and pressure term p . It gives also the correct boundary conditions that will be treated further in this chapter.

5.2.1 Solution of Poisson Equation

As pointed out in the previous section, one of the steps to solve equations (5.8) and (5.7), is to compute the Poisson's Equation (5.11). The solution of this type of equation, relies on the use of the *spectral method*. Recalling the Poisson's equation

$$\nabla^2 \phi = -\nabla \cdot \tilde{u} \quad (5.17)$$

and rewriting the Laplacian term in cylindrical coordinates, one obtains

$$\frac{1}{r} \frac{\partial}{\partial r} \left(r \frac{\partial \phi}{\partial r} \right) + \frac{1}{r^2} \frac{\partial^2 \phi}{\partial \vartheta^2} + \frac{\partial^2 \phi}{\partial z^2} = -\nabla \cdot \tilde{u} = f \quad (5.18)$$

Applying the *Fourier series expansion* to $\phi(r, \vartheta, z) = \hat{\phi}(r)_{k_\vartheta, k_z} e^{-jk_\vartheta \vartheta} e^{-jk_z z}$ and substituting it into (5.18)

$$\frac{1}{r} \frac{\partial}{\partial r} \left(r \frac{\partial \hat{\phi}}{\partial r} \right) - \frac{\hat{\phi}}{r^2} k_\vartheta^2 - \hat{\phi} k_z^2 = \hat{f} \quad (5.19)$$

$$\frac{1}{r} \frac{\partial}{\partial r} \left(r \frac{\partial \hat{\phi}}{\partial r} \right) - \left(\frac{k_\vartheta^2}{r^2} + k_z^2 \right) \hat{\phi} = \hat{f} \quad (5.20)$$

The equation (5.20) can be written as (see *Appendix B*)

$$\alpha \hat{\phi}_{i-1} + \beta \hat{\phi}_i + \gamma \hat{\phi}_{i+1} = \hat{f} \quad (5.21)$$

This last equation in matrix form is

$$A\phi = Q \quad (5.22)$$

where A is the square tridiagonal matrix, ϕ is a vector (or column matrix) containing the variable values at the grid nodes, and Q is the vector containing the terms on the right-hand side of equation (5.21). In general, this kind of mathematic problems are solved with the *Thomas algorithm* [11].

5.2.2 Staggered mesh

It is important to underline that it has been used to solve equations the second-order-accurate finite difference scheme [13] with staggered mesh [20]. As usual, vectors are defined on the cell surfaces and scalars are defined at the cell centre (figure 5.1). A practical and useful choice, is to assume the spacing to be equal in the θ and z directions and unequal in the r direction. With the staggered mesh, the momentum equations are evaluated at velocities nodes, and the continuity equation is enforced for each cell. One important advantage of using the staggered mesh for incompressible flows, is that ad hoc pressure boundary conditions are not required.

5.3 TIME INTERPOLATION

The temporal discretization of the equations is based on the explicit *Runge-Kutta method* [16] with an accuracy of third order. This method, belongs to the

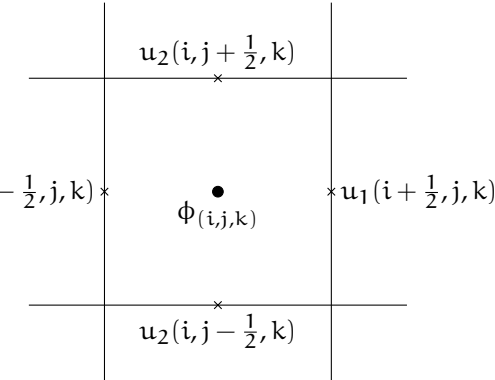


Figure 5.1: The staggered mesh in two dimensions.

group of *Low storage Runge-Kutta method* [39], where the storage quantities for each time step depend only from the previous time step solution. A generic time evolution equation $du/dt = RHS[u]$ is considered, where u is a generic quantities and RHS is the operator which represents the right-hand side of the equation. Therefore the temporal evolution scheme can be written as

$$\begin{cases} u_1 = u^n + \alpha_1 RHS[u^n] \\ u_2 = u_1 + \Delta t (\alpha_2 RHS[u_1] + \beta_2 RHS[u_2]) \\ u_3 = u_2 + \Delta t (\alpha_3 RHS[u_2] + \beta_3 RHS[u_3]) \\ u^{n+1} = u_3 \end{cases} \quad (5.23)$$

where the subscript index specifies the substeps, whereas the top index specifies the time step. The value of coefficients which have been used in the numerical code are shown in the following table.

Index	1	2	3
α_i	$8/15$	$5/12$	$3/4$
β_i	0	$-17/60$	$-5/12$

Table 1: Values of *Low storage Runge-Kutta* coefficients.

5.4 BOUNDARIES CONDITIONS

The boundaries conditions concern the periodicity, the impermeability and the presence of slip or no-slip conditions at the wall. The periodicities are imposed, for the geometry of the pipe, along z and θ directions. The impermeability is forced on the external face of the entire pipe $u_r = 0$ in the direction of the wall. Now the slip or no-slip boundaries conditions distinguish the simulation of superhydrophobic from a smooth surface. As mentioned in chapter 2, the superhydrophobic surfaces are represented by an alternate pattern of *grooves* and *peaks* (wall) as shown in figure 5.2, where the groove is filled by air and

not water. To model a superhydrophobic surface, it is necessary to distinguish two zones, with different interfaces: one is characterised by an interface liquid-gas linked to the groove and the other has an interface liquid-solid linked to peak. To simulate the latter is sufficient to impose the a no-slip condition; whereas the problem of how to model the liquid-gas interface remains. As still explained in chapter two in the Navier's model, the magnitude of the slip velocity, U_s , is proportional to the magnitude of the shear rate experienced by the fluid at the wall:

$$U_s = b \left| \frac{\partial \langle u \rangle}{\partial r} \right| \quad (5.24)$$

where b is the slip length. Starting from this hypothesis, the simulation has considered that b is ∞ so that $\frac{\partial \langle u \rangle}{\partial r} = 0$. In this way it is not necessary to impose a specific slip velocity, which would not correspond to the reality. In the simulations, the interface liquid-gas has been considered flat with no normal shear stress, i.e. the interface does not oscillate. The assignment of zero shear stress is a good approximation, considering that the shear stress is

$$\tau_{ij} = 2\mu E_{ij} \quad (5.25)$$

Note that the dynamic viscosity μ of the air is fifty times smaller than the water: therefore it validates the approximation. In the hypothesis of flat liquid-gas interface, the whole pipe surface is placed at a radial quote coincident to the peaks. A no-slip boundary condition is imposed for peaks $u_\theta = 0$ and $u_z = 0$ and for grooves, where the fluid slides on the air layer, the slip boundary condition is $\frac{\partial u_z}{\partial r} = 0$ and $\frac{\partial u_\theta}{\partial r} = 0$.

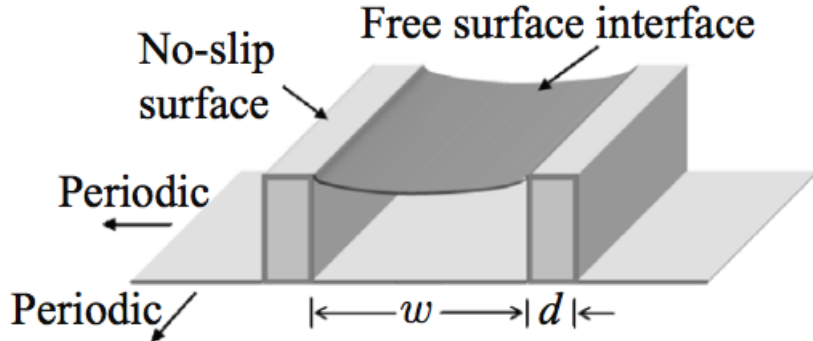


Figure 5.2: Scheme of superhydrophobic surface with two different interfaces.

The boundary conditions (B.C) are set to the u , and they have to be projected in parallel τ and normal n directions to the surface, considering also the decomposition made in the equation (5.10). The impermeability B.C is related to n and is valid for both interfaces (liquid/gas and liquid/solid), and it can be written as

$$u \cdot n = \tilde{u} \cdot n + \frac{\partial \phi}{\partial n} = 0 \quad \begin{cases} \tilde{u} \cdot n = 0, & \text{Unprojected variable.} \\ \frac{\partial \phi}{\partial n} = 0, & \text{Poisson's equation.} \end{cases}$$

The no-slip B.C (τ direction) referred to the peaks (interface liquid-solid) is

$$u \cdot \tau = \tilde{u} \cdot \tau + \frac{\partial \phi}{\partial \tau} = 0 \quad \begin{cases} \tilde{u} \cdot \tau = 0, & \text{Unprojected variable.} \\ \frac{\partial \phi}{\partial \tau} = 0, & \text{Poisson's equation.} \end{cases}$$

The slip B.C for the interface liquid-gas (groove) is

$$u \cdot \tau = \tilde{u} \cdot \tau + \frac{\partial \phi}{\partial \tau} \quad \begin{cases} \tilde{u} \cdot \tau = \min, & \text{Projection variable.} \\ \frac{\partial \phi}{\partial \tau} = \min, & \text{Poisson's equation.} \end{cases}$$

It must be underlined that there are not information about the value of $\frac{\partial \phi}{\partial \tau}$. For numerical reasons, it is proved, that the deviation from the value would be slight and it satisfies the relation $u \cdot \tau = \tilde{u} \cdot \tau$.

In addition to the simulations done with an interface liquid-vapour flat, previously discussed, a *movable interface* liquid-gas has been preliminary studied. In this case it can move with its own velocity, so that the pressure field have an influence on the shape of the interface. The correct boundary condition is directly set on ϕ , which is related to the pressure field, as shown in equation (5.16). This, in terms of boundaries conditions, means that $u \cdot n \neq 0$, so that the interface has a normal velocity expressed as

$$u \cdot n = \tilde{u} \cdot n + \frac{\partial \phi}{\partial n} \quad \begin{cases} \tilde{u} \cdot n, & \text{Projection variable.} \\ \phi = \phi_0 - \int_0^t (p + \frac{1}{Re} \nabla \cdot \tilde{u}) dt, & \text{Poisson's equation.} \end{cases}$$

Table 2 summarizes the different boundaries conditions for the several cases which have been taken into account

Interface	Type	Direction	Eq. Poisson
No	Peak	$u \cdot n$	$\frac{\partial \phi}{\partial n} = 0$
		$u \cdot \tau$	$\frac{\partial \phi}{\partial \tau} = 0$
	Groove	/	/
		/	/
Flat	Peak	$u \cdot n$	$\frac{\partial \phi}{\partial n} = 0$
		$u \cdot \tau$	$\frac{\partial \phi}{\partial \tau} = 0$
	Groove	$u \cdot n$	$\frac{\partial \phi}{\partial n} = 0$
		$u \cdot \tau$	$\frac{\partial \phi}{\partial \tau} = \min$
Movable	Peak	$u \cdot n$	$\frac{\partial \phi}{\partial n} = 0$
		$u \cdot \tau$	$\frac{\partial \phi}{\partial \tau} = \min$
	Groove	$u \cdot n$	$\phi = \phi_0 - \int_0^t (p + \frac{1}{Re} \nabla \cdot \tilde{u}) dt$
		$u \cdot \tau$	$\frac{\partial \phi}{\partial \tau} = \min$

Table 2: Description of boundaries conditions for different cases.

5.5 CHARACTERISTIC PARAMETERS

The numerical code solves the non dimensional form of the Navier-Stokes system with characteristics parameters $\tilde{R} = 1$, $\tilde{U}_b = 1$ and $\tilde{\nu} = 1$ so $Re_{AD} = \tilde{U}_b \tilde{R}/\tilde{\nu} = 1$. Furthermore the reference velocity is U_R , imposing $\tilde{U}_b = U_b/U_R = 1$ so that $U_b = U_R$. To make the simulation comparable the forcing term f_g into Navier-Stokes equation, which is a constant pressure gradient expressed in non-dimensional unities $(dp/dz)/(\rho U^2)$ equal to $7.88 \cdot 10^{-3}$ for the reference simulation, has been imposed the same value for all simulations. The simulations differ from $Re_N = U_b R/\nu$ which depends on U_b . Now the $Re_{eff} = Re_N Re_{AD}$ depends only from U_b , with a fixed value of $Re_N = 5000$. All simulations have been adimensionalised with U_τ so $Re_\tau = U_\tau R/\nu = \sqrt{\tau_w/\rho R/\nu}$. This in the practical computation means to multiply for $1/U_b \cdot Re_N/Re_\tau$. Reporting the parameters to a real case where the pipe has a fixed radius of 1mm, so the *reference simulation* has a bulk velocity of $U_b = 5\text{m/s}$, having considered for the water $\nu = 10\text{m}^2/\text{s}$. The pipe has two periodicity: along the tangential coordinate ϑ and the longitudinal coordinate z ; the last one needs to simulate a pipe of infinite length. The spatial coordinates of the pipe move along the interval:

$$0 \leq \vartheta \leq 2\pi, \quad 0 \leq r \leq R, \quad 0 \leq z \leq Z_{max}$$

The value of $Z_{max} = 2\pi R$, evaluated from others experiences, ensures that the correlation along z goes to zero. Since the boundary conditions change respect to standard cases, it is necessary to verify, at the end of simulations, that the far end points of the domain are not correlated.

5.5.1 Calculus domain

The domain is divided in three directions $[\theta \times r \times z]$ with $[384 \times 129 \times 256]$ points. The number of grid points is chosen to solve the viscous scale and also the Kolmogorov's scale. This scale is defined as

$$\eta = \left(\frac{\nu^3}{\epsilon} \right)^{\frac{1}{4}} \quad (5.26)$$

where ϵ is the turbulent dissipation for mass unit. In a pipe with circular section [31], η can be expressed as

$$\eta = \frac{1.5}{Re_\tau} R \quad (5.27)$$

Considering a cylindric pipe with $Re_N = 5000$ and $Re_\tau = U_\tau R/\nu = 308$ with $U_\tau = (\tau_w/\rho)^{1/2}$, therefore $\eta = 5 \cdot 10^{-3}$ so this ensures that the amplitude of the grid $[\Delta\theta \times \Delta r \times \Delta z] = [0.0163 \times 0.00226 \div 0.00954 \times 0.0245]$ is of the same order of Kolmogorov's scale.

5.6 SIMULATIONS

The cases studied present the pattern of the grooves sorted in the streamwise direction. As still observed in chapter two there are several study on the super-hydrophobic surfaces applied to the channel flow, where the drag reduction

is explored. In this thesis the simulations performed differs for the width of groove and peak. The width is expressed in terms of cells occupied by the grooves (slip) and peaks (no-slip) in azimuthal direction ϑ (composed by 384 cells). The various simulations consider a different number of cells along ϑ , where a slip or no-slip boundary condition is imposed. This implies a variation of the solid fraction ϕ_s , which is defined as the portion of surface occupies by a no-slip condition with respect to the total number of cells. In table 3 the set of simulated configurations with superhydrophobic surface is listed.

Name	Nº of cells	ϕ_s	Wall unit	Physic unit [μm]
Smooth	0-384	100%	0- 2π	0-628
SHS 4-4	4-4	50%	20.34-20.34	65.4-65.4
SHS 6-2	6-2	25%	30.52-10.17	98.1-32.7
SHS 2-6	2-6	75%	10.17-30.52	32.7-98.1
SHS 8-8	8-8	50%	40.69-40.69	130.8-130.8
SHS 12-4	12-4	25%	61.04-20.34	196.2-65.4
SHS 4-12	4-12	75%	20.34-61.04	65.4-196.2

Table 3: All simulations performed with *superhydrophobic surface* SHS with flat interface. The Nº of cells indicate the presence of x cells slip and y no slip. This pattern are replaced along the entire circumference. The solid fraction ϕ_s is evaluated as $y/(x + y)$ and expresses the percentage of the slip zone along θ . The dimensions of pattern are expressed also in terms of wall unit and physic unit [μm], the latter evaluated supposing a radius pipe of $R = 1\text{mm}$.

6

RESULTS

In this chapter the results obtained from simulations will be discussed. In particular, it will be shown the mean velocities profiles, in one and two dimensions, in order to have an estimation of the drag reduction within the pipe. Furthermore, the momentum balance [12] has been used to analyse the different dynamic contributions which cause the drag reduction. Finally, the trend of the mean pressure of the six cases and the pressure fluctuations are reported. The latter are used to build the probability density functions to evaluate the maxima of pressure fluctuations at the interface liquid-gas that are relevant to study the stability of the Cassie Baxter state [6].

6.1 MEAN VELOCITIES

To obtain the mean velocities, the averages are performed in space along ϑ , z and in time. For one dimensional velocity averages, the dependence is removed from z , taking advantage of the periodicity of the pipe. Average in phase, along ϑ , takes into account separately the slip and no-slip cells. Once two cloves are obtained, the first related to slip (grooves) and the second to the no-slip zones (peaks), they are repeated periodically for reconstructing the pipe section which depends on r and z . In this way the average is performed only between cells of the same nature. In more detail, considering the period nature of grooves in the spanwise direction, a phase-averaging operator is introduced (as suggested by Reynolds and Hussain [33]):

$$\langle u(\varphi, r) \rangle = \frac{1}{N} \sum_{n=1}^N \iint_{t,z} u\left(L\left(\frac{\varphi}{2\pi} + n\right), r, z, t\right) dz dt \quad (6.1)$$

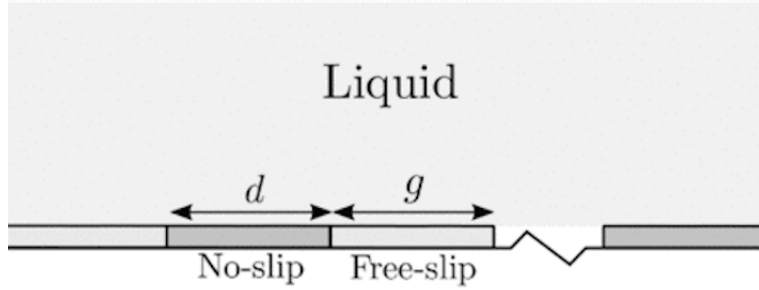
where u is an the velocity field as a function of space and time, ϕ is a phase with respect to the periodic structure, N is a number of periods in the computational domain. Now averaging $\langle u \rangle$ over ϕ results in spatial mean

$$\bar{u}(r) = \frac{1}{2\pi} \int_0^{2\pi} \langle u(\varphi, r) \rangle d\varphi \quad (6.2)$$

The fluctuations can be computed defining also the overall fluctuation as the deviation of from the spatial mean

$$u'(\vartheta, r, z, t) = u(\vartheta, r, z, t) + u'(r). \quad (6.3)$$

For all simulations the pressure gradient is constant ($7.88 \cdot 10^{-3}$), and the number of Reynolds stress $Re_\tau = 311.35$ is considered the same. The values of Re_τ of the simulations are not close to this value and the deviations from this value is less then 1% as showed table 4.

Figure 6.1: Sketch of the model of SHS surface with $L=d+g$.

Case	Smooth	4-4	6-2	2-6	8-8	12-4	4-12
Re_τ	313.82	310.71	308.93	312.01	311.78	311.31	310.90
Deviation	0.79%	0.21%	0.77%	0.21%	0.01%	0.01%	0.14%

Table 4: Values of Re_τ and the deviation from the mean value.

6.1.1 Longitudinal velocity

The contribution of superhydrophobic surface to the increase of drag reduction, is observable through global parameters, showed in table 5: U_b (mean velocity over the section), U_s (velocity at the liquid-gas interface) and their difference. As one can notice, the slip velocity U_s increases with the width of grooves, except for the case SHS 6-2 where the velocity is higher than SHS 8-8 (where grooves have a wide greater than 6-2).

Name	U_b	U_s	$U_b - U_s$	$(U_b - U_s)^+$
Smooth	1	0	1	16.05
SHS 4-4	1.15	0.2834	0.8666	13.93
SHS 6-2	1.45	0.6943	0.7557	12.15
SHS 2-6	1.07	0.0826	0.9874	15.87
SHS 8-8	1.22	0.4048	0.8152	13.11
SHS 12-4	1.62	0.9370	0.6831	10.98
SHS 4-12	1.06	0.1263	0.9337	15.01

Table 5: Values of U_b , U_s and their difference also in terms of wall units $+$, having adimensionalized with u_τ where the characteristics parameters are $Re_N = 5000$ and $Re_\tau = 311.35$.

In figure 6.2a the mean longitudinal velocity profiles $\langle u_z \rangle^+$ are represented. Making a comparison between simulations, the velocity is higher for the su-

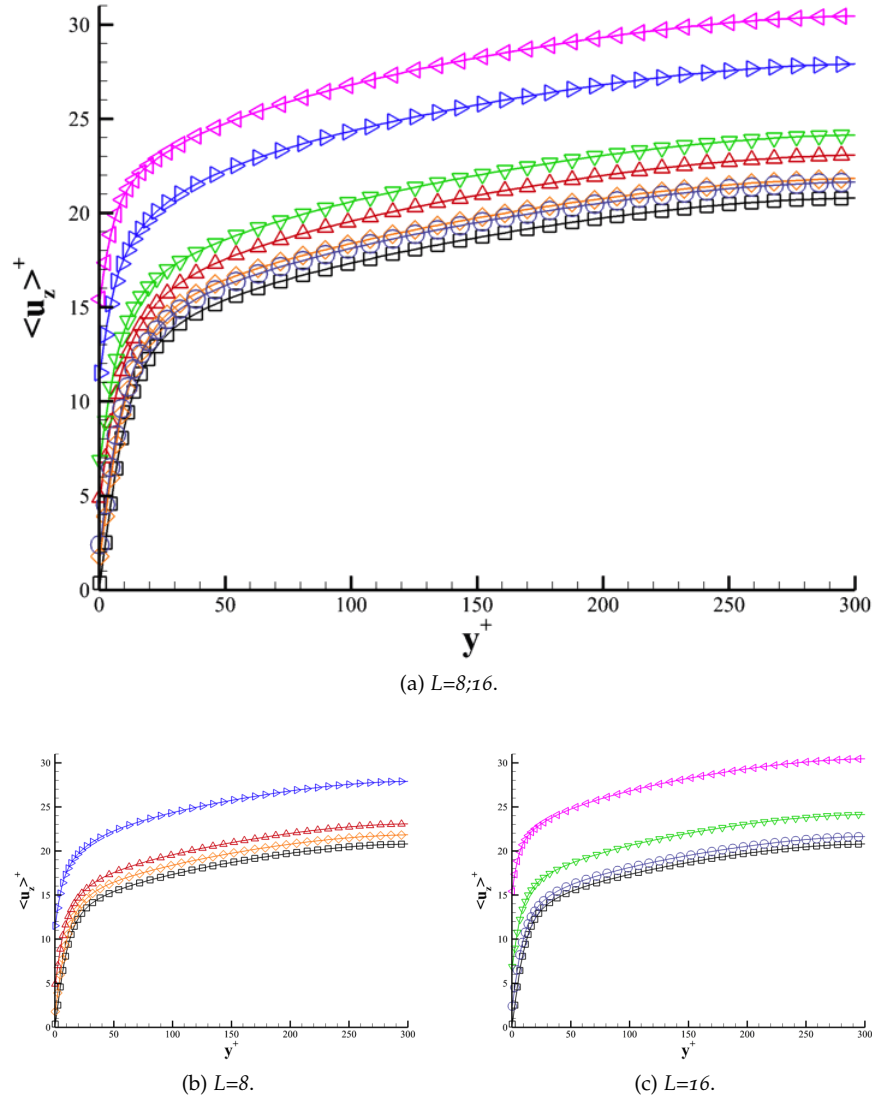


Figure 6.2: **(a)** Means velocity profiles of $\langle u_z \rangle^+$ as a function of the distance from the wall y^+ . The symbol + indicates the variables express in terms of wall units, with characteristics parameters $Re_N = 5000$ and $Re_\tau = 311.35$. The simulation performed are: smooth surface (black line \square); SHS with 4 slip-4 no-slip cells (red line \triangle); SHS with 8 slip-8 no-slip cells (green line \triangledown); SHS with 6 slip-2 no-slip cells (blue line \triangleright); SHS with 12 slip-4 no-slip cells (pink line \triangleleft); SHS with 2 slip-6 no-slip cells (orange line \diamond); SHS with 4 slip-12 no-slip cells (dark blue line \circlearrowright). Plot **(a)** has been splitted for the number of cells: in **(b)** $L=8$ and **(c)** $L=16$.

perhydrophobic cases in comparison to smooth surface. In addition, the simulations SHS 2-6 and SHS 4-12 exhibit a velocity profile which is very close to the reference case. The reason of this behaviour lies on the width of slip cells which have a solid fraction $\phi_s = 75\%$.

For the opposite reason, the cases SHS 6-2 and SHS 12-4 with $\phi_s = 25\%$, show higher velocity profiles. Having fixed the width of pattern L, the mean velocity profiles $\langle u_z \rangle^+$, as pointed out in figures 6.2b and 6.2c, exhibit an increment of velocity with the growth of the width of the grooves.

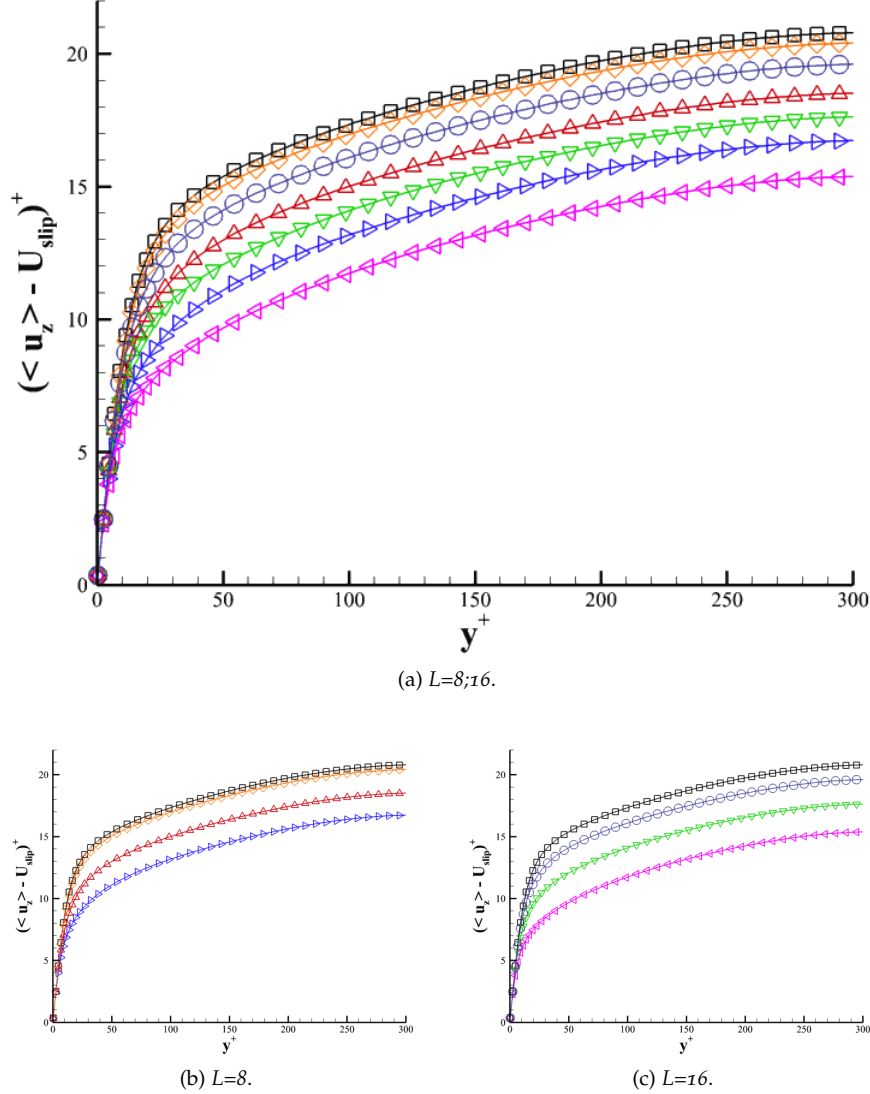


Figure 6.3: (a) Means velocity profiles $(\langle u_z \rangle - U_s)^+$ as a function of the distance from the wall y^+ . The symbol + indicates the variables express in terms of wall units, having adimensionalized with u_τ where the characteristics parameters are $Re_N = 5000$ and $Re_\tau = 311.35$. The simulation performed are: smooth surface (black line \square); SHS with 4 slip-4 no-slip cells (red line \triangle); SHS with 8 slip-8 no-slip cells (green line \triangledown); SHS with 6 slip-2 no-slip cells (blue line \triangleright); SHS with 12 slip-4 no-slip cells (pink line \triangleleft); SHS with 2 slip-6 no-slip cells (orange line \diamond); SHS with 4 slip-12 no-slip cells (dark blue line \circ). Plot (a) has been splitted for the number of cells: in (b) $L=8$ and (c) $L=16$.

In this study, the pressure gradient and the section of the pipe has been kept constant. Thus, observing the figures 6.2a and 6.3a, one can start to think in terms of mass flow rate to analyse the drag reduction within the superhydrophobic pipe. In first approximation, let's assume that the variation of the total mass flow rate ΔQ^{TOT} is given by two different contributes:

- ΔQ_S : variation of the mass flow rate produced by the slip velocity U_s
- ΔQ_T : variation of the mass flow rate produced by the turbulence structure

These terms are related to the figures 6.2a and 6.3a. As specified in detail in the figures 6.3b and 6.3c, the gap from the smooth case is much emphasised in the case of $L=16$ rather than $L=8$. Now comparing the figures 6.2a and 6.3a one notices that: in the first one, all mean velocities with superhydrophobic surface are located above the smooth case, whereas in the second the trend is opposite. The figure 6.2a expresses the contribution given by ΔQ^{TOT} and figure 6.3a that of ΔQ_T . The last one is originated by the modification of turbulent structures and tends to decrease the mass flow rate, i.e. the drag reduction. The remaining contribution ΔQ_S , related to the slip velocity, produces an increase of the mass flow rate, i.e. drag reduction within the pipe. However, the positive effect of ΔQ_S prevails on ΔQ_T producing a positive variation of total mass flow rate ΔQ^{TOT} . It is important to underline that this is true only in first approximation because the phenomenon is not linear and the two effects are coupled.

The mean velocity profiles along z , are reported in figure 6.4 as a function of y^+ in semi-logarithmic scale [18]. It is possible to observe for the reference case the same trend known in literature: the first zone, the viscous sublayer, shows a linear profile which arrives up to $y^+ \approx 5$; a buffer layer between $5 < y^+ < 30$ and then a logarithmic region for $y^+ > 30$. In table 6 the constant values of the equation (6.4) are reported: they are coherent with the values available in literature, $k = 0.43$ and $B = 6.13$ (Pope [31]).

$$U^+ = \frac{1}{k} \ln y^+ + B. \quad (6.4)$$

Case	Smooth	4-4	6-2	2-6	8-8	12-4	4-12
k	0.3461	0.3439	0.3386	0.3451	0.3336	0.3339	0.3408
B	4.2134	2.0519	0.1732	3.9231	0.6063	-1.6305	3.0326

Table 6: Different values of the parameters k and B of the equation (6.4) for all simulations performed.

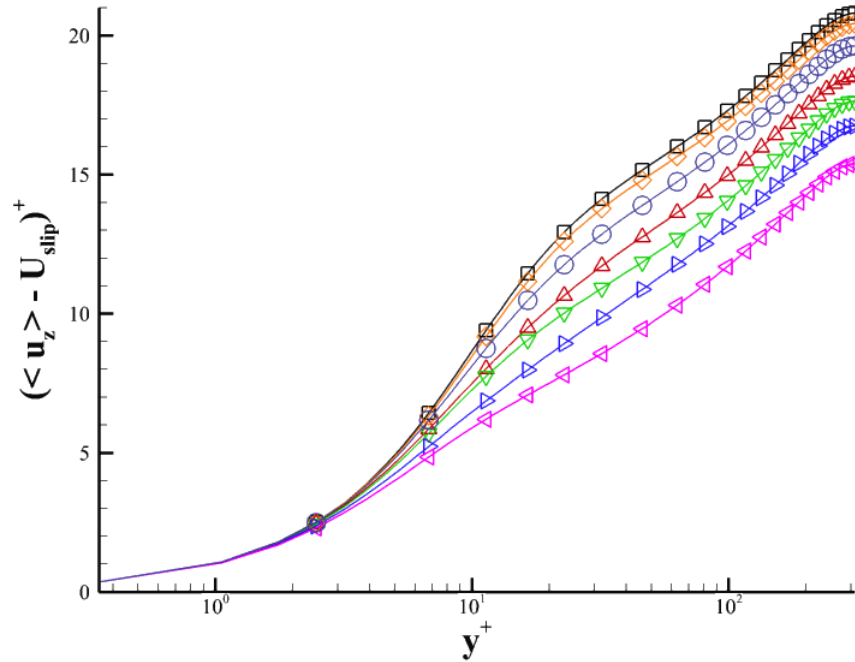


Figure 6.4: The distance from the wall y^+ in logarithmic scale as a function of means velocity profiles $(\langle u_z \rangle - U_s)^+$. The symbol + indicates the variables express in terms of wall units, having adimensionalized with u_τ where the characteristics parameters are $Re_N = 5000$ and $Re_\tau = 311.35$. The simulation performed are: smooth surface (black line \square); SHS with 4 slip-4 no-slip cells (red line \triangle); SHS with 8 slip-8 no-slip cells (green line \triangledown); SHS with 6 slip-2 no-slip cells (blue line \triangleright); SHS with 12 slip-4 no-slip cells (pink line \lhd); SHS with 2 slip-6 no-slip cells (orange line \diamond); SHS with 4 slip-12 no-slip cells (dark blue line \circlearrowleft).

6.1.2 Radial velocity

In figure 6.5, the two-dimensional mean radial velocities for the simulations are shown. They have been obtained using an average in phase. All simulations, excepted for the smooth case, have the same behaviour: the radial velocity $\langle u_r \rangle|_g$ (average in phase) is positive at the grooves (slip condition) and it is negative at peaks (no-slip condition). This means that in the first case the flux tends to approach to the interface, whereas in the second it tends to move away from the wall. Furthermore, as the width of groove increases, the mean radial velocity increases too. Comparing the two extreme cases, the behaviour previously explained is particularly evident. For the case of figure 6.5c, referred to the case SHS 2-6, one notices that the values maxima and minima of radial velocity are an order of magnitude lower than the case SHS 12-4. The alternate trend of positive and negative velocity induces the formation of *vortical structures* $\langle \omega_z \rangle|_g$ near the surface [28], as shown in figure 6.7. In this figure the velocity vectors indicate the rotating verse of vortical structures [17].

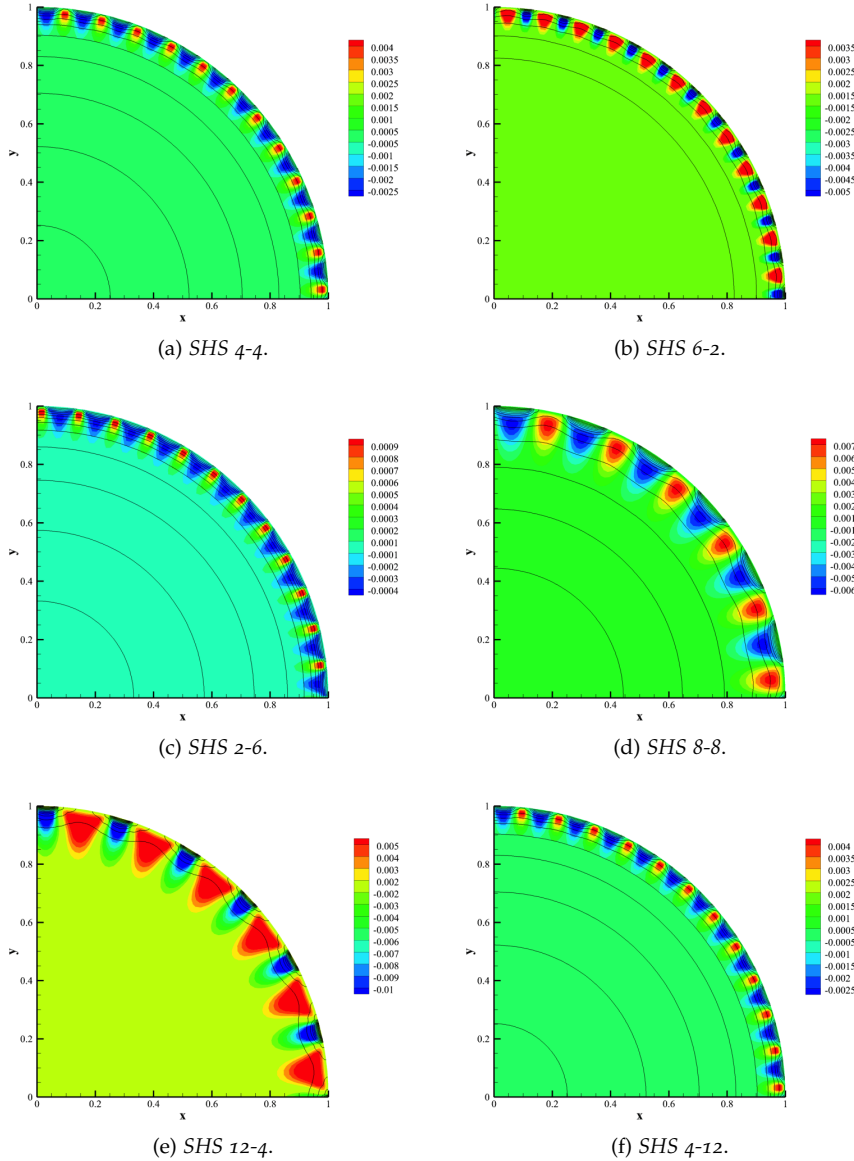


Figure 6.5: Two dimensional mean radial velocity $\langle u_r \rangle |_\vartheta$ (flood colours) and the longitudinal mean velocity $\langle u_z \rangle$ to represent the portion of the solid boundary (black isoline). Different shades in the background are originated due to the different interval used to plot them.

These tend to place themselves outwardly to the peaks, remaining symmetric in their middle. This behaviour can be explained by the presence of different velocities between slip and no-slip zone and it is also confirmed by the fact that the pressure inside the groove is negative and this tends to attract to itself the vortical structures. These structures become more intense when the width of peaks is reduced and tend to move away from the centre of the peak as the width of groove decreases. As showed in figure 6.8, these vortical structures are symmetric to the centre of the peaks.

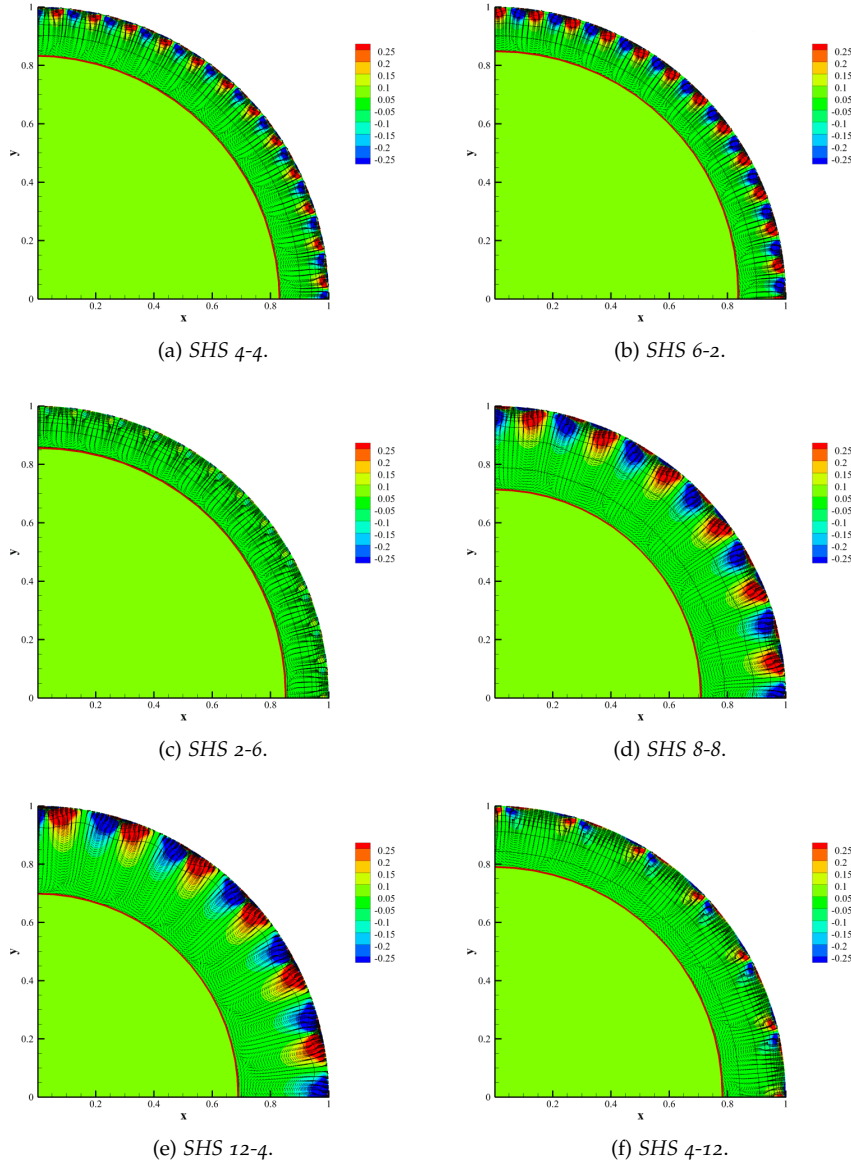


Figure 6.6: Two dimensional mean vorticity along z direction $\langle \omega_z \rangle|_{\partial}$ in correspondence of grooves and peaks (flood colours); representation of $\langle u_x \rangle|_{\partial}$, $\langle u_y \rangle|_{\partial}$ (black vectors); whereas the longitudinal mean velocity $\langle u_z \rangle|_{\partial}$ to represent the portion of the solid boundary (black isoline). The red line indicates the limit of the extension of vortical structures. The interval of values is fixed for all simulations.

Moreover there are additional vortical structures, named *secondary vortexes*, that are located above the primary one. These secondary structures turn in opposite direction to the primary and are also less strong. Their appearance originate due to the dragging of the flow by the principal vortexes. The figure 6.6 underlines the fact that these vortical structures, increasing the width of grooves, tend to enhance their extension within the pipe. The mostly significa-

tive case is that of SHS 12-4 where the vortical structures are extended up to the 32% of the radius of the pipe.

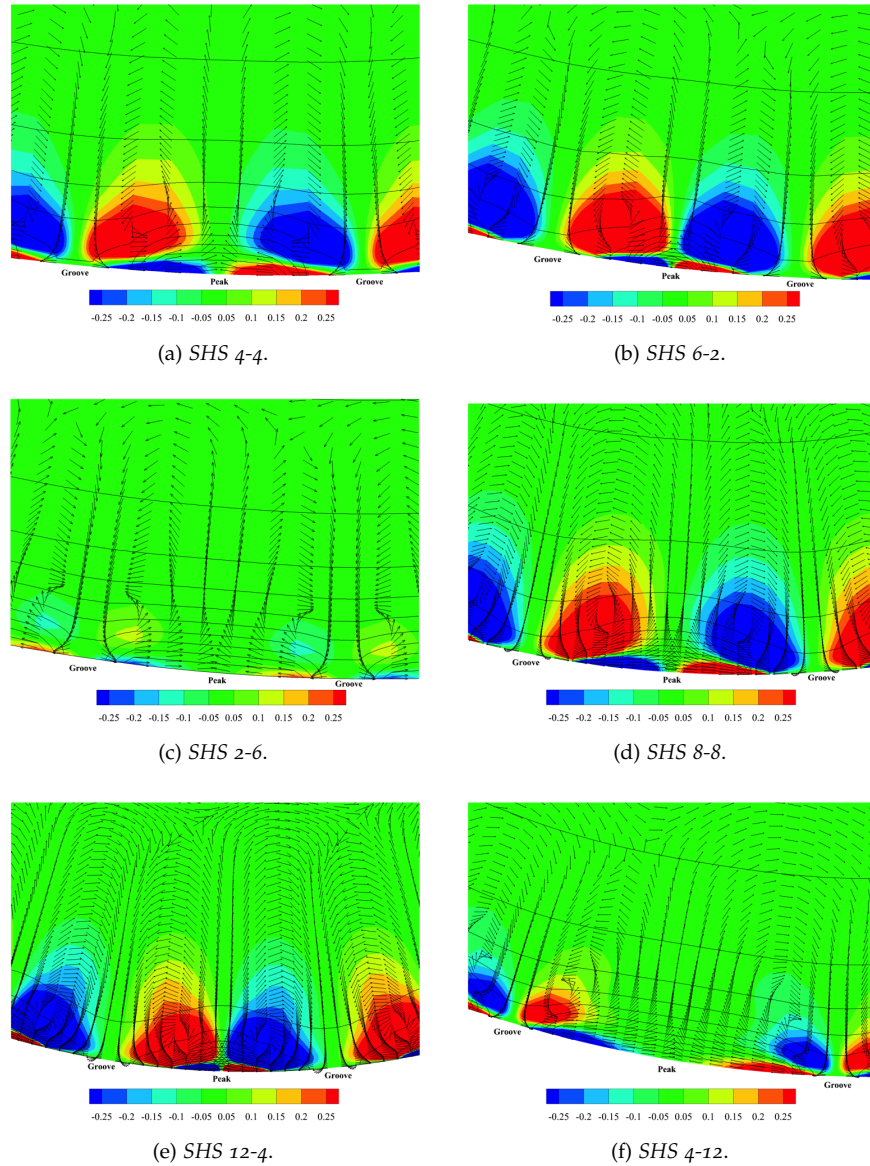


Figure 6.7: Two dimensional mean vorticity along z direction in correspondence of grooves and peaks (flood colours); representation of $\langle u_x \rangle |_\vartheta$, $\langle u_y \rangle |_\vartheta$ (black vectors); whereas the longitudinal mean velocity $\langle u_z \rangle |_\vartheta$ to represent the portion of the solid boundary (black isoline). The interval of values is fixed for all simulations.

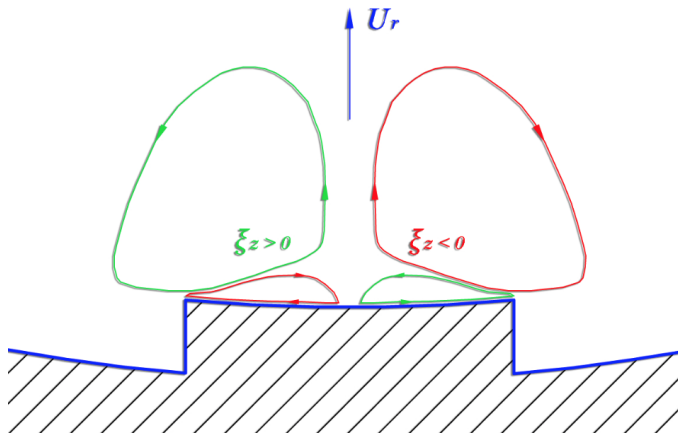


Figure 6.8: Schematic representation of vortical structures: principal (big one) and secondary (small one).

6.1.3 Phase velocity

Using the phase average, it is possible to reconstruct the mean velocities profiles of $\langle u_z \rangle^+ |_g$, concerning zones of different nature. In figure 6.9a the velocity profiles are reported, related to groove zones (slip) and in figure 6.9c those of peaks (no-slip). These trends confirm that shown in figure 6.2a: the velocity in the slip zone increases with the width of grooves; whereas it is zero at the wall peaks. It is also possible to note in figure 6.9b that in the slip zone the shear stress at the wall τ_w is zero because the gradient at the wall is infinity i.e. $1/\tau_w \rightarrow 0$. The result is different for the peaks zones (no-slip). In this case one has to consider the balance of forces

$$\Delta p A = \tau_w A_w = \tau_w A_c \phi_s \quad (6.5)$$

where Δp , A , A_c and ϕ_s are, respectively: the imposed pressure gradient, the area of pipe section, the side area of pipe and the solid fraction. Then the equation can be rewritten (6.5) in two equivalent forms

$$\tau_w = \frac{\Delta p A}{A_c} \frac{1}{\phi_s} \quad (6.6)$$

$$\frac{1}{\tau_w} = \frac{A_c}{\Delta p A} \phi_s \quad (6.7)$$

In the figure 6.9d, the velocity at the wall is zero (no-slip zones) and here a finite gradient is present, i.e. τ_w is finite. It can be noticed that, as the width of peaks increases, also the gradient grows, so that τ_w decrease. This fact is demonstrated by the equation (6.6), where Δp , A and A_c are kept constant: as the solid fraction ϕ_s increases, τ_w decreases. Therefore the simulations SHS with the same ϕ_s will have the same wall shear stress. A physical explanation for this trend is that the increase of solid fraction leads to a growth of peak width, so there is more surface where the forces can unload and this implies a reduction of τ_w .

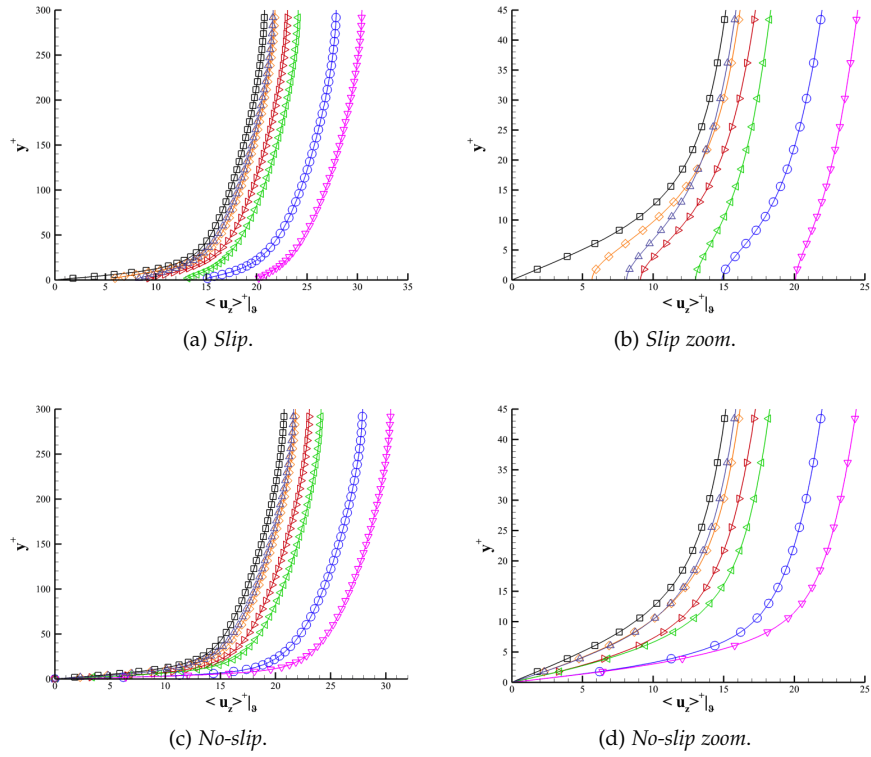


Figure 6.9: Trend of y^+ as a function of velocity $\langle u_z \rangle^+ |_9$ for (a) slip zones; (c) no-slip zones and (b), (d) their magnification near the wall. The symbol + indicates the variables express in terms of wall units, having adimensionalized with u_τ where the characteristics parameters are $Re_N = 5000$ and $Re_\tau = 311.35$. The simulation performed are: smooth surface (black line \square); SHS with 4 slip-4 no-slip cells (red line \triangle); SHS with 8 slip-8 no-slip cells (green line \triangledown); SHS with 6 slip-2 no-slip cells (blue line \triangleright); SHS with 12 slip-4 no-slip cells (pink line \triangleleft); SHS with 2 slip-6 no-slip cells (orange line \diamond); SHS with 4 slip-12 no-slip cells (dark blue line \circlearrowright).

6.2 REYNOLDS STRESS

In figure 6.10 the profiles of the components of the Reynolds tensor are shown: $\langle u_z'^2 \rangle$, $\langle u_r'^2 \rangle$, $\langle u_\theta'^2 \rangle$ and $\langle u_z' u_r' \rangle$. One can notice that maxima of superhydrophobic surface are slightly shifted near the wall, compared with the smooth simulation. Moreover, the width of the grooves influence the intensity of fluctuations of velocity averages near the wall, increasing the contribution of drag linked to the turbulent part. The contribution of $\langle u_z' u_r' \rangle$, which identifies the Reynolds' stress, are represented in figure 6.10d. This component is zero at the wall and reach a maximum in the buffer layer. Through these components one can have an evaluation of the contribution of the turbulence which results to grow with the width of grooves. This behaviour is in line with the trend of vortical structure shown in figure 6.7.

The contribution deriving from the *viscous stresses* and *Reynolds stresses* for the seven cases are reported in figure 6.11. As expected by the theory, the

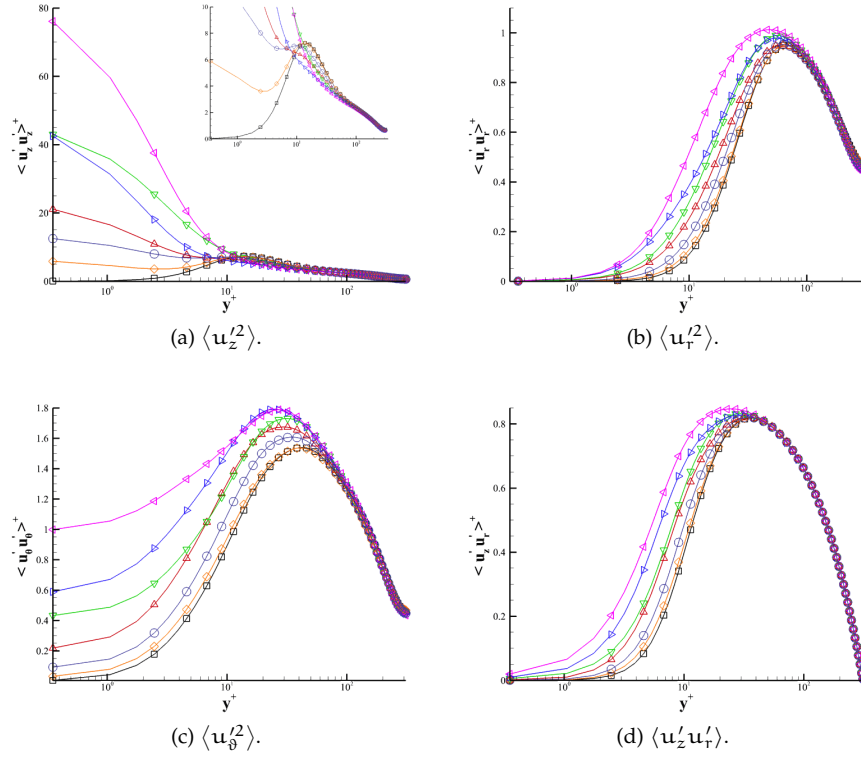


Figure 6.10: Mean fluctuations velocities for the seven cases: (a) $\langle u_z'^2 \rangle$; (b) $\langle u_r'^2 \rangle$; (c) $\langle u_\theta'^2 \rangle$, (d) $\langle u_z' u_r' \rangle$ as a function of the distance from the wall y^+ in semi-logarithmic scale. The symbol + indicates the variables express in terms of wall units, having adimensionalized with u_τ where the characteristics parameters are $Re_N = 5000$ and $Re_\tau = 311.35$. The simulation performed are: smooth surface (black line \square); SHS with 4 slip-4 no-slip cells (red line \triangle); SHS with 8 slip-8 no-slip cells (green line \triangledown); SHS with 6 slip-2 no-slip cells (blue line \triangleright); SHS with 12 slip-4 no-slip cells (pink line \triangleleft); SHS with 2 slip-6 no-slip cells (orange line \diamond); SHS with 4 slip-12 no-slip cells (dark blue line \circlearrowleft).

Reynolds stresses are zero at the wall, maximum in the buffer layer ($r \approx 0.2$) and then go again to zero at the centre of pipe. On the contrary, the viscous stresses exhibit a maximum at the wall, then decrease rapidly up to $r \approx 0.2$ and are zero at the centre of pipe. In any case the stresses of simulations performed does not deviate too much with respect to the smooth case. As said before, the Reynolds stresses grow with the width of groove (see figure 6.10d). Figure 6.11 underlines that, since the total stress is always a constant straight line, the viscous one tends to decrease with the width of grooves.

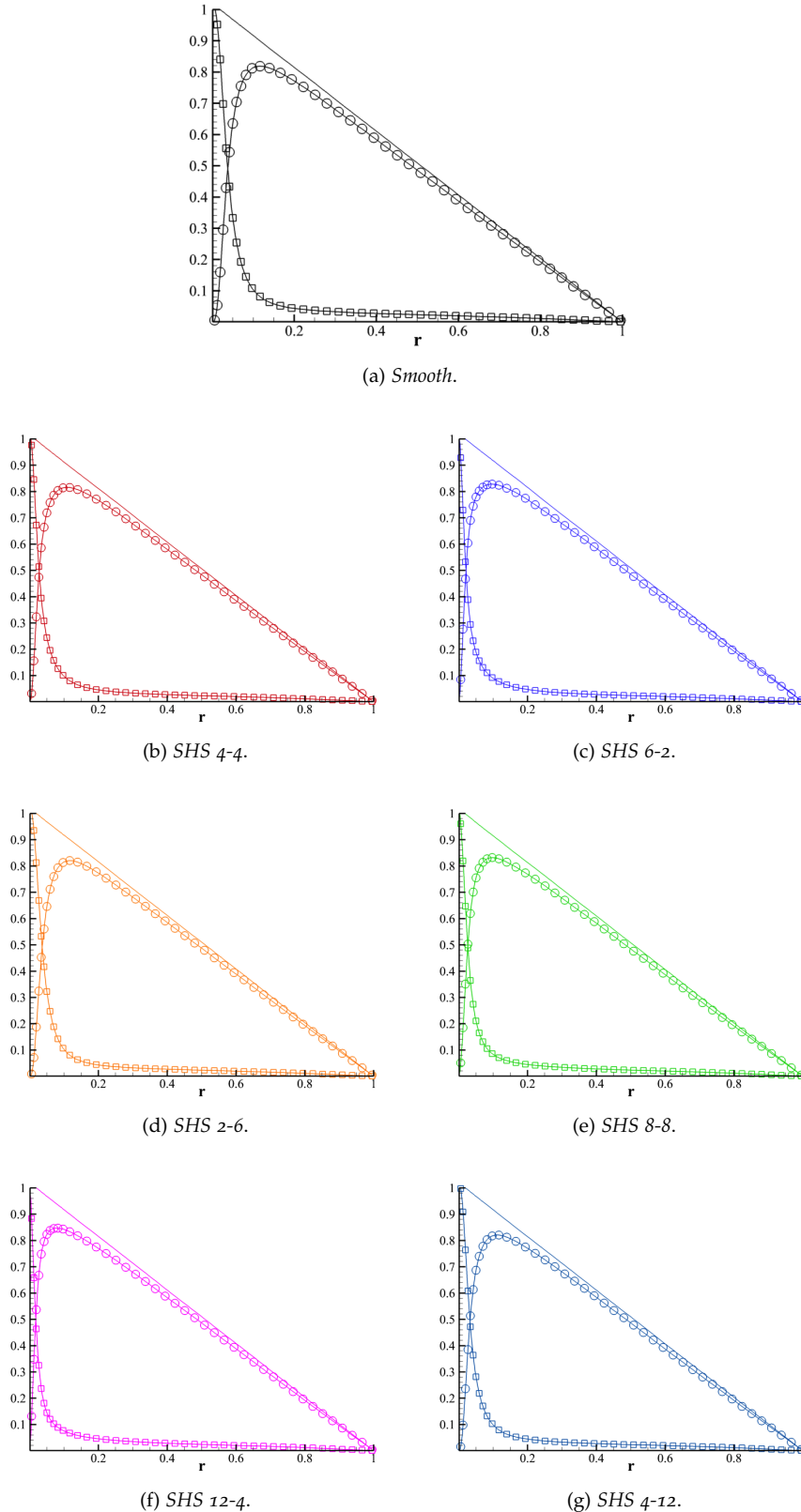


Figure 6.11: Representation of Reynolds stress τ_v (line \square), viscous stress τ_R (line \circ) and total stress τ_{Tot} (line \triangle) as a function unitary radius r . The simulation performed are: (a) smooth surface (black); (b) SHS with 4 slip-4 no-slip cells (red); (c) SHS with 6 slip-2 no-slip cells (blue); (d) SHS with 2 slip-6 no-slip cells (orange); (e) SHS with 8 slip-8 no-slip cells (green); (f) SHS with 12 slip-4 no-slip cells (pink) and (g) SHS with 4 slip-12 no-slip cells (dark blue).

6.3 FUKAGATA'S BALANCE

The quantitative relation between the statistical information of the flow and the drag reduction effect seems to remain not completely clear. Fukagata *et al.* [12] derive an equation for different dynamical effects that produce frictional drag in turbulent pipe flows. The result is suggestive and useful for analyzing the effect of the Reynolds stress on the drag. The Fukagata's balance is (see Appendix A)

$$\mu R^2 (U_b - U_{\text{slip}}) - \int_0^R r^2 \tau_r dr = -\frac{1}{8} \left. \frac{dp}{dz} \right|_0 R^4 \quad (6.8)$$

where the different terms describe the work spent, respectively by: the flow velocity, the slip velocity, of the Reynolds stresses and finally, of the pressure gradient which is maintained constant. This equation can assume several forms related to assumption of the flow that one considers. Here three cases of interest are reported:

- *Laminar case*, where the surface is entire no-slip, with $U_{\text{slip}} = 0$ and $\tau_r = 0$

$$\mu R^2 U_b = -\frac{1}{8} \left. \frac{dp}{dz} \right|_0 R^4 \quad \text{Pouiseille's equation} \quad (6.9)$$

in this case all contributions, given by the pressure gradient, are balanced by viscous stress at the wall.

- *Turbulent case*, where the surface is entire no-slip, $U_{\text{slip}} = 0$

$$\mu R^2 U_b - \int_0^R r^2 \tau_R dr = -\frac{1}{8} \left. \frac{dp}{dz} \right|_0 R^4 \quad (6.10)$$

if one takes into account a turbulent flow, the constant pressure gradient is balanced by two different terms: one related to the flow velocity and the other linked to the Reynolds stress τ_R . Therefore, fixed the constant pressure gradient, the mass flow rate decreases due to the τ_R in the turbulent regime compared to the laminar.

- *Turbulent case*, where there is a slip condition on the surface

$$\mu R^2 U_b - \mu R^2 U_{\text{slip}} - \int_0^R r^2 \tau_R dr = -\frac{1}{8} \left. \frac{dp}{dz} \right|_0 R^4 \quad (6.11)$$

The latter case considers the presence of a slip boundary condition at the wall and it is useful to discuss what happens within a pipe with a super-hydrophobic surface. This balance is presented in figure 6.12, comparing the cases where $L=8$ or $L=16$ are involved. Figure 6.12a shows the trend of the Fukagata's terms as a function of the *free fraction* ($100 - \phi_s$), which is defined as complementary of the *solid fraction* ϕ_s . For the smooth case ($100 - \phi_s = 0$), in figure 6.12, the slip velocity is zero, and corresponds to the case of equation (6.10).

For a free fraction ($100 - \phi_s$) = 75%, inserted into simulation SHS 6-2, the τ_R increases and since the pressure gradient is constant, the contribution of

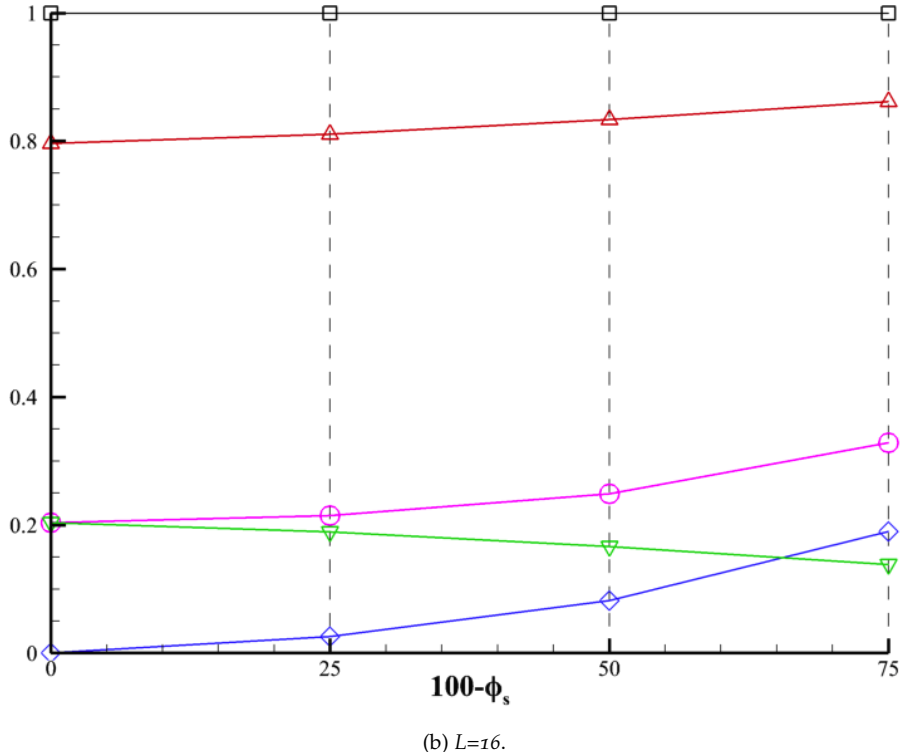
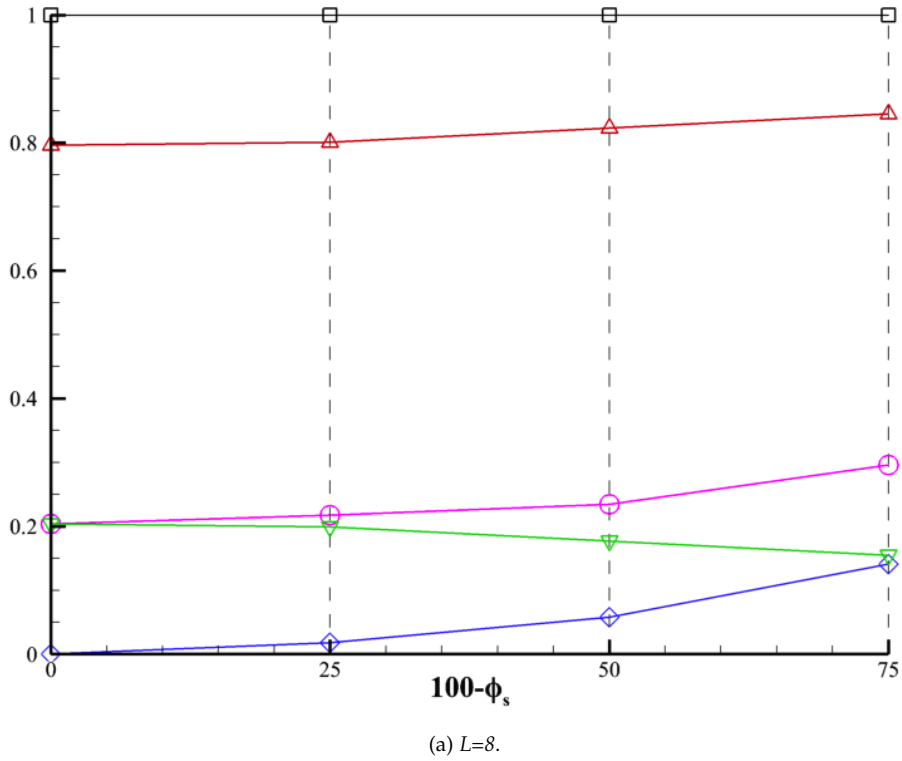


Figure 6.12: Fukagata's balance normalised as the pressure gradient $7.78 \cdot 10^{-2}$. (a) referred to the simulations where $L=8$ and (b) referred to the simulations where $L=16$ as a function of *interface fraction* ($100 - \phi_s$). The terms of Fukagata's balance are: bulk velocity U_b (purple line ○); slip velocity U_s (blue line ◇); difference between bulk and slip velocity $U_b - U_s$ (green line ▽); Reynolds stress τ_R (red line △); total of all contributes Total (black line □).

$(U_b - U_{\text{slip}})$ into equation (6.11) has to decrease (see *green line* ∇ in figure 6.12a). Furthermore, if U_s increases with the width of grooves, the term U_{slip} into equation (6.11) inevitably must increase too. Therefore, the mass flow rate increases, confirming the discussion of paragraph 6.1.1. In figure 6.12a, the contribution of τ_R decreases with the interface fraction $(100 - \phi_s)$, so for the Fukagata's balance, the $(U_b - U_{\text{slip}})$ has to increase, and this is confirmed by the *green line* (∇). A similar reasoning can be done for the plot in figure 6.12b. Here, all contributions increase in comparison with the cases of figure 6.12a. In conclusion, the Fukagata's balance is useful to evaluate the weight of different contributions when a superhydrophobic surface for a turbulent flow is present.

6.4 PRESSURE FIELD

The two-dimensional fields of the mean pressure, obtained by the computation of the average in phase along ϑ [33], so that depend only from r and z , is shown in figure 6.13. In correspondence of liquid-gas interface the mean pressure values are negative, while at the solid wall positive values are observed. As the groove width increases, the mean pressure tends to be stronger. It is noteworthy to observe that the value of mean pressure is very small if compared with that of the pressure fluctuations; in other words it would not influence the stability of the interface.

6.4.1 Probability density function

Assuming that the system is in the Cassie state, i.e. gas is present within the grooves, and to study the stability of this state, it is useful to analyse the pressure fluctuations. The distribution of the fluctuations are evaluated through the probability density function which expresses the probability to find a certain variation of the pressure at the interface. To evaluate the probability density function (PDF) for the six cases, the values of the pressures at the halfway points of slip zones are registered in the three reference sections of the pipe $z = \pi/2, \pi, 3\pi/2$. For each section one will obtain three different fields. Finally, to increase the statistics, these are averaged each others. A step $\Delta p = 2p_{\max}/N_p$ is selected to reconstruct the PDF, where p_{\max} is the maximum value between three section and $N_p = 300$ is the number of points used to discretise the variation field.

Figure 6.14a shows the trends of the PDFs for the cases where eight cells are involved. Here one notices that the reference case, the smooth one, exhibits a narrower distribution of pressure fluctuations in comparison with the other cases. Increasing the width of the grooves, the range of pressure fluctuation increases, and the shape of PDF curves become broader. In figure 6.14b the cases are compared with a pattern of sixteen cells. The trend is the same of the case explained above. In this situation the width of groove is larger, so the maxima and minima values of pressure fluctuations are higher, as confirmed numerically in the table 7. In order to see how much the PDFs deviate from the gaussian behaviour, they are normalized to their standard deviation σ and compared with normalized standard gaussian curve (see figure 6.15). In all cases they exhibit a trend very similar to the gaussian.

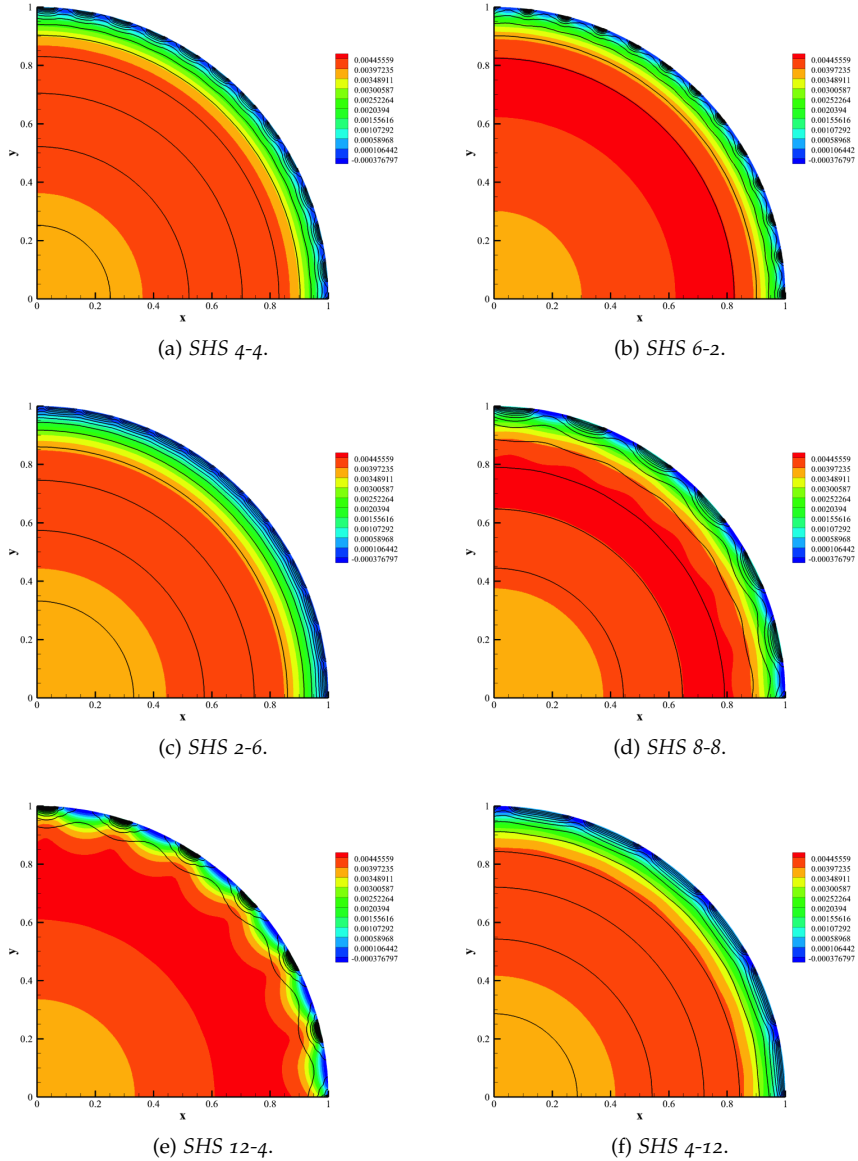


Figure 6.13: Two dimensional plot of mean pressure $\langle p \rangle|_\vartheta$ (*flood colours*) and the longitudinal mean velocity $\langle u_z \rangle|_\vartheta$ to represent the portion of the solid boundary (*black isoline*). The range of the scale is the same for all simulations.

Computing the *skewness* [25] (asymmetric index), which is defined as $s = m_3/m_2^{3/2}$ where m_i are the statistics moment of i -th order, one can evaluate the weigh of the left and right events in terms of probability. In table 7 the skewness s , except for the smooth case, is negative and this means that the negative pressure fluctuations are much probable to positive one. In particular, it is more likely to find a negative pressure fluctuations, i.e. under the mean value, than positive values. Finally one can notice in both figures 6.14 and 6.15, that all curves are larger than the reference gaussian. The second

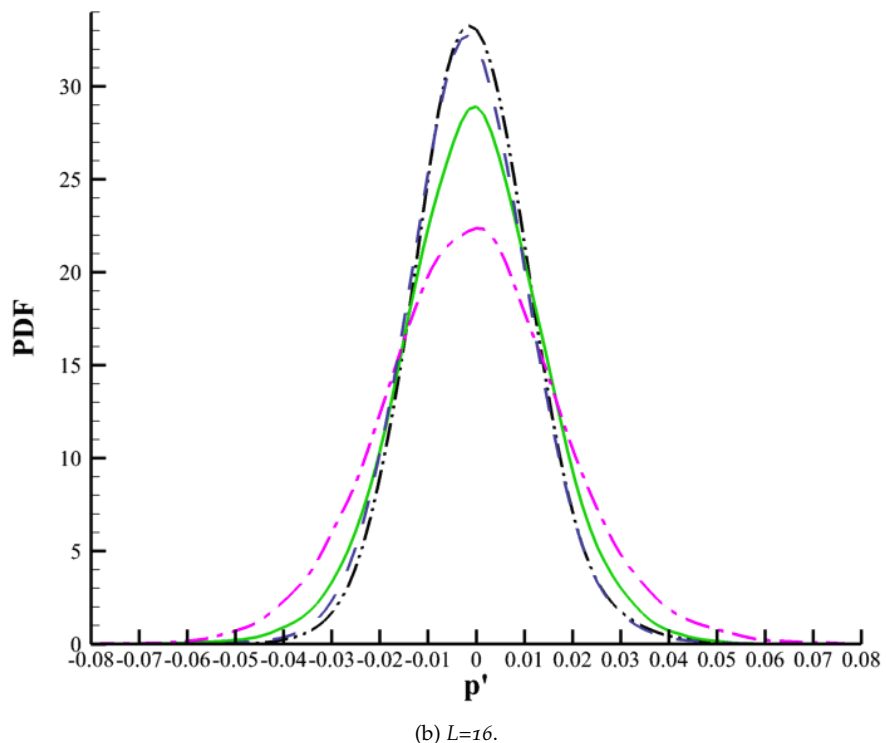
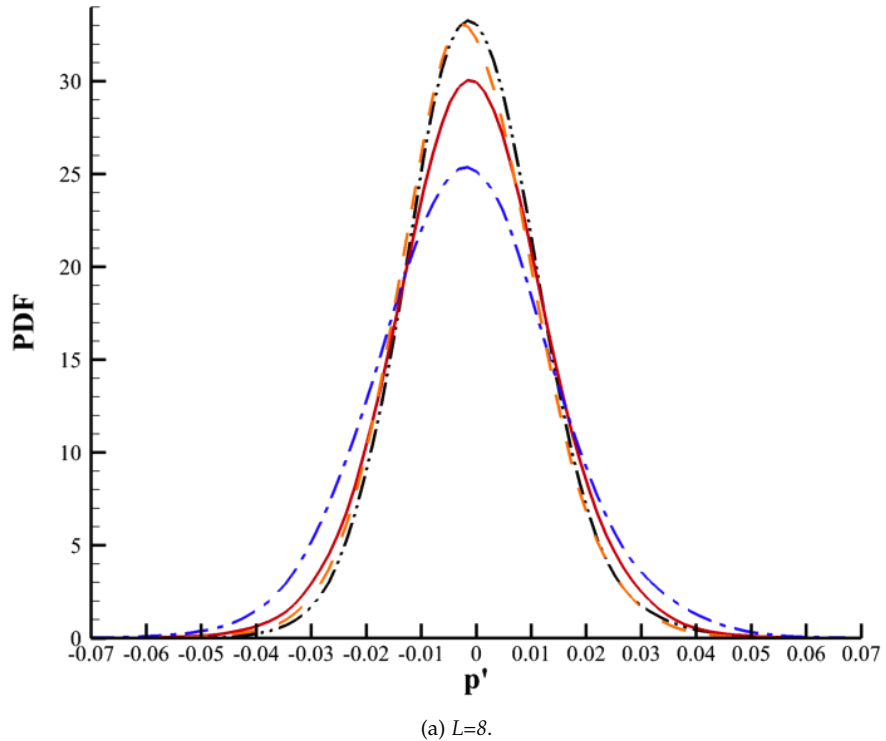


Figure 6.14: (a) Probability density functions (PDF) for the cases where $L=8$: smooth surface (black $\cdots\cdots$); SHS with 4 slip-4 no-slip cells (red line); SHS with 6 slip-2 no-slip cells (blue line $- \cdot -$); SHS with 2 slip-6 no-slip cells (orange line $- - -$). (b) Cases where $L=16$: smooth surface (black $\cdots\cdots$); SHS with 8 slip-8 no-slip cells (green line); SHS with 12 slip-4 no-slip cells (pink line $- \cdot -$); SHS with 4 slip-12 no-slip cells (dark blue line $--$).

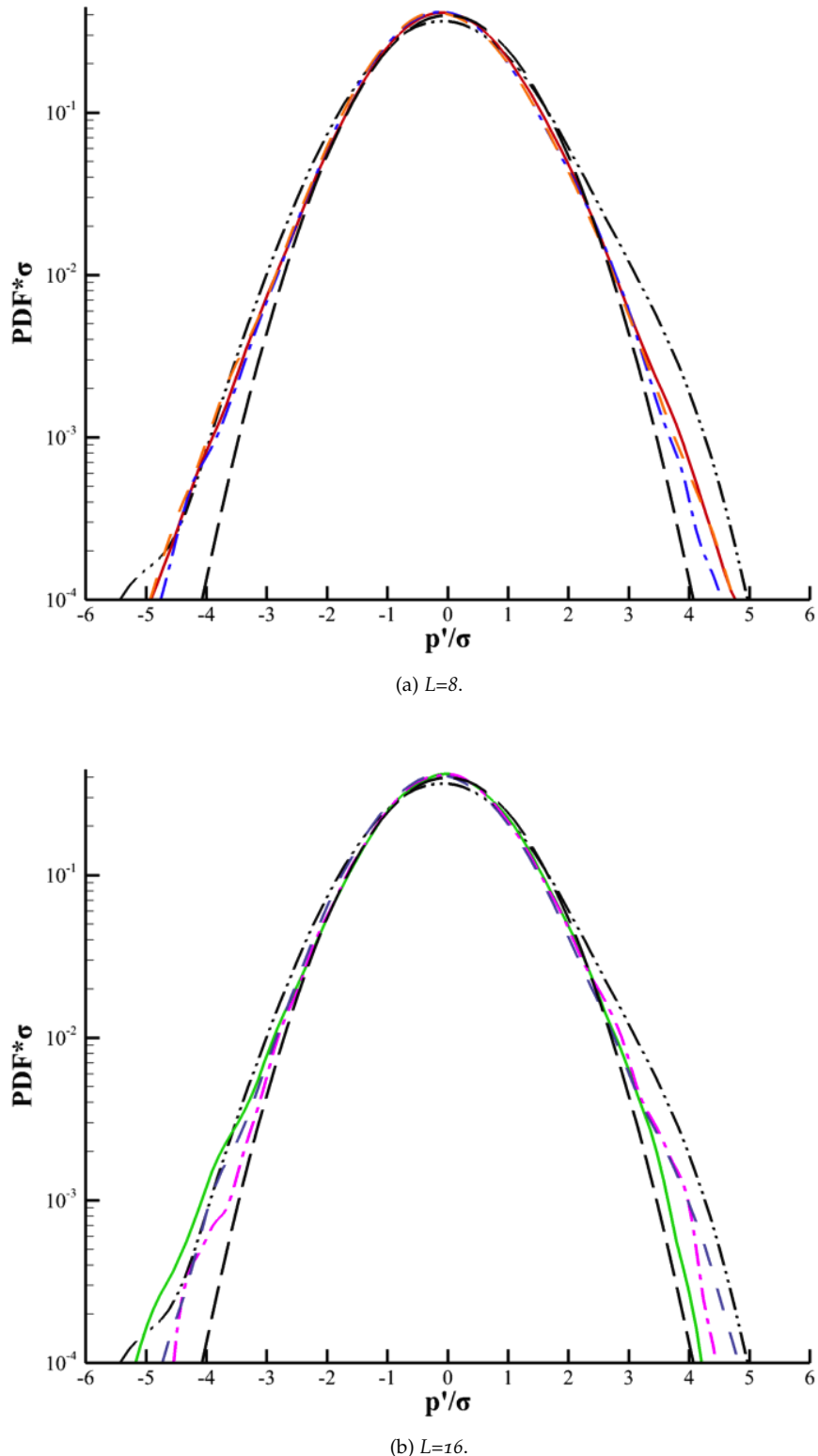


Figure 6.15: Probability density functions (PDF) normalized with the standard deviation σ and compared to the Gaussian curve (black long --). **(a)** cases where $L=8$: smooth surface (black $- \cdots -$); SHS with 4 slip-4 no-slip cells (red line); SHS with 6 slip-2 no-slip cells (blue line $- \cdot - \cdot -$); SHS with 2 slip-6 no-slip cells (orange line $- \cdots -$). **(b)** Cases where $L=16$: smooth surface (black $- \cdots -$); SHS with 8 slip-8 no-slip cells (green line); SHS with 12 slip-4 no-slip cells (pink line $- \cdots -$); SHS with 4 slip-12 no-slip cells (dark blue line $- \cdots -$).

Case	Smooth	2-6	4-4	6-2	4-12	8-8	12-4
σ	0.0119	0.0125	0.0137	0.0164	0.0126	0.0145	0.0186
$s(10^{-3})$	1.894	0.689	0.578	1.294	1.265	-0.741	1.809
f	3.561	3.600	3.556	3.456	3.527	3.525	3.423
p'_{\max}	+0.059	+0.069	+0.082	+0.091	+0.075	+0.069	+0.086
p'_{\min}	-0.069	-0.083	-0.080	-0.088	-0.067	-0.083	-0.087

Table 7: Here are reported the values of standard deviation σ , skewness s , flatness f and the values of the pressure fluctuations p'_{\max} and p'_{\min} .

significant parameters is the *flatness* [25] $f = m_3/m_2^2$, which is the measure of the combined weight of the tails relative to the rest of the distribution. In the SHS simulations the flatness is greater than three (see table 7) i.e. the distribution has heavier tails. This result underlines the intermittent behaviour of the turbulent flows, i.e. intense events, for example those above 5σ , are more probable when compared to their rate in a standard gaussian distribution.

CONCLUSIONS

In this work the drag reduction obtained by the use of superhydrophobic surfaces within the turbulent pipe flow has been investigated through direct numerical simulations (DNS). It is noteworthy to stress that while in the planar channel flow the effect of superhydrophobic surfaces is extensively investigated, this is the first time that the analysis is performed on the flow in a turbulent pipe. The flow on the surface of a micro-structured pipe with grooves (micro-cavities) aligned to the span-wise direction, has been modelled through free-slip boundary conditions.

Seven cases at different solid fractions ϕ_s , i.e. the wall to overall surface ratios, and different widths of the groove, have been studied. The mean velocity profiles have been reconstructed to determine the dynamics of the flow within the pipe. The result of the study has shown that, in the case of superhydrophobic surfaces, the velocities along the z coordinate are higher than in a smooth configuration. In fact, as the width of the groove increases, the velocity profiles are modified and they deviate considerably from the smooth case. This trend underlines that the presence of a slip velocity produced by the groove zone, contributes positively to the drag reduction, but only in a first approximation, due to its coupling with turbulence. A positive increase of mass flow rate, i.e. a drag reduction, is observed, due to the prevalence of the contribute given by slip velocity with respect to the one of turbulence.

The dynamic behaviour of the interface has been evaluated computing the mean radial velocity through an average in phase. The radial velocity in correspondence of the grooves is positive, showing that the fluid tends to push the interface towards the bottom of the grooves, while at the peak the behaviour is opposite. The presence of a superhydrophobic surface modifies also the turbulent structures at the wall. The vortical structures are affected by the solid fraction ϕ_s and they tend to be stronger as ϕ_s decreases. These are linked to the trend of the Reynolds stresses component $\langle u'_z u'_r \rangle$ which has the same behaviour.

However, a deeper understanding of drag reduction, and of the read effectiveness of superhydrophobic surfaces, has requested more investigation. Therefore, using a momentum balance, originally introduced by Fukagata, individual contributions to the dynamical effects that produce frictional drag in turbulent pipe flows, have been singled out. The outcome of this analysis is that maintaining the pressure gradient constant, and decreasing the solid fraction, Reynolds stresses increase and therefore the difference between the bulk (U_b) and the slip (U_{slip}) velocities decreases. This effect is more beneficial to drag reduction, when compared with the smooth case.

Finally the average and fluctuations of the pressure have been reconstructed in order to examine the stability of the interface liquid-vapour (Cassie state). The pressure fluctuations have been studied through the analysis of the probability density functions (PDF). The process appear to be gaussian, limiting therefore possible pressure asymmetry effects. The present study has also shown that

increasing the width of the grooves, the range of pressure fluctuations rises up. It is important to recall that the pressure fluctuations in the turbulent flow strongly affect the stability of the Cassie-Baxter state, which is assumed in the present investigation. In fact, the Wenzel state does not bring any advantage in terms of drag reduction, but it produces negative effects.

This work has demonstrated that, when compared to a smooth surface, positive drag reduction increments are obtained at different values of superhydrophobic solid fractions, as reported in table 8. The effect increases as the solid fraction decreases. Configurations with identical solid fractions, but different in groove width, show slightly different drag reduction values.

An interesting follow-up of this work would consist in the investigation of the liquid-gas interface, to study its stability, and implementing a more realistic model, i.e. a *movable interface*. In this case, the interface is free to move with its own velocity, and the pressure field can trigger its dynamics.

Case	Smooth	4-12	2-6	4-4	8-8	6-2	12-4
ϕ_s	100%	75%	75%	50%	50%	25%	25%
DR	Ref.	6%	7%	15%	22%	45%	62%

Table 8: Drag reduction increment ($(U_b - U_{ref})/U_{ref}$) compared to the reference (Ref.) smooth case for different configurations (ϕ_s being the solid fraction).

Part IV
APPENDIX

A

FUKAGATA'S BALANCE

Fukagata *et al.* [12] derive an expression of the componential contributions that different dynamical effects make to the frictional drag in turbulent pipe flows. The local skin friction can be decomposed into four parts, i.e., laminar, turbulent, inhomogeneous and transient components, the second of which is a weighted integral of the Reynolds stress distribution. Starting from the Reynolds averaged Navier-Stokes momentum equation in cylindrical coordinates

$$0 = -\frac{dp}{dz}\Big|_0 + \frac{1}{r} \frac{d}{dr} \left[r \left(\mu \frac{d \langle u_z \rangle}{dr} + \tau_r \right) \right] \quad (\text{A.1})$$

where $\tau_r = -\rho \langle u'_r u'_z \rangle$. Now applying triple integration between $[0, r]$, the first integration essentially gives the force balance

$$0 = -\frac{dp}{dz}\Big|_0 r + \frac{d}{dr} \left[r \left(\mu \frac{d \langle u_z \rangle}{dr} + \tau_r \right) \right] \quad (\text{A.2a})$$

$$0 = -\frac{1}{2} \frac{dp}{dz}\Big|_0 r^2 + r \left(\mu \frac{d \langle u_z \rangle}{dr} + \tau_r \right) \quad (\text{A.2b})$$

$$\mu \frac{d \langle u_z \rangle}{dr} + \tau_r = \frac{1}{2} \frac{dp}{dz}\Big|_0 r$$

$$\mu \langle u_z(r) \rangle - \mu \langle u_z(0) \rangle + \int_0^r \tau_r(\rho) d\rho = \frac{1}{4} \frac{dp}{dz}\Big|_0 r^2 \quad (\text{A.2c})$$

for the boundary conditions $\langle u_z(0) \rangle = 0$ in the no-slip region, whereas $\langle u_z(0) \rangle = U_{\text{slip}}$ in the slip region. For $r = R$

$$\mu U_{\text{slip}} - \mu \langle u_z(0) \rangle + \int_0^R \tau_r(\rho) d\rho = \frac{1}{4} \frac{dp}{dz}\Big|_0 R^2 \quad (\text{A.3})$$

Going to subtract the equation (A.3) to (A.2c),

$$\underbrace{-\frac{1}{4} \frac{dp}{dz}\Big|_0 (R^2 - r^2)}_4 = \underbrace{-\int_0^R \tau_r(\rho) d\rho}_3 + \underbrace{\int_0^r \tau_r(\rho) d\rho}_2 + \underbrace{\mu (\langle u_z(r) \rangle - U_{\text{slip}})}_1 \quad (\text{A.4})$$

Now integrating on the section of pipe $A=[0, 2\pi] \times [0, R]$, i.e., $\int_0^{2\pi} r d\theta \int_0^R r dr$ the equation (A.4), for each terms one obtains

1.

$$\begin{aligned} & 2\pi\mu \int_0^R (\langle u_z(r) \rangle - U_{\text{slip}}) r dr \\ &= 2\pi\mu \left[\int_0^R \langle u_z(r) \rangle r dr + \int_0^R U_{\text{slip}} r dr \right] \\ &= 2\pi\mu \left[\frac{U_b R^2}{2} + \frac{U_{\text{slip}} R^2}{2} \right] = \pi R^2 \mu (U_b - U_{\text{slip}}) \end{aligned} \quad (\text{A.5})$$

2.

$$2\pi \int_0^R \left(\int_0^r \tau_r d\rho \right) r dr = \pi R^2 \int_0^R \tau_r dr \quad (\text{A.6})$$

3.

$$\begin{aligned} 2\pi \int_0^R \left(\int_0^r \tau_r d\rho \right) r dr &= 2\pi \int_0^R F(r) r dr \\ &= 2\pi \left[\frac{r^2}{2} F(r) \Big|_0^R - \int_0^R \frac{r^2}{2} F'(r) dr \right] \\ &= \pi \left[R^2 F(R) - \int_0^R r^2 \tau_r dr \right] = \\ &= \pi \left[R^2 \int_0^R \tau_r dr - \int_0^R r^2 \tau_r dr \right] = \pi \int_0^R (R^2 - r^2) \tau_r dr \end{aligned} \quad (\text{A.7})$$

4.

$$\begin{aligned} 2\pi \int_0^R \frac{1}{4} \frac{dp}{dz} \Big|_0 (R^2 - r^2) r dr \\ &= 2\pi \frac{1}{4} \frac{dp}{dz} \Big|_0 \left(\frac{1}{2} R^2 r^2 - \frac{1}{2} r^4 \right)_0^R \\ &= \frac{\pi}{2} \frac{dp}{dz} \Big|_0 \left(\frac{1}{2} - \frac{1}{4} \right) R^4 = \frac{\pi}{8} \frac{dp}{dz} \Big|_0 R^4 \end{aligned} \quad (\text{A.8})$$

Therefore rewriting all contributes and considering the simplifications

$$\mu R^2 (U_b - U_{\text{slip}}) - \int_0^R r^2 \tau_r dr = -\frac{1}{8} \frac{dp}{dz} \Big|_0 R^4 \quad (\text{A.9})$$

Shown below, there are the three cases of interest

- Laminar case, where the surface is entire no-slip, with $U_{\text{slip}} = 0$ and $\tau_r = 0$

$$\mu R^2 U_b = -\frac{1}{8} \frac{dp}{dz} \Big|_0 R^4 \quad \text{Poiselle's equation} \quad (\text{A.10})$$

- Turbulent case, where the surface is entire no-slip, $U_{\text{slip}} = 0$

$$\mu R^2 U_b - \int_0^R r^2 \tau_r dr = -\frac{1}{8} \frac{dp}{dz} \Big|_0 R^4 \quad (\text{A.11})$$

- Turbulent case, where there is a slip condition on the surface

$$\mu R^2 U_b - \mu R^2 U_{\text{slip}} - \int_0^R r^2 \tau_r dr = -\frac{1}{8} \frac{dp}{dz} \Big|_0 R^4 \quad (\text{A.12})$$

The advantage in the series of relations derived above is that one can quantitatively identify each dynamical contribution to the drag reduction/enhancement even for a manipulated flow. For a fully developed turbulent pipe flow, consistent with the DNS data results obtained by Choi *et al.* [7], the equation (A.12) offers a different point of view for explaining the phenomenon of drag reduction in a turbulent flow.

B

DISCRETISATION OF POISSON'S EQUATION

Here is reported the numerical computation of the Poisson's equation (5.11), considering that the domain is discretised like in figure B.1). Reporting the all steps for arriving to the equation (5.20):

$$\nabla^2 \phi = -\nabla \cdot \tilde{u} \quad (\text{B.1})$$

Now rewriting the Laplacian term in cylindrical coordinates, one obtains

$$\frac{1}{r} \frac{\partial}{\partial r} \left(r \frac{\partial \phi}{\partial r} \right) + \frac{1}{r^2} \frac{\partial^2 \phi}{\partial \vartheta^2} + \frac{\partial^2 \phi}{\partial z^2} = -\nabla \cdot \tilde{u} = f \quad (\text{B.2})$$

Applying the Fourier series expansion to $\phi(r, \vartheta, z) = \hat{\phi}(r)_{k_\vartheta, k_z} e^{-jk_\vartheta \vartheta} e^{-jk_z z}$ and substituting it into (B.2)

$$\frac{1}{r} \frac{\partial}{\partial r} \left(r \frac{\partial \hat{\phi}}{\partial r} \right) - \frac{\hat{\phi}}{r^2} k_\vartheta^2 - \hat{\phi} k_z^2 = \hat{f} \quad (\text{B.3})$$

$$\frac{1}{r} \frac{\partial}{\partial r} \left(r \frac{\partial \hat{\phi}}{\partial r} \right) - \left(\frac{k_\vartheta^2}{r^2} + k_z^2 \right) \hat{\phi} = \hat{f} \quad (\text{B.4})$$

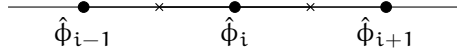


Figure B.1: One dimensional mesh, where the scalar quantities ϕ is located in the middle of two consecutive nodes.

Now making a discretisation of the first term of the equation (B.4):

$$\frac{1}{r} \frac{\partial}{\partial r} \left(r \frac{\partial \hat{\phi}}{\partial r} \right) = \frac{1}{r} \frac{\partial}{\partial r} (q) = \frac{1}{r_i} \frac{q_I - q_{I-1}}{\Delta r_i} \quad (\text{B.5})$$

where the terms of the equation (B.5) can be expressed as

$$q_I = r_I \frac{\hat{\phi}_{i+1} - \hat{\phi}_i}{r_{i+1} - r_i}, \quad r_I = \frac{r_{i+1} + r_i}{2}$$

$$q_{I-1} = r_{I-1} \frac{\hat{\phi}_i - \hat{\phi}_{i-1}}{r_i - r_{i-1}}, \quad r_{I-1} = \frac{r_i + r_{i-1}}{2}$$

$$\Delta r_i = r_I - r_{I-1} = \frac{r_{i+1} - r_{i-1}}{2}$$

so the equation (B.4) becomes:

$$\frac{1}{r_i \Delta r_i} \left[r_I \frac{\hat{\phi}_{i+1} - \hat{\phi}_i}{r_{i+1} - r_i} - r_{I-1} \frac{\hat{\phi}_i - \hat{\phi}_{i-1}}{r_i - r_{i-1}} \right] - \left(\frac{k_\vartheta^2}{r^2} + k_z^2 \right) \hat{\phi} = \hat{f} \quad (\text{B.6})$$

$$\frac{1}{r_i \Delta r_i} \left[\frac{r_I}{\Delta r_I} \hat{\phi}_{i+1} - \left(\frac{r_I}{\Delta r_I} + \frac{r_{I-1}}{\Delta r_{I-1}} \right) \hat{\phi}_i + \frac{r_{I-1}}{\Delta r_{I-1}} \hat{\phi}_{i-1} - \left(\frac{k_\vartheta^2}{r^2} + k_z^2 \right) \hat{\phi} \right] = \hat{f} \quad (\text{B.7})$$

with $\Delta r_I = r_{i+1} - r_i$ and $\Delta r_{I-1} = r_i - r_{i-1}$. Collecting constant terms in three variables α , β and γ :

$$\alpha = \frac{1}{r_i \Delta r_i} \frac{r_{I-1}}{\Delta r_{I-1}} \quad (\text{B.8})$$

$$\beta = -\frac{1}{r_i \Delta r_i} \left(\frac{r_I}{\Delta r_I} + \frac{r_{I-1}}{\Delta r_{I-1}} \right) - \left(\frac{k_\theta^2}{r^2} + k_z^2 \right) \quad (\text{B.9})$$

$$\gamma = \frac{1}{r_i \Delta r_i} \frac{r_I}{\Delta r_I} \quad (\text{B.10})$$

So the equation (B.4) can be written as

$$\alpha \hat{\phi}_{i-1} + \beta \hat{\phi}_i + \gamma \hat{\phi}_{i+1} = \hat{f} \quad (\text{B.11})$$

BIBLIOGRAPHY

- [1] Giacomello A. "Metastable states in the wetting of rough hydrophobic surfaces." 2013.
- [2] J. Anderson. *Computational Fluid Dynamics*. Computational Fluid Dynamics: The Basics with Applications. McGraw-Hill Education, 1995. ISBN: 9780070016859. URL: <https://books.google.it/books?id=dJceAQAAIAAJ>.
- [3] Bharat Bhushan. "Bioinspired structured surfaces." In: *Langmuir* 28.3 (2012), pp. 1698–1714.
- [4] Lydéric Bocquet and Eric Lauga. "A smooth future?" In: *Nature materials* 10.5 (2011), pp. 334–337.
- [5] Casciola C.M. *Dispense del corso di tubolenza*. 2005.
- [6] A. B. D. Cassie and S. Baxter. "Wettability of porous surfaces." In: *Trans. Faraday Soc.* 40 (0 1944), pp. 546–551. DOI: [10.1039/TF9444000546](https://doi.org/10.1039/TF9444000546). URL: <http://dx.doi.org/10.1039/TF9444000546>.
- [7] Haecheon Choi, Parviz Moin, and John Kim. "Active turbulence control for drag reduction in wall-bounded flows." In: *Journal of Fluid Mechanics* 262 (1994), pp. 75–110.
- [8] Robert J Daniello, Nicholas E Waterhouse, and Jonathan P Rothstein. "Drag reduction in turbulent flows over superhydrophobic surfaces." In: *Physics of Fluids* 21.8 (2009), p. 085103.
- [9] Theodore De Karman and Leslie Howarth. "On the statistical theory of isotropic turbulence." In: *Proceedings of the Royal Society of London A: Mathematical, Physical and Engineering Sciences*. Vol. 164. 917. The Royal Society. 1938, pp. 192–215.
- [10] R Fernandez-Feria and E Sanmiguel-Rojas. "An explicit projection method for solving incompressible flows driven by a pressure difference." In: *Computers & Fluids* 33.3 (2004), pp. 463–483.
- [11] J.H. Ferziger and M. Peric. *Computational Methods for Fluid Dynamics*. Springer Berlin Heidelberg, 2012. ISBN: 9783642560262. URL: <https://books.google.it/books?id=BZnvCAAAQBAJ>.
- [12] Koji Fukagata, Kaoru Iwamoto, and Nobuhide Kasagi. "Contribution of Reynolds stress distribution to the skin friction in wall-bounded flows." In: *Physics of Fluids* 14.11 (2002), pp. L73–L76.
- [13] Koji Fukagata and Nobuhide Kasagi. "Highly energy-conservative finite difference method for the cylindrical coordinate system." In: *Journal of Computational Physics* 181.2 (2002), pp. 478–498.
- [14] Koji Fukagata, Nobuhide Kasagi, and Petros Koumoutsakos. "A theoretical prediction of friction drag reduction in turbulent flow by superhydrophobic surfaces." In: *Physics of fluids* 18.5 (2006), p. 051703.

- [15] Alberto Giacomello, Simone Meloni, Mauro Chinappi, and Carlo Massimo Casciola. "Cassie–Baxter and Wenzel states on a nanostructured surface: phase diagram, metastabilities, and transition mechanism by atomistic free energy calculations." In: *Langmuir* 28.29 (2012), pp. 10764–10772.
- [16] Sigal Gottlieb and Chi-Wang Shu. "Total variation diminishing Runge-Kutta schemes." In: *Mathematics of computation of the American Mathematical Society* 67.221 (1998), pp. 73–85.
- [17] TO Jelly, SY Jung, and TA Zaki. "Turbulence and skin friction modification in channel flow with streamwise-aligned superhydrophobic surface texture." In: *Physics of Fluids* 26.9 (2014), p. 095102.
- [18] Javier Jimenez. "Turbulent flows over rough walls." In: *Annu. Rev. Fluid Mech.* 36 (2004), pp. 173–196.
- [19] Steven M Kay and Stanley L Marple. "Spectrum analysis?a modern perspective." In: *Proceedings of the IEEE* 69.11 (1981), pp. 1380–1419.
- [20] John Kim and Parviz Moin. "Application of a fractional-step method to incompressible Navier-Stokes equations." In: *Journal of computational physics* 59.2 (1985), pp. 308–323.
- [21] John Kim, Parviz Moin, and Robert Moser. "Turbulence statistics in fully developed channel flow at low Reynolds number." In: *Journal of fluid mechanics* 177 (1987), pp. 133–166.
- [22] P.K. Kundu, I.M. Cohen, and D.R. Dowling. *Fluid Mechanics*. Academic Press, 2012. ISBN: 9780123821003. URL: <https://books.google.it/books?id=iUo4tsHQYUC>.
- [23] Eric Lauga and Howard A Stone. "Effective slip in pressure-driven Stokes flow." In: *Journal of Fluid Mechanics* 489 (2003), p. 55.
- [24] Miao'er Liu, Yu-Xin Ren, and Hanxin Zhang. "A class of fully second order accurate projection methods for solving the incompressible Navier-Stokes equations." In: *Journal of Computational Physics* 200.1 (2004), pp. 325–346.
- [25] Kanti V Mardia. "Measures of multivariate skewness and kurtosis with applications." In: *Biometrika* (1970), pp. 519–530.
- [26] Michael B Martell, J Blair Perot, and Jonathan P Rothstein. "Direct numerical simulations of turbulent flows over superhydrophobic surfaces." In: *Journal of Fluid Mechanics* 620 (2009), p. 31.
- [27] Taegee Min and John Kim. "Effects of hydrophobic surface on skin-friction drag." In: *Physics of Fluids* 16.7 (2004), pp. L55–L58.
- [28] Hyunwook Park, Hyungmin Park, and John Kim. "A numerical study of the effects of superhydrophobic surface on skin-friction drag in turbulent channel flow." In: *Physics of Fluids* 25.11 (2013), p. 110815.
- [29] John R Philip. "Flows satisfying mixed no-slip and no-shear conditions." In: *Zeitschrift für angewandte Mathematik und Physik ZAMP* 23.3 (1972), pp. 353–372.
- [30] Linfeng Piao and Hyungmin Park. "Two-dimensional analysis of air-water interface on superhydrophobic grooves under fluctuating water pressure." In: *Langmuir* 31.29 (2015), pp. 8022–8032.

- [31] Stephen B Pope. *Turbulent flows*. Cambridge: Cambridge Univ. Press, 2011. URL: <https://cds.cern.ch/record/1346971>.
- [32] Osborne Reynolds. "On the Theory of Lubrication and Its Application to Mr. Beauchamp Tower's Experiments, Including an Experimental Determination of the Viscosity of Olive Oil." In: *Proceedings of the Royal Society of London* 40.242-245 (1886), pp. 191–203.
- [33] WC Reynolds and AKMF Hussain. "The mechanics of an organized wave in turbulent shear flow. Part 3. Theoretical models and comparisons with experiments." In: *Journal of Fluid Mechanics* 54.02 (1972), pp. 263–288.
- [34] Jonathan P Rothstein. "Slip on superhydrophobic surfaces." In: *Annual Review of Fluid Mechanics* 42 (2010), pp. 89–109.
- [35] Mohamed A Samaha, Hooman Vahedi Tafreshi, and Mohamed Gad-el Hak. "Superhydrophobic surfaces: From the lotus leaf to the submarine." In: *Comptes Rendus Mécanique* 340.1-2 (2012), pp. 18–34.
- [36] J Seo, R García-Mayoral, and A Mani. "Pressure fluctuations and interfacial robustness in turbulent flows over superhydrophobic surfaces." In: *Journal of Fluid Mechanics* 783 (2015), pp. 448–473.
- [37] S Türk, G Daschiel, A Stroh, Y Hasegawa, and B Frohnäpfel. "Turbulent flow over superhydrophobic surfaces with streamwise grooves." In: *Journal of Fluid Mechanics* 747 (2014), pp. 186–217.
- [38] Robert N Wenzel. "Resistance of solid surfaces to wetting by water." In: *Industrial & Engineering Chemistry* 28.8 (1936), pp. 988–994.
- [39] JH Williamson. "Low-storage runge-kutta schemes." In: *Journal of Computational Physics* 35.1 (1980), pp. 48–56.
- [40] Jingxian Zhang, Haiping Tian, Zhaozhi Yao, Pengfei Hao, and Nan Jiang. "Evolutions of hairpin vortexes over a superhydrophobic surface in turbulent boundary layer flow." In: *Physics of Fluids* 28.9 (2016), p. 095106.

COLOPHON

This document was typeset using the typographical look-and-feel **classicthesis** developed by André Miede.

Final Version as of May 10, 2017 (classicthesis).